Computational Studies on Interfacial Dynamics in Complex Fluids

by

Mingfeng Qiu

B.Sc., Peking University, 2011

M.Sc., The University of Utah, 2013

A THESIS SUBMITTED IN PARTIAL FULFILLMENT
OF THE REQUIREMENTS FOR THE DEGREE OF

Doctor of Philosophy

in

THE FACULTY OF GRADUATE AND POSTDOCTORAL STUDIES

(Mathematics)

The University of British Columbia

(Vancouver)

August 2020

The following individuals certify that they have read, and recommend to the Faculty of Graduate and Postdoctoral Studies for acceptance, the thesis entitled:

Computational Studies on Interfacial Dynamics in Complex Fluids

submitted by **Mingfeng Qiu** in partial fulfillment of the requirements for the degree of **Doctor of Philosophy** in **Mathematics**.

Examining Committee:

James J. Feng, Mathematics, Chemical and Biological Engineering
Supervisor

Jean-Christophe Loudet, Physics, University of Bordeaux, France
Supervisory Committee Member

Ian Frigaard, Mathematics, Mechanical Engineering
University Examiner

Dana Grecov, Mechanical Engineering
University Examiner

Arun Ramchandran, Chemical Engineering, University of Toronto
External Examiner

Additional Supervisory Committee Members:

Gwynn Elfring, Mechanical Engineering
Supervisory Committee Member

Brian Wetton, Mathematics
Supervisory Committee Member

Abstract

This thesis aims to develop and apply modern computational techniques to study the interfacial dynamics involving complex fluids, where the underlying microstructure strongly affects the behaviour of the fluid. In particular, we have chosen two case studies that are significant to the current state of knowledge in specific fluids.

In the first problem, we investigate the interaction between a pair of ferrofluid drops subject to rotating magnetic fields. Through direct numerical simulation using a volume-of-fluid method, we classify four different regimes of the ferrofluid drop interaction. We closely examine the planetary motion regime and identify hydrodynamic interaction to be dominant over magnetic dipole interactions. We also discover a new interaction regime called drop locking, which is confirmed in experiments inspired by our study.

In the second problem, we first develop a phase-field method to compute elasto-capillary flows of nematic liquid crystals. The new formulation is able to simultaneously achieve a consistent description of structures of topological defects in the material, as well as an accurate recovery of macroscopic interfacial forces including surface tension and liquid crystal anchoring stress. This is made possible by incorporating a hydrodynamic theory of liquid crystals based on a tensor order parameter in a phase-field formalism approximating the sharp-interface limit. Then the method is applied to the drop retraction problem. We characterize a variety of different cases and examine their dynamics. Our numerical results reveal quantitatively that the drop deformation is a hallmark of competition between bulk distortional elasticity of the liquid crystal and surface tension. The new computational framework opens doors to a large class of fundamental problems concerning colloidal interaction in coupled elasto-capillary fields.

Lay Summary

Unlike water, the behaviour of complex fluids is strongly affected by their sophisticated microstructures. Near a fluid interface, these microstructures cause complex forces, coupled to the usual surface tension. We demonstrate how computer simulations are used to understand the physics of such systems studying two complex fluids: ferrofluid and liquid crystals.

We simulate how a pair of ferrofluid drops interact under a rotating magnetic field. We explain physical mechanisms of the drop motion, and discover a new type of motion. This study provides a building block for understanding ferrofluid emulsions and developing a number of biomedical applications.

We propose a general method for simulating interfacial flows of liquid crystals (LCs). Its advantage is capturing the LC microstructure and interfacial forces at the same time. We demonstrate this method through a drop retraction problem. This method opens doors to studying new classes of soft materials and active biological matter.

Preface

Chapter 2, Section 4.2, Chapter 5 have been published in Volume 846 of *Journal of Fluid Mechanics* by Cambridge University Press with the title "Interaction of a pair of ferrofluid drops in a rotating magnetic field" with modifications [137]. All figures and tables in these chapters and sections are extracted from [137] with permission from Cambridge University Press.

S. Afkhami (co-author in [137], New Jersey Institute of Technology, Newark, USA), C.-Y. Chen (co-author in [137], National Chiao Tung University, Taiwan, ROC) and J. J. Feng (thesis supervisor) conceived the ferrofluid project. J.-C. Loudet (supervisory committee member, University of Bordeaux, Bordeaux, France) and J. J. Feng conceived the liquid crystal project. J.-C. Loudet provided some literature references for Chapter 4 and Chapter 6.

Some of the analysis in Section 5.2.2 was consolidated by J. J. Feng (Figure 5.11, Figure 5.12). The scaling analysis presented in Section 6.2.8 were initially formulated by J.-C. Loudet and J. J. Feng, and refined by me.

I carried out the rest of the work presented in this thesis and publication [137], including reviewing literature, deriving theories in Section 4.3, writing codes, performing simulations and analyzing results. These were under guidance of S. Afkhami, J.-C. Loudet and J. J. Feng. I wrote this thesis and [137], with feedback from S. Afkhami, C.-Y. Chen, J.-C. Loudet and J. J. Feng.

Table of Contents

List of Tables

List of Figures

Acknowledgments

At times the Ph.D. seemed a bridge too far, particularly with a bumpy start of my academic career. I have come, with unbelievable fortune, to UBC Mathematics. Here I have enjoyed and appreciated every square inch of the collegiate soil from which I have grown.

I am deeply indebted to my advisor, Prof. Jimmy Feng, who chose to adopt an academic orphan five years ago. Over time I learned from his patience, truthfulness, compassion and sharpness. Thank you Jimmy, for bringing life to my academic dream.

I want to thank my two co-advisors, Profs. Shahriar Afkhami (NJIT Math) and Jean-Christophe Loudet (U of Bordeaux Physics), who have been working closely with me and gave me enormous help. Shahriar has warmly supported my career with technical suggestions, encouraging words, conference invitations, reference letters and so on. JC would always come to the lab and discuss in great detail our work, in addition to sharing travel stories, laughing off life challenges, and having a drink together. Apart from reference letters, he gave me strong encouragement when I ruminated with deep frustration and self doubt.

My gratitude also goes to other mentors in the Fluids Lab and the Math Department. Prof. Ian Frigaard has been a constant support with his witty remarks and geniality. Prof. Brian Wetton has been a candid and warm-hearted advocate for us all students. I thank Profs. Anthony Wachs, James Colliander and Gwynn Elfring for stimulating scientific discussions. Profs. Leah Keshet, Khanh Dao Duc and Eric Cytrynbaum from the Math Bio group have strongly influenced my scientific interest, and assisted me before interviews and talks, offering valuable suggestions. I must also thank the faculty overall for constantly bringing in external visitors, with

whom I have had inspiring scientific discussions.

I have been lucky to get opportunities in our Department to test and develop my teaching skills. I am thankful for a lot of mentors and fellow TAs and junior instructors who have worked with me. In particular, I want to thank Dr. Elyse Yeager, Dr. Patrick Walls, Dr. Matt Coles, Dr. Costanza Piccolo, Dr. Cole Zmurchock, and Katie Faulkner. And of course, so many thanks to the lovely students in MATH 102.

Over the years I have met incredibly wonderful colleagues and friends, in our own group, the Fluids Lab, the Feng-Keshet joint group (aka the "snacks group"), and the Institute of Applied Mathematics. I am particularly grateful for my best friend at UBC, Clinton Durney, who has a kind and open mind with an Asian stomach. I cannot possibly count the times that he offered critical help to me, that we shared thoughts and feelings, that we had meals and played chess. I also want to thank Amin Arefi, Dr. Thomasina Ball, Dr. Andreas Buttenschoen, Dr. Masoud Daneshi, Dr. Mohar Dey, Jieliang Hong, Dr. Ida Karimfazli, Ye Liu, Brian Merchant, Frédéric Paquin-Lefebvre, Zhiwei Peng, Dr. Lisanne Rens, Dr. Timm Treskatis, Sanna Tyrväinen, Prof. Paul Vigneaux, Chen Wang, Tony Wong, Yifu Zhou, Dr. Marjan Zare. Because of the restriction of space, I cannot thank you one by one. But without your support, both emotionally and scientifically, I would not have possibly sustained the years. At times when projects do not work, having the best colleagues and friends (i.e., you) is a strong reason to go to the office. I have enjoyed conversations with you in the IAM Lounge, in the seminar room, on a bus, in a restaurant, on a beach or a street in Vancouver regardless of the weather, on an RV, and on the internet.

Last but not least, I want to thank my family—my wife Xinyue and my parents, who have supported my choices without reservation over many years. I am so lucky to have them. Also thanks to Dumbledore—not the old wizard, but our physically huge and hugely adorable cat.

Chapter 1

Overview

1.1 Interfacial flows of complex fluids

Interfacial flow is ubiquitous in nature, from nanoscale droplets to the ocean surface. The asymmetry of materials across the interface, and thus of molecular forcing, gives rise to surface tension. In this thesis, we focus on interfacial flows at small length scales, typically from hundreds of nanometers to a few millimeters, such that surface tension plays a significant role. There are many classical examples where surface tension drives physical phenomena, which have been attracting scientists' attention for decades. These include, for instance, formation of drops [33], capillary waves [4], Rayleigh-Plateau instability [28], and the Cheerios effect [174].

Meanwhile, many flow phenomena involve complex fluids, whose rheology is strongly affected by their microstructure [e.g., 83]. Common examples include biological fluids such as saliva, food and drinks such as milk and smoothies, geophysical fluids such as snow and rocks in an avalanche, industrial fluids such as polymer melts to manufacture plastics. One can find that many of complex fluids consist of a phase dispersed in another. For more examples, corn starch suspended in water, cosmetics liquids and creams, slurries, and foams are all of this type. One characteristic of many complex fluids is that the shear stress does not grow linearly with shear rate, together with other properties not seen in a simple fluid like water.

Interfacial flows of complex fluids arise when the two factors reviewed above

meet. These flows are usually governed by the coupled surface tension and complex rheology, thereby displaying rich behaviour. One such instance is viscoelastic fluids like biological liquids. The elasticity of the fluids, often owing to long-chain molecules such as proteins or polymers, significantly alters their interfacial behavior. A consequence is that the high normal stress due to stretching of the molecules in a straining flow of viscoelastic fluids suppresses liquid bridge pinch-off in late stages of the Rayleigh-Plateau instability [184]. Another example involves viscoplastic fluids, featuring many everyday, industrial and geophysical fluids such as toothpaste, colloidal gels, petroleum, and volcanic lava domes [84]. One effect arising from the yield stress of viscoplastic fluids in interfacial dynamics is that it suppresses fingering driven by surface tension in an advancing thin film [16]. Other examples of interfacial flows of complex fluids include polymer blending, where immiscible polymer melts are mixed together to make high-performance composite material [150], and polymer-dispersed liquid crystals, in which liquid crystal droplets are dispersed in a polymer melt to obtain desirable optical properties [42]. Understanding these phenomena involving a moving interface with surface tension and a complex fluid is thus crucial for both fundamental science and industrial applications and economy.

1.2 Contribution of this thesis

In this thesis, our over-arching goal is to contribute to the understanding of how complex rheology couples with surface tension in interfacial phenomena of complex fluids. Toward this objective, we have chosen two case studies, both important to the current state of knowledge: (i) ferrofluid drop interaction in rotating magnetic fields, and (ii) elasto-capillary flows of liquid crystals. The problems involve complicated geometries (multiple ferrofluid drops in relative motion) and fluid constitutive models (liquid crystal rheology). Therefore, we use computational techniques to study them. Below we outline the main novelties in this thesis.

Ferrofluid is a stable suspension of nano-size magnetizable particles. Normally it behaves as any Newtonian fluid, but reacts to magnetic fields. In terms of the physics of ferrofluid drops, a lot has been known about the shape of a single drop in a static magnetic field and a rotating field, as well as assembling of an array of

drops in a static field. There has not been as much knowledge, however on how ferrofluid drops interact under a rotating field. Inspired by recent experiments which have identified a planetary motion of drops, we use direct numerical simulation to study drop interaction for the first time. We have investigated the planetary motion in detail, and demonstrated that the motion is dominated by a hydrodynamic interaction through viscous flow. It explains features of the motion distinct from magnetic dipole interactions. We have also identified a new drop locking regime and explained the regime transition. This numerical discovery has been confirmed in experiments by other researchers. Our study has provided a building block for understanding more complicated phenomena involving drop interaction, such as ferrofluid emulsions, and developing novel biomedical applications.

The second part of the thesis is motivated by two merging lines of research, one on the interaction of colloids under elastic forces in the bulk of a liquid crystal, and the other on the interaction of colloids with surface tension on a fluid-fluid interface. Latest experiments have only scratched the surface of the rich behaviour displayed in the colloidal interaction between particles trapped at an interface of a liquid crystal. To tackle these problems, one needs reliable and flexible numerical tools. In this thesis, we develop a phase-field model for computing the interfacial flows of nematic liquid crystals. Thanks to our careful design exploiting the diffuse-interface dynamics, our model is the first to capture both liquid crystal microstructure, in particular the topological defects, and interfacial forces including surface tension and the anchoring stress of the liquid crystal. We then apply this method to the drop retraction problem which validates our model by reproducing known features. Our study further provides a comprehensive map of defect and drop configurations in drop retraction, as a function of material combinations, anchoring conditions, and spatial dimensions. Using numerical data, we have discovered a proportional relation between the drop deformation at steady state and an intrinsic length scale. This new relation highlights the competition between nematic distortional elastic energy with surface energy, mediated by anchoring energy at the interface.

We will further justify the significance of these two problems in detail in Section 2.1 and Section 3.1, respectively, and identify specific open problems. The sections also review the mathematical descriptions of these two fluids. In Chapter 4

on methodology, I start with a mini-review of numerical methods for multiphase flows in general, relating to complex fluids. More detailed formulations associated with our chosen problems are subsequently developed in the same chapter. We then solve the problem of a pair of interacting ferrofluid drops under a rotating magnetic field in Chapter 5. In Chapter 6, I show numerical examples to validate our new method developed for interfacial flows of liquid crystals, and present the application of this method to the drop retraction problem. Concluding remarks regarding both problems are included in corresponding chapters. We recall the progress in knowledge made in this thesis and discuss general future directions in Chapter 7.

1.3 Notational convention

Note that due to the breath covered in this thesis, a clash of notations is inevitable between the two problems: ferrofluid and liquid crystals. The same symbols can represent distinct quantities in different problems. However, the reader is also assured that within each specific problem, the notation is consistent, and the meanings of symbols shall be clear from their context.

Nevertheless, the following convention applies to the whole thesis.

- The operator $\partial_i \cdot$ means partial derivative with respect to the variable i. Usually, $i = t$ which means time, or $i = 1, 2, 3$ where the numbers denote the first, second, and third spatial dimensions, respectively. They correspond to x, y, z in Cartesian coordinates or r, θ, z in cylindrical coordinates.

- When invoking the index notation, we always assume Cartesian coordinates, unless stated otherwise explicitly in the text.

- The gradient of tensors (including vectors) follows the same ordering rule for the indices as in tensor products. For example, let $\boldsymbol{A}$ be a tensor of second rank. Using the index notation, its gradient is defined as

$$(\nabla \boldsymbol{A})_{ijk} = \partial_i A_{jk}. \tag{1.1}$$

- In inner products of tensors, contractions start from the nearest indices. For

example, let $\boldsymbol{B}$ be another second-rank tensor. Then

$$(\boldsymbol{A} \cdot \boldsymbol{B})_{ij} = A_{ik} B_{kj}. \tag{1.2}$$

- The divergence of tensors follows the two rules above, i.e.,

$$(\nabla \cdot \boldsymbol{A})_j = \partial_i A_{ij}. \tag{1.3}$$

Chapter 2

Background of ferrofluid drop interaction

2.1 Introduction

A ferrofluid is a suspension of magnetizable nano-particles in a carrier fluid. Owing to the ultra-fine particle size and the colloidal stability, a ferrofluid appears as a homogeneous medium, but it displays a variety of novel interfacial phenomena under an external magnetic field [34, 35, 51, 114]. As ferrofluids can be manipulated remotely by a magnetic field, they find applications in mechanical seals, damping systems and loudspeakers [15, 147, 171]. More recently, ferrofluids have been studied for potential applications in drug delivery [175], treatment of retinal detachment [110], control of microfluidic devices [168], and mechanical measurement in biological tissues [152]. In these cases, the dynamics of deformable ferrofluid drops suspended in an immiscible liquid plays an essential role.

The behaviour of a single ferrofluid drop in a static uniform field is well understood. It elongates in the field direction as the magnetic force pulls the drop against interfacial tension. At small deformation, the equilibrium drop shape can be calculated approximately by assuming a prolate spheroidal shape [12]. At large deformations numerical computation is necessary [7, 148]. Zhu et al. [191] studied the case of a drop resting on a hydrophobic substrate, with the field direction parallel to the substrate. Other studies have examined the motion of a ferrofluid drop in

a magnetic field driven by buoyancy [78] or a field gradient [6], drop rupture [50] and drop relaxation [148].

In a rotating magnetic field, a single ferrofluid drop exhibits an array of interesting dynamics. When the angular velocity of the field—called the driving frequency hereafter—is low, a drop elongates as in a static field and follows the rotation of the field. With increasing driving frequency, the prolate drop may bend [29, 80] or even break up [86] because of viscous friction in the surrounding medium. At even higher frequencies, the drop may assume several shapes depending on the field strength, ranging from oblate spheroidal at low field strength to a "spiny starfish" shape at high field strength [13, 30, 87, 116]. The recent boundary-integral computation of Erdmanis et al. [48] has successfully reproduced many of these shapes.

A pair of ferrofluid drops interact in a static field because of mutually induced magnetization. If their line of centers is initially perpendicular to the external static field, the drops repel while rotating around each other so that their line of centers aligns with the field. Meanwhile the radial force becomes attractive and the two approach each other and may even coalesce [32]. A similar scenario occurs in the equivalent problem of two bubbles interacting in a ferrofluid [89]. In both cases, the magnetophoretic interaction can be understood by viewing each drop as an effective magnetic dipole. If an array of ferrofluid drops are constrained in a plane and a static external field is applied perpendicular to the plane, the drops assemble into a hexagonal lattice owing to the magnetic repulsion among them [31, 169].

Note that the ferrofluid problem is equivalent to an electrohydrodynamic (EHD) problem for perfect dielectrics, with no free charge and vanished conductivity. Thus, the observations above have counterparts in EHD studies, e.g. on the equilibrium shape of a dielectric drop in an insulating fluid [60, 154], the conical ends of a drop under high field strength [163], and the dielectrophoretic alignment of drops [18].

For a pair of ferrofluid drops in a rotating magnetic field, Chen et al. [32] observed an intriguing "planetary motion", illustrated in figure Figure 2.1. In their experiments, the millimeter-sized drops elongate in the field direction into an approximately ellipsoidal shape and then spin in phase with the rotating field. The driving frequency is too low for any of the shape instabilities [87]. In addition to the self-spin, the drops revolve around each other in the same sense as the rotation

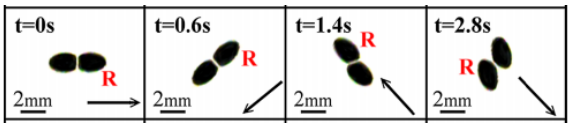

Figure 2.1: Snapshots of the planetary motion of a pair of ferrofluid drops under a magnetic field of uniform strength $H_0 = 4488$ A/m that rotates counterclockwise at a driving frequency of 1 Hz. The letter "R" marks the drop initially on the right. Reproduced from Chen et al. [32] with permission, ©Springer.

of the field. This planetary revolution does not proceed smoothly with a constant angular velocity, but is punctuated by periodical reversals. The averaged angular velocity is much lower than that of the field. Moreover, a larger number of drops arrange themselves into a regular array that revolve in the sense of the rotating field, at a much lower angular velocity.

For understanding the cause of the planetary revolution, the most closely related work is perhaps Bacri et al. [14], which concerns a pair of micron-sized highly viscous ferrofluid drops in a rotating field. Because of the small size of the drops, their high viscosity and presumably surface immobilization by surfactant transport, the drops deform little and behave essentially as rigid particles. A pair of solid particles are known to exhibit a revolution around each other [59, 67] beyond a critical driving frequency. This can be rationalized by treating each particle as a magnetic dipole, and balancing the magnetophoretic forces with a Stokes drag on the particle [14, 67]. Both studies also predict that the angular velocity of the doublet revolution decreases with the driving frequency.

The experiment of Chen et al. [32] differs from the solid-particle studies in that the drops are large (radius $r_0 \sim 1$ mm); they deform and are subject to inertial effects. Can their planetary motion be explained by the same dipole model, or does it involve distinct mechanisms? Are there other modes of interaction between deformable ferrofluid drops? These questions have motivated the current study. We have conducted a careful two-dimensional (2D) numerical simulation of the interaction between a pair of ferrofluid drops in a rotating field. We have reproduced the planetary revolution but found that it arises from different mechanisms. Although the magnetophoretic forces play a role, the most important factor is the hydrody-

namic interaction between the elongated drops termed "viscous sweeping". We have also discovered a novel "drop locking" regime, which has been confirmed by other researchers in new experiments.

We choose to use the volume-of-fluid (VOF) formalism to solve the two-phase ferro-hydrodynamics problem numerically. This is because the property of ferrofluid under a slow magnetic field, in the sense that magnetic relaxation is instant, is simple enough so that a VOF formulation can be readily constructed. The VOF method has also been used in [e.g., 6, 7] to investigate the shape and dynamics of a single ferrofluid drop. The highly efficient and accurate VOF algorithms devised in [101, 131] can be employed to tackle the physical problem we are faced with. For more details of the VOF method, see Section 4.1. In the following, we review the mathematical theory of ferrofluid hydrodynamics. This theory is incorporated in a multiphase formulation in Section 4.2. For results of this problem, the reader is referred to Chapter 5.

2.2 Mathematical description of hydrodynamics of ferrofluid

Consider a general magnetizable fluid (either a ferrofluid or a simple viscous fluid). It is Newtonian in its viscous stress and incompressible. Because we will use matched density in our ferrofluid drop with the viscous medium, gravity or buoyancy is immaterial. The equations of motion for such a fluid are [7]

$$\nabla \cdot \boldsymbol{v} = 0, \tag{2.1}$$

$$\rho \left(\partial_t \boldsymbol{v} + \boldsymbol{v} \cdot \nabla \boldsymbol{v} \right) = -\nabla p + \nabla \cdot (2\eta \boldsymbol{D}) + \nabla \cdot \boldsymbol{\tau}_m. \tag{2.2}$$

Here p is the pressure, $\boldsymbol{v}$ the velocity, ρ the density, and η the dynamic viscosity. $\boldsymbol{D} = (\nabla \boldsymbol{v} + \nabla \boldsymbol{v}^{\intercal})/2$ is the rate of deformation tensor. The Maxwell stress tensor $\boldsymbol{\tau}_m$ represents the magnetic forcing on the fluid. All magnetic equations and quantities in this thesis are in SI units. Both fluids are assumed to be dielectric, with instantaneous relaxation of magnetic moments within the ferrofluid (i.e.,

"superparamagnetic") [55, 156, 167]. Hence,

$$\boldsymbol{\tau}_m = \mu \boldsymbol{H}\boldsymbol{H} - \frac{1}{2}\mu H^2 \boldsymbol{I}, \tag{2.3}$$

where μ is the magnetic permeability of the material. The surrounding fluid (denoted by subscript s) is non-magnetic, so its permeability μ_s equals that of vacuum $\mu_0 = 4\pi \times 10^{-7}$ N/A^2. For the ferrofluid drop (denoted by subscript d), $\mu_d = \mu_0(1+\chi)$ with χ being the magnetic (volume) susceptibility. $\boldsymbol{H}$ is the magnetic field vector. As commonly done in the literature [7, 48], we assume magnetostatics so $\boldsymbol{H} = -\nabla\varphi$ is irrotational, φ being the magnetic potential, and the Maxwell equations reduce to

$$\nabla \cdot (\mu \nabla \varphi) = 0. \tag{2.4}$$

In Section 4.2 we present this theory in a two-phase flow formulation.

Chapter 3

Background of elasto-capillary flows of liquid crystals

3.1 Introduction

In soft matter physics, two lines of research have been pursued fruitfully but independently. One is colloidal interaction in the bulk of a liquid crystal where elastic forces arise through disruption of order in the microstructure of liquid crystal. The other is colloidal interaction on a fluid-fluid interface through surface tension. In recent years, there is growing interest to merge these two lines and investigate colloids under coupled elasto-capillary effects. A model system consists of colloidal particles straddling an interface of a liquid crystal.

Motivated by this trend, we construct a general method for direct numerical simulation of such systems, with an accurate account of both elastic and capillary forces. In this section, I review the basic physics in the two merging lines of research, state-of-the-art in the understanding of elasto-capillary interactions, and our approach.

As a remark, conventionally the subject of "elasto-capillary" phenomena concerns an elastic solid interacting with capillary forces under small scales [146]. It should be distinguished from the topic in this thesis where elasticity arises from the microstructure of a fluid.

3.1.1 Liquid crystals and their properties

In general, the building blocks of matter are anisotropic in shape. Their orientation gives rise to additional degrees of freedom of the material. A liquid crystal (LC) is an intermediate state of matter (also called "mesophase") characterized by partial positional and/or orientational order of its building blocks. In other words, LC molecules diffuse and advect more or less freely, but point toward some well-defined direction to an extent. The alignment arises from the anisotropic interaction potential between molecules. LC is a rich topic with many different kinds of LCs. In this thesis, we only consider the simplest phase of LC, i.e., the *nematic* phase. It consists of rod-like molecules which tend to align parallel to each other and flow freely. A nematic has no positional order and only orientational order along one direction. LCs can also be categorized into being thermotropic or lyotropic. *Thermotropic* LCs are those whose phase depends solely on temperature. A *Lyotropic* LC is a solution whose phase depends on concentration of the solvent. The examples visited in this thesis will only involve thermotropic LCs. However, one just needs a minor generalization in our method to describe a lyotropic LC in multiphase flows (see Section 3.2.3).

In a nematic LC, one way to describe molecular alignment is to introduce $\boldsymbol{n}$ as the average direction of alignment of an ensemble of rod-like molecules. $\boldsymbol{n}(\boldsymbol{x}, t)$ is thus an order parameter, and is a pseudo-vector field since we don't distinguish between the head and tail of a nematic molecule. $\boldsymbol{n}$ is called the *director* (also called the *optical axis* due to its interaction with electromagnetic fields).

On the boundary of an LC, its molecules usually take well-defined directions, called *easy directions*, based on physical-chemical conditions of the contacting surface. These are the so-called *anchoring conditions*. Conflict between the topology of the boundary with that of the bulk of an LC material gives rise to singularities in the $\boldsymbol{n}$ field, termed *topological defects*. On the molecular level, at these locations molecular order is decreased. Figure 3.1 illustrates several common types of defects. The ellipses represent average molecular orientation in space ($\boldsymbol{n}$), with the green disks marking the defects. Figure 3.1(a) and Figure 3.1(b) are point defects. They are called the *radial* and *hyperbolic hedgehog* defects, respectively. Figure 3.1(c,d) are point defects in 2D or line defects in 3D.

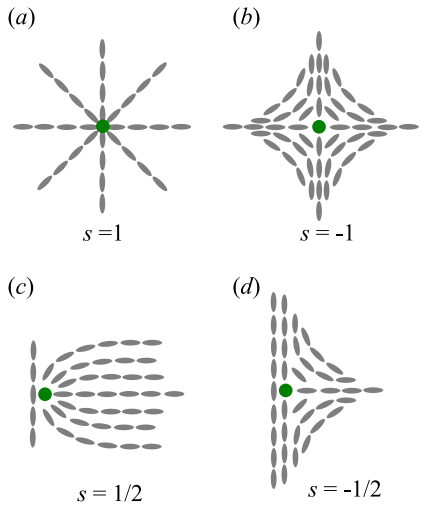

Figure 3.1: Common topological defects in the bulk of nematic LC with their winding numbers s. The ellipses represent the average molecular orientation (n). The green dots mark the loci of the defect. (a) Radial hedgehog. (b) Hyperbolic hedgehog. (c,d) Two defects of opposite half-integer winding numbers.

The *winding number* s (or *defect strength*, or *topological charge*) is a basic topological property characterizing the structure of a defect [26, 38]. In loose terms, s can be defined as follows. Away from the defects, the director field is a continuous vector field, mapping an Euclidean space (physical space) to a configuration space containing all possible directions of $\boldsymbol{n}$. We introduce a closed manifold enclosing a defect. The winding number is defined as the number of times the $\boldsymbol{n}$ map "covers" the configuration space. In 2D, the configuration space is the full circle of unit radius $\mathbb{S}^1$. The winding number is the number of times $\boldsymbol{n}$ rotates by 2π along an arbitrary closed curve circling the defect core, counter-clockwise being positive and clockwise being negative. For example, the hedgehogs have $s = 1$ (Figure 3.1a) or $s = -1$ (Figure 3.1b) depending on if it is radial or hyperbolic. In Figure 3.1(c,d), the defects have half-integer winding numbers. This also characterizes line defects in 3D, where the value of s conveniently remains the same. For point defects in 3D, one needs a surface to enclose the defect core. The configuration space is the unit sphere $\mathbb{S}^2$. The number of times the range of $\boldsymbol{n}$ traverses $\mathbb{S}^2$

is the winding number. Hedgehogs in 3D still have $s = \pm 1$ (Figure 3.1*a*,*b*). The basic property of the winding number is that the sum of s is conserved, i.e., the s value of a group of defects is equal to the sum of s values of each of the defects. Readers are referred to [85, 111] for more details.

The spontaneous alignment of LC molecules endows the material with an elastic energy. Elastic stress arises when the molecular alignment is disturbed. Due to large distortions nearby, topological defects are sites of high elastic energy and stress. Multiple topological defects interact with each other through long-range elastic forces.

3.1.2 Colloidal particles in the bulk of LC

Anchoring and defects play important roles in colloidal suspensions in an LC. We review here three most basic defect structures associated with a spherical particle submerged in a nematic. They will also be instrumental for interpreting our results in Chapter 6. On the particle surface, there are two kinds of common anchoring conditions: *homeotropic* where nematic molecules are perpendicular to the surface, and *planar* where nematic molecules are tangential to the surface. In the far field, LC molecules are aligned uniformly in parallel in some direction. Figure 3.2 shows defect structures commonly observed in experiments. The solid black lines are streamlines of the $\boldsymbol{n}$ field. Under homeotropic anchoring, a *Saturn ring* is a line defect circling the particle in a plane perpendicular to far-field alignment with winding number $-1/2$ (Figure 3.2*a*). In the vicinity of the line defect, molecular alignment is similar to Figure 3.1(*d*). The director distribution around the particle has a quadrupolar symmetry. Alternatively, a hyperbolic hedgehog (Figure 3.1*b*) forms on one side of the particle (Figure 3.2*b*). The particle-defect pair lies in parallel with far-field alignment, and the overall director distribution has a dipolar symmetry. Which defect emerges depends on material properties, the particle size, the domain size, and presence of other fields [52, 140] (also see Section 6.1.1). Under planar anchoring, typically two surface defects of winding number 1, called "*boojums*", form (Figure 3.2*c*). The director field has quadrupolar symmetry.

When multiple colloids are in the bulk of an LC, each of them induces a companion defect. These colloid-defect pairs interact through long-range elastic forces

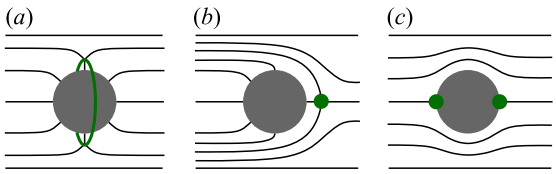

Figure 3.2: Common topological defects formed around a spherical colloid submerged in a nematic LC. The solid black lines are streamlines for the $\boldsymbol{n}$ field, and the green solid line/dots show the defects. (*a*) The Saturn-ring defect under homeotropic anchoring. (*b*) The hyperbolic hedgehog defect under homeotropic anchoring. (*c*) The boojum defects under planar anchoring.

and could assemble into regular patterns [e.g., 118, 134, 135]. For more details on LC colloids, refer to review articles [22, 56, 140, 157] and the references therein.

3.1.3 Capillary interaction of particles

In preparation for colloids trapped at LC interfaces, in this section we review the basics of capillary interaction of colloids on interfaces of isotropic fluids. The interaction is caused by lateral capillary forces, which originate from the overlapping deformations of the fluid interface by the particles. Interfacial deformation is determined by three factors: gravity, particle wetting conditions, and undulated three-phase contact lines [37]. For a relatively large particle, a meniscus forms for surface tension to balance gravity. Gravity-induced interfacial deformation is immaterial if the particle is small. Nevertheless, deformation due to wetting conditions is still operative even for nano-sized particles. The contact lines can be distorted due to anisotropic particle shapes [90, 103] or heterogeneities of particle surface properties such as chemical composition or surface roughness [106, 160]. These heterogeneities can be artificially created [127] or simply inevitable in practice.

Similar to elastic interactions of colloids in bulk liquid crystals, the capillary interaction of colloids at an interface is long-ranged compared to molecular forces. The energy scale is also much larger than thermal fluctuation, even for nano-sized particles [37]. Besides, the capillary interaction by undulated contact lines is anisotropic [127, 160]. For example, two cylindrical particles interact dif-

ferently when they are placed side-to-side, or end-to-end, or side-to-end.

For more details regarding capillary interaction, refer to reviews [79, 100, 122] and the references therein.

3.1.4 Coupled elasto-capillary systems

As mentioned above, both the elastic interaction of colloids in LC and capillary interaction on an interface are long-ranged and dominate thermal fluctuation. Both could be anisotropic. Therefore, it is natural to bring the above two lines of research together and consider colloidal interactions under coupled elasto-capillary effects. In particular, it is easy to design such systems in practice.

A number of experiments on this system have been done to probe the behaviour of colloids in coupled elasto-capillary fields, showing rich results. A hexagonal lattice is formed by particles with either tangential or homeotropic anchoring [61, 158]. In contrast, particles with homeotropic anchoring in a bulk nematic assemble into a rectangular lattice [118]. At a high density, the particles with tangential anchoring transition into a more compact lattice [121], while those with homeotropic anchoring lose the order to become a dense amorphous state [61]. In thin nematic films, particles form chains in the direction of global nematic alignment under both anchoring conditions [61, 158]. A few other studies have been dedicated to colloids in an extremely thin nematic layer—with a thickness comparable to the particle diameter [62, 73, 74, 99]. In this case, much larger separation between the particle and its companion defect is observed compared with dipoles in the bulk of a nematic, suggesting a strong influence of capillary action on elastic interactions.

As for modeling of such systems, both theoretical and numerical studies are scarce. Oettel et al. [123] derived interaction forces between a pair of particles trapped on the interface of a nematic phase, in the limit of large particle separation. Contrary to experiments, only when the nematic phase has a finite film thickness could they recover an attractive capillary interaction force, which was nevertheless negligible compared to thermal fluctuation. Jeridi et al. [74] calculated defect structures around a spherical particle in a thin nematic film. It shows a variety of defect configurations as a result of the confinement from the thin film.

3.1.5 Contribution of this thesis

With the above summary, we emphasize that understanding of elasto-capillary phenomena concerning colloids is far from complete. First, from the experimental studies, novel behaviour of colloids trapped at LC interfaces is found compared to on Newtonian fluid interfaces. These phenomena await satisfactory explanation from modeling. Second, there are many fundamental questions that need to be answered. For example, how does interface capillarity affect defect configurations around particles? How do the defects and associated elastic forces modify drag forces on a particle straddling an interface? What are the characteristics of elasto-capillary pair interactions (range, magnitude)? How does the LC/isotropic interface curvature modify these interactions?

Moreover, there is a lack of reliable, versatile modeling tools to answer these problems. First, due to their complexity, these problems remain theoretically intractable. The approximate derivation presented by Oettel et al. [123] is incapable to describe the strong interaction between colloids on nematic interfaces discovered by experiments. Second, owing to the lack of numerical tools, computational research is restricted to only limiting cases. The 3D calculations presented in Jeridi et al. [74] follow the paradigm in Ravnik and Žumer [140] and only incorporate minimization of the total energy. The fluid interface is kept flat, which only applies to cases with a large surface tension.

Therefore, the objective of this part of the thesis is to bridge this gap and develop a computational framework that is capable of modeling elasto-capillary interactions. We do this by combining two well-developed lines of approaches modeling interfacial flows and LC dynamics, respectively.

When choosing a formalism to describe the moving interface, the energetic nature of LC dynamics makes it naturally amenable to Phase-Field (PF) methods (see Section 4.1). In the case of liquid crystal flows, Yue et al. [181, 183], Zhou et al. [188, 189] used their sharp-interface-approximating PF method to study a category of elasto-capillary systems consisting of one or more soft drops dispersed in the bulk of a nematic. The common drawback of these studies limiting their applicability, however, is that they all used the regularized Leslie-Ericksen (LE) theory to describe nematic order. For one, this simplified theory is based on the

director $\boldsymbol{n}$ as the order parameter. It assumes that local alignment is not much disturbed away from the defect core, which may not hold in strong flows (see Section 3.2). For the other, in order to accommodate defects in the computation, a regularization [93] was introduced, resulting in nonphysical defect structures (see Section 3.2.2). These limit the applicability of the previous studies. On the other hand, using a tensorial order parameter to describe molecular configuration is free from these artifacts, and can reproduce consistent defect structures as observed in experiments [140]. However, in this class of research, most of the existing computations [e.g. 74, 140] are incapable of modeling a moving interface. Lately some studies used a phase-field model to describe two-phase mixtures including a nematic phase [112, 113]. However, the relationship of their models to the sharp-interface limit is unclear and the macroscopic interfacial forces are intractable.

Hence, we incorporate the tensorial description of nematic order and a tensor-based model for hydrodynamics of LC, into the phase-field model proposed by Yue et al. [181]. The advantage of our method over previous numerical tools is to achieve accurate calculation of surface tension and consistent description of LC microstructure *simultaneously*. For numerical approximation, we use a finite element method similar to [185], allowing for high flexibility in problem geometry and mesh deployment compared with other interfacial calculations such as [112].

In Section 4.3, I present the generalization of the PF formulation in the tensorial context and derive terms in various equations related to LC anchoring. We show the capability of this method in Chapter 6. It includes a series of numerical examples of increasing complexity for validation, as well as the application of the method on the drop retraction problem where we develop novel physical insights into elasto-capillary flows by computation.

3.2 Mathematical theory for nematic liquid crystals and their hydrodynamics

We start by clarifying the construction of an order parameter in a nematic. Subsequently we review the Beris-Edwards theory for bulk LC flow. The theory covered here will be incorporated into the PF formalism in Section 4.3.

3.2.1 LC order parameter

Different conventions for LC order are used by different researchers, sometimes without consent on a standard definition. Hence, here I define our choice of an order parameter. The following description is from compilation of literature, applied to our specific case. For more details, see [21, 38, 43, 83].

We limit our study to *uniaxial nematic* LCs consisting of rod-like molecules which have rotational symmetry about some axis. Let the vector $\boldsymbol{u}$ denote a particular molecule's orientation, e.g., the axis of rotational symmetry. Then it is a point on the unit sphere $\mathbb{S}^2$. At equilibrium free from external forces, thanks to the nematic alignment, the distribution function for the molecular orientation $\psi(\boldsymbol{u})$ would have complete rotational symmetry about a direction $\boldsymbol{n}$, i.e., the director. We further assume that there is always equal distribution between $\boldsymbol{u}$ and $-\boldsymbol{u}$ directions. Then $\psi(\boldsymbol{u}) = \psi(-\boldsymbol{u})$ and we don't distinguish head or tail of $\boldsymbol{n}$. The uniaxial building block assumption relieves us from considering additional orientation vectors and order parameters. Note that when only "nematics" is used in literature, it usually refers to uniaxial nematics, i.e., nematics made from uniaxial building blocks. The anisotropy of the orientations of an ensemble of molecules can be described by the following tensor of rank 2:

$$\boldsymbol{Q} = \left\langle \boldsymbol{uu} - \frac{1}{3}\boldsymbol{I} \right\rangle = \int_{\mathbb{S}^2} \left(\boldsymbol{uu} - \frac{1}{3}\boldsymbol{I} \right) \psi(\boldsymbol{u})\, d\boldsymbol{u}, \tag{3.1}$$

which is the traceless part of the moment of second order of $\psi(\boldsymbol{u})$. $\boldsymbol{I}$ is the unit tensor of second rank. The moment of first order vanishes thanks to the symmetry $\boldsymbol{u} = -\boldsymbol{u}$. Note that $\boldsymbol{Q}$ is symmetric and has zero trace.

We say that the nematic is in a *uniaxial state* if i.e., the molecular distribution has rotational symmetry around $\boldsymbol{n}$. $\boldsymbol{Q}$ can be written as

$$\boldsymbol{Q} = q \left(\boldsymbol{nn} - \frac{1}{3}\boldsymbol{I} \right). \tag{3.2}$$

q is a constant, defined to be the *scalar order parameter*. It is a measure of how

well the ensemble of molecules are aligned to $\boldsymbol{n}$. Indeed, one can see

$$q = \frac{3}{2}\boldsymbol{n}\cdot\boldsymbol{Q}\cdot\boldsymbol{n} = \frac{3}{2}\left\langle (\boldsymbol{u}\cdot\boldsymbol{n})^2 - \frac{1}{3}\right\rangle . \tag{3.3}$$

If $\boldsymbol{u}$ is distributed randomly, i.e., $\psi(\boldsymbol{u})$ is isotropic, then $q = 0$. If all molecules align exactly in the $\boldsymbol{n}$ direction, $q = 1$. If all molecules are perpendicular to $\boldsymbol{n}$ but randomly distributed in the equatorial plane, then $q = -1/2$. Thanks to these properties, we choose $\boldsymbol{Q}$ to be our order parameter.

Because $\boldsymbol{Q}$ is symmetric, it has three real eigenvalues (not necessarily distinct) and three mutually orthogonal eigenvectors. The molecular alignment state can be identified through the eigenvalues. There are three cases in general.

(i) All three eigenvalues are equal. Then they all have to vanish. The molecular distribution is isotropic. There is no particular orientational order.

(ii) Two of the three eigenvalues are equal. This is the uniaxial state in which molecular distribution is rotationally symmetric. The eigenvalues must be $2q/3, -q/3, -q/3$. The eigenvector corresponding to the largest eigenvalue in magnitude gives the axis of symmetry $\boldsymbol{n}$ (See Equation 3.2). If identifying $\boldsymbol{n}$ with the x-direction, then

$$\boldsymbol{Q} = \begin{bmatrix} \frac{2}{3}q & 0 & 0 \\ 0 & -\frac{1}{3}q & 0 \\ 0 & 0 & -\frac{1}{3}q \end{bmatrix} . \tag{3.4}$$

(iii) All three eigenvalues are distinct. In this case, the uniaxial nematic is said to be in a *biaxial state*. It suggests strong distortions of molecular distribution. This occurs near, for example, topological defects.

The above definition of the scalar order parameter q relies on the existence of rotational symmetry about the director $\boldsymbol{n}$. We would like to generalize the notion of q in order to obtain an indicator of molecular alignment in all cases. Here we describe two conventions commonly used in literature.

(i) The Frobenius norm of the tensor $\boldsymbol{Q}$ multiplied with a constant

$$q = \left(\frac{3}{2} \boldsymbol{Q} : \boldsymbol{Q}^{\mathsf{T}} \right)^{\frac{1}{2}}. \tag{3.5}$$

One can derive it from $\boldsymbol{Q}$ in the uniaxial state in Equation 3.2: $\boldsymbol{Q} : \boldsymbol{Q}^{\mathsf{T}} = 2q^2/3$. It is used in the classical Maier and Saupe theory [e.g., 52, 83].

(ii) The largest-in-magnitude eigenvalue of the tensor $\boldsymbol{Q}$ multiplied with a constant

$$q = \frac{3}{2} \lambda_{|\max|}. \tag{3.6}$$

Again, after diagonalizing Equation 3.2 we obtain Equation 3.4 and $\lambda_{|\max|} = 2q/3$. A few studies use this form [e.g., 10, 65, 70].

These two definitions are equivalent only under uniaxial state. In this thesis, we use (i) to define the general scalar order parameter q, which clearly applies more widely.

In this thesis we only consider cases in 2D, where we embed the geometry in a 3D Euclidean space. Generally, in a Cartesian frame, individual molecular direction $\boldsymbol{u}$ can "tilt" into the third (z) dimension, provided that every variable satisfies the condition $\partial_3 \cdot = 0$. In this thesis, for simplicity, we further assume that the molecular distribution $\psi(\boldsymbol{u})$ is symmetric about the 1-2 plane, thereby requiring $Q_{23} = Q_{13} = 0$. In a cylindrical frame, the above assumptions remain the same with the second dimension (θ) being the direction of symmetry and $\boldsymbol{Q}$ component values changed accordingly.

Another commonly employed order parameter is the director $\boldsymbol{n}$. From Equation 3.2, it is clear that $\boldsymbol{n}$ is a simplified form of $\boldsymbol{Q}$. When the molecular alignment is uniaxial and q is approximately constant, $\boldsymbol{n}$ describes the local average orientation of molecules well. These assumptions require that the flow in the nematic is slow, and distortion in the $\boldsymbol{n}$ field is small. Topological defects show up as singularities in the vectorial order parameter $\boldsymbol{n}$ field.

3.2.2 Theories for the hydrodynamics of bulk LC flow

All dynamic theories for LC flow share the following common features, some of which are universal to describing complex fluids in general. A complete theory consists of an evolution equation describing the microstructure in terms of an order parameter, and a stress tensor representing the additional forcing on the fluid by the microstructure. The evolution equation arises through the relaxation of total elastic energy in the nematic. The origin of elastic energy can be classified into two types: short-range distortion of the local molecular distribution (*microelasticity*) and non-local, long-range distortion of the orientation of molecules (*distortional elasticity*). The former only depends on the order parameter, and the latter depends on the gradient of the order parameter. The stress tensor must obey the first law of thermodynamics. It will augment the total stress in the Navier-Stokes equation.

The classical theory for LC hydrodynamics is the Leslie-Ericksen (LE) theory based on the director $\boldsymbol{n}$. For detailed accounts of the LE theory, see de Gennes and Prost [38]. Here we only point out that due to the vectorial nature of $\boldsymbol{n}$, molecular elasticity is neglected. Thus the LE theory only applies to low-distortion, weak-flow limits. This is generally not suitable for flows that are strongly correlated to defects. It also brings about challenges in numerical calculation by introducing singularities in the $\boldsymbol{n}$ field. One idea of remedy is to allow the degree of alignment to vary [49]. Lin [93], Lin and Liu [94] introduced a Landau-Ginzburg approximation to regularize the defect cores in a simplified LE theory. Near defect cores in a small region characterized by length scale δ, the length $|\boldsymbol{n}|$ falls below 1 at the expense of an elastic energy penalty. This scheme was successfully applied in simulations of simplified LE bulk dynamics [96], and the phase-field calculations by Yue et al. [181, 183], Zhou et al. [188, 189]. However, the regularized LE theory suffers from flaws in its physics. In the limit $\delta \to 0$, this model only permits isolated point defects of winding numbers 1 or -1 [20]. Defects of half-integer strengths (i.e., line defects) must reside on domain boundaries. Indeed, Zhou et al. [188] predicts a surface ring rather than a Saturn ring in their simulations. Another manifestation is that the theory admits defects of integer strength in 2D planar geometry. It is at odds with calculations using more general tensorial theories, which predict that integer-strength defects are energetically unstable in 2D and will split into a pair

of half-strength defects [57] (see next paragraph). This also limits the applicability of the work carried out in, e.g., Zhou et al. [189]. There the chaining of particle-defect dipoles was a result of this artificial dynamics. Moreover, although less of an essential issue, error and convergence of numerical approximations will depend on the arbitrary parameter δ [96].

In contrast, a tensorial order parameter such as $\boldsymbol{Q}$ in Equation 3.1 is not limited to uniaxial states. In defect cores and other regions where rotational symmetry is lost from the molecular distribution $\psi(\boldsymbol{u})$, $\boldsymbol{Q}$ remains smooth and bounded. There is no undesirable physics such as the removal of Saturn rings introduced by artificial regularizations. Hence it is necessary to consider theories based on the more general tensorial order parameters.

There are many theories based on the $\boldsymbol{Q}$ tensor for nematic hydrodynamics. Some are of phenomenological origin [19, 124, 136, 159, 161]. Almost all of them start from the Landau-de-Gennes expansion of the free energy in terms of powers of the order parameter $\boldsymbol{Q}$, and then derive the evolution equation through some formalism governed by thermodynamic laws. Other models are from kinetic approaches [43, 54, 66, 109, 176]. They begin by postulating elementary interaction potentials between molecules, usually in a mean-field setting. The resulting Fokker-Planck equation (also called the Smoluchowski equation) is integrated in the molecular configuration space to arrive at an evolution equation for $\boldsymbol{Q}$. Usually an assumption is needed to close the equation system because higher-order moments of the distribution function $\psi(\boldsymbol{u})$ often arise [53]. Phenomenological theories enjoy simpler mathematical forms which are more amenable to numerical treatment, while kinetic theories have a clearer physical picture and fewer empirical material parameters.

Overall, all these theories give the same qualitative results. See Willman [177] and compare Tóth et al. [172] with Svenšek and Žumer [166]. Nevertheless, these theories cannot recover one another and have different quantitative predictions. For example, the kinetic theory developed by Feng et al. [54] predicts point defects in 3D, while under a phenomenological theory using the Landau-de-Gennes energy the point defect opens up to a small ring [58, 141]. So far there has not been any experimental evidence refined enough to judge the validity of these hydrodynamic models. A comparison between them theoretically or experimentally is beyond the

scope of this thesis.

3.2.3 The Beris-Edwards theory for dynamic LC flow

We choose the Beris-Edwards (BE) theory [19, 39, 40, 46, 47] since it appears to be the most widely applied model. We also prefer the mathematically simple form of the distortional elasticity terms in the equations thanks to the phenomenological nature. This reduces numerical difficulties. Note that the phase-field framework we use does *not* depend on the specific hydrodynamic model chosen for the LC. In this sub-section, I summarize the BE theory in the context of our study.

The free energy density in the nematic can be expressed as

$$f_b = \frac{A}{2}Q_{ij}Q_{ij} + \frac{B}{3}Q_{ij}Q_{jk}Q_{ki} + \frac{C}{4}(Q_{ij}Q_{ij})^2 + \frac{L_1}{2}(\partial_i Q_{jk})(\partial_i Q_{jk}). \quad (3.7)$$

The subscript b highlights it is the elastic energy density in the bulk of LC. Here $A,\ B,\ C$ are material property coefficients, and L_1 is the bulk elastic constant. The first three terms constitute the celebrated Landau-de-Gennes (LdG) free energy, which describes microelasticity and how local molecular distribution relaxes. The values of $A,\ B,\ C$ determine the local orientational configuration of the LC molecules at equilibrium. Since we are only concerned with thermotropic LCs at a fixed temperature in this thesis, $A,\ B,\ C$ are constants. Lyotropic nematic LCs can be described by making $A,\ B,\ C$ dependent on concentration (see Section 3.1.1). Minimizing the microelasticity part of f_b under the uniaxial assumption gives the equilibrium scalar order parameter

$$q_e^{\pm} = \frac{3}{4}\left(-\frac{B}{3C} \pm \sqrt{\left(\frac{B}{3C}\right)^2 - \frac{8A}{3C}}\right). \quad (3.8)$$

Roughly speaking, in a nematic with relatively strong interaction energy and thus better alignment, only the "+" solution is admissible. In this thesis, we only consider this parameter regime. Thus, we use

$$q_e = \frac{3}{4}\left(-\frac{B}{3C} + \sqrt{\left(\frac{B}{3C}\right)^2 - \frac{8A}{3C}}\right). \quad (3.9)$$

The last term in Equation 3.7, which is non-local, is for distortional elasticity and describes relaxation of long-range orientation distortions. We have applied the common one-constant approximation for simplicity, i.e., the different distortion modes share the same elastic constant [38]. The total bulk free energy in a nematic-filled domain Ω is thus

$$F_b = \int_\Omega \frac{A}{2} Q_{ij}Q_{ij} + \frac{B}{3} Q_{ij}Q_{jk}Q_{ki} + \frac{C}{4}(Q_{ij}Q_{ij})^2 + \frac{L_1}{2}(\partial_i Q_{jk})(\partial_i Q_{jk})\, dV. \tag{3.10}$$

In the BE theory, the evolution equation of $\boldsymbol{Q}$ and the LC stress tensor are obtained by generalizing and applying Poisson brackets to dissipative systems [19, 46]. Poisson brackets are operators which reflect symmetry in the underlying physical system, such as conservation of energy and frame indifference. $\boldsymbol{Q}$ is governed by

$$\frac{\partial \boldsymbol{Q}}{\partial t} + \boldsymbol{v} \cdot \nabla \boldsymbol{Q} = \boldsymbol{S}(\nabla \boldsymbol{v}, \boldsymbol{Q}) + \Gamma \boldsymbol{H}(\boldsymbol{Q}, \nabla \boldsymbol{Q}), \tag{3.11}$$

where $\boldsymbol{v}$ is the velocity vector. The tensor $\boldsymbol{S}$ describes the local molecular distribution being rotated, sheared and stretched by the underlying flow. In the bulk of a single nematic phase, it has the following expression

$$\begin{aligned} \boldsymbol{S}_b(\nabla \boldsymbol{v}, \boldsymbol{Q}) =& (\xi \boldsymbol{D} + \boldsymbol{\Omega}) \cdot \left(\boldsymbol{Q} + \frac{1}{3}\boldsymbol{I} \right) + \left(\boldsymbol{Q} + \frac{1}{3}\boldsymbol{I} \right) \cdot (\xi \boldsymbol{D} - \boldsymbol{\Omega}) \\ & - 2\xi \left(\boldsymbol{Q} : (\nabla \boldsymbol{v})^\intercal \right) \left(\boldsymbol{Q} + \frac{1}{3}\boldsymbol{I} \right), \end{aligned} \tag{3.12}$$

where $\boldsymbol{D}$ is the rate of deformation tensor, and $\boldsymbol{\Omega}$ is the vorticity tensor:

$$\boldsymbol{D} = \frac{1}{2}\left((\nabla \boldsymbol{v})^\intercal + \nabla \boldsymbol{v} \right), \quad \boldsymbol{\Omega} = \frac{1}{2}\left((\nabla \boldsymbol{v})^\intercal - \nabla \boldsymbol{v} \right). \tag{3.13}$$

ξ is a material property parameter which plays a role in determining if the nematic is flow-aligning or tumbling [38, 40].

Γ is the *collective rotational diffusion coefficient* and will be taken as a constant in this thesis (for an example where Γ is not constant, see [e.g., 41]). The tensor $\boldsymbol{H}$ is also called the *molecular field*. It describes how the $\boldsymbol{Q}$ profile is rotated and

deformed by the nematic relaxation.

$$\boldsymbol{H} = -\frac{\delta F}{\delta \boldsymbol{Q}} + \frac{1}{3}\,\mathrm{tr}\left(\frac{\delta F}{\delta \boldsymbol{Q}}\right) I. \tag{3.14}$$

$\delta F/\delta \boldsymbol{Q}$ is the variational derivative of the functional F with respect to $\boldsymbol{Q}$, which results in a second-rank tensor

$$\frac{\delta F}{\delta Q_{ij}} = \frac{\partial f}{\partial Q_{ij}} - \partial_k \left(\frac{\partial f}{\partial(\partial_k Q_{ij})}\right). \tag{3.15}$$

In the special case where only a nematic phase is present, we can use the bulk free energy F_b solely, and obtain

$$\boldsymbol{H}_b = \boldsymbol{M}(\boldsymbol{Q}) + \nabla \cdot (L_1 \nabla \boldsymbol{Q}), \tag{3.16}$$

where $\boldsymbol{M}$ is a polynomial in $\boldsymbol{Q}$

$$\boldsymbol{M}(\boldsymbol{Q}) = -A\boldsymbol{Q} - B\boldsymbol{Q}\cdot\boldsymbol{Q} - \frac{B}{3}(\boldsymbol{Q} : \boldsymbol{Q}^{\mathsf{T}})\boldsymbol{I} - C(\boldsymbol{Q} : \boldsymbol{Q}^{\mathsf{T}})\boldsymbol{Q}. \tag{3.17}$$

Note that Both $\boldsymbol{S}_b$ and $\boldsymbol{H}_b$ are symmetric.

The LC stress tensor in the BE theory

$$\begin{aligned}(\tau_p)_{ij} =& -\xi H_{ik}\left(Q_{kj} + \frac{1}{3}\delta_{kj}\right) - \xi\left(Q_{ik} + \frac{1}{3}\delta_{ik}\right)H_{kj} \\ &+ 2\xi\left(Q_{ij} + \frac{1}{3}\delta_{ij}\right)(Q_{kl}H_{kl}) - (\partial_j Q_{kl})\frac{\partial f}{\partial\left(\partial_i Q_{kl}\right)} \\ &+ H_{ik}Q_{kj} - Q_{ik}H_{kj}.\end{aligned} \tag{3.18}$$

Since rod-like molecules in the nematic are subject to torques, the LC stress tensor $\boldsymbol{\tau}_p$ is not symmetric, indicated by the antisymmetric part in the last line of the above equation.

The BE theory can be reduced in different limits to the LE theory and Doi's kinetic theory [19, 40, 46].

Besides $\boldsymbol{\tau}_p$, we assume that the rest of the stress in the bulk of the fluid can be described by the Newtonian stress $-p\boldsymbol{I} + 2\eta\boldsymbol{D}$ where p denotes pressure and η is

a viscosity (see Equation 4.59).

I will address the boundary conditions in Section 4.3 where we modify the above equations to arrive at the phase-field formulation.

Chapter 4

Methodology: multiphase flow formulations

In this chapter, we first review briefly numerical methods for multiphase flows based on continuum models. Subsequently, I present the mathematical theories for ferrofluid (Section 4.2) and liquid crystals (Section 4.3) in the volume-of-fluid and phase-field formalisms, respectively. The former follows well-developed results in literature, while the latter is developed by this thesis. The numerical discretization will be covered in the end.

4.1 Computational modeling of interfacial flows

4.1.1 Introduction

From the methodology point of view, there are two almost universal challenges to computational studies of interfacial dynamics of complex fluids. First, a scheme is needed to represent and track the moving interface. Related to the scheme is how to impose Boundary Conditions (BCs) across the interface, particularly surface tension. The second challenge comes from incorporating the complex rheology in a multiphase formalism. The presence of complex fluids typically causes additional stress and modifies the flow. It has two consequences. On one hand, one needs to solve the evolution of the microstructure of the fluids and the complex stress. It

sometimes requires complicated approaches. On the other hand, the complex stress changes force balance conditions across the interface. In particular, for certain fluids such as liquid crystals, additional interfacial rheology arises from special microstructure configurations dictated by the interface. Complexities involving the interfacial forces are harder to deal with because they exacerbate the issues of calculating the forces accurately and in a balanced way.

Besides these conceptual challenges, on the discrete level, a difficulty that usually arises is the design of accurate and efficient numerical schemes to solve the resulting governing equations. Owing to the complexity of these methods, numerical discretization often needs to be taken into account together with the formulation of the model on the continuum level from the start.

In the following, I review a few popular methods for computing interfacial flows, in the context of complex fluids. The general remarks above are also illustrated in these examples. Note that computations of interfacial flows have been studied for decades and there is vast literature dedicated to the development, analysis, and application of these methods. In this brief chapter, I have no intention to be exhaustive and to cover all the variants and their details. We restrict to continuum methods based on describing the macroscopic behaviour of fluids. Molecular Dynamics (MD) methods are based on microscopic behaviour of particles, and are thus beyond our scope. So is the Lattice Boltzmann Method (LBM) which relies on kinetic models of ensembles of fluid molecules. We also restrict to mesh-based methods as they are currently the most widely used. Recently, mesh-free techniques such as the Smoothed Particle Hydrodynamics (SPH) method [180] and the Material Point Method (MPM) [162] have received growing attention. These methods use discrete particles to represent fluid (and solid). The Lagrangian nature is particularly suitable to model topological changes. However, incorporating interfacial forces is non-trivial, and their application in interfacial flows of complex fluids is limited. For comprehensive reviews on numerical methods of multiphase flows, see [149, 178]. The recent review paper by Popinet [132] treats the same topic from the perspective of numerical models for surface tension.

Consider a generic flow field with two immiscible fluids separated by a moving interface (Figure 4.1). Microscopically, it is a thin mixing region governed by intermolecular forces. However, the thickness of this mixing layer is far smaller

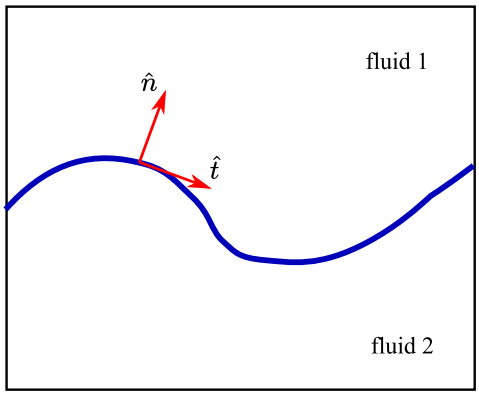

Figure 4.1: Generic multiphase flow problem with two immiscible fluids separated by a sharp moving interface. $\hat{\boldsymbol{n}}$ and $\hat{\boldsymbol{t}}$ are the unit normal vector and a unit tangential vector to the interface, respectively.

than the usual grid or particle resolution of a numerical description. Also we are only interested in continuum models. Hence the interface is considered sharp with a vanishing thickness.

The methods we look at can be loosely classified in Table 4.1. In general,

	Eulerian	**Lagrangian**
Sharp-interface methods	Volume-Of-Fluid (VOF) Level Set (LS)	Interface-tracking
Diffuse-interface methods	Phase-field (PF)	(Not applicable)

Table 4.1: Commonly used numerical methods for multiphase flows.

Lagrangian methods track the interface explicitly through various objects, such as mesh points or markers. In *Eulerian methods*, the fluids move through a fixed mesh, with the interface implicitly represented by an evolving scalar field which is approximated on the mesh.

4.1.2 Interface-tracking methods

Perhaps the most natural method is to deploy discrete *markers* on the interface explicitly, following the velocity field of the fluids. This can be coupled with a

fixed Eulerian mesh on which the fluid motion is computed [133, 170]. As the flow field evolves, the marker distribution could be distorted, which needs to be restored. Another type of this method uses mesh points as markers (*moving mesh*). In order to accommodate large deformation of the mesh caused by fluid motion, one can propagate the deformation along the mesh network to maintain overall meshing quality, provided that the marker points stay on the interface. This leads to the *Arbitrary Lagrangian-Eulerian* (ALE) methods [69]. The concepts for both the markers and ALE techniques are shown in Figure 4.2. Because the location and shape of the interface are known explicitly, computing geometrical properties of the interface and imposing BCs are relatively easy. The interface stays sharp throughout the calculation. However, the numerical procedure is either challenging or costly with strong flows and large deformation.

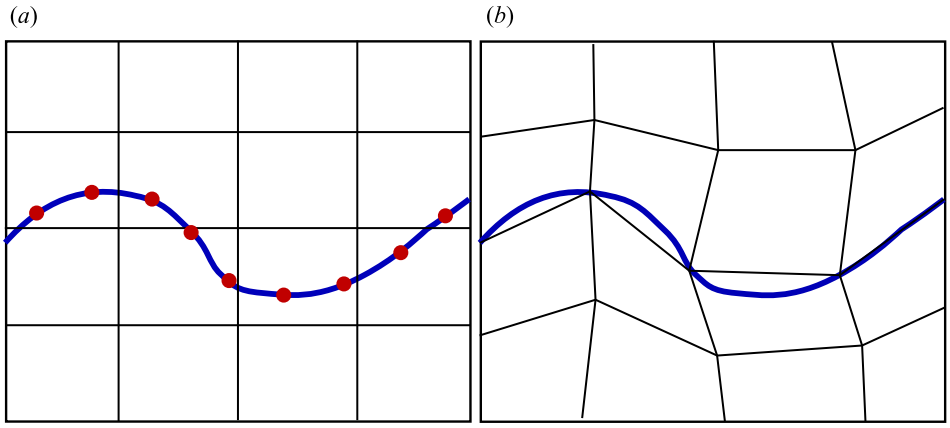

Figure 4.2: Interface-tracking methods. (*a*) Markers are attached to the moving interface which evolves through a fixed Eulerian mesh. (*b*) ALE. Mesh points are used as markers while the grid deforms and relaxes to maintain mesh quality.

4.1.3 Sharp-interface Eulerian methods

Inevitably all methods based on a Eulerian grid have a diffuse interface after numerical discretization, with the interfacial thickness at a size of at least one grid cell. By sharp-interface Eulerian methods, we consider approaches in which the mathematical description of the interface is sharp on the continuum level. This

includes the *Volume-Of-Fluid* (VOF) methods [68, 91, 131] and the *Level Set* (LS) methods [125, 126, 165]. Both methods are based on an advection equation for a scalar function c describing the local phase.

$$\frac{\partial c}{\partial t} + \boldsymbol{v} \cdot \nabla c = 0. \tag{4.1}$$

In VOF, c is called the "colour function". In a two-phase flow, it is defined as the local volume fraction of one of the two fluids. Therefore, on the continuum level, it takes the value 0 on one side of the interface, and 1 on the other side, with a jump across the interface. Equation 4.1 describes the mass conservation of both phases. It can then be discretized using different methods. For example, with finite volume discretization using cell-centred values, the discrete c field represents volume fraction in mesh cells (Figure 4.3*a*). The interface needs to be reconstructed from the c field. Figure 4.3(a) shows a commonly used approximation method called Piecewise Linear Interface Construction (PLIC).

In LS, c is called the "level set function", which is an artificial scalar function defined in the computational domain. Its zero level set is the interface. It is usually initialized as the signed distance function from the interface. Equation 4.1 enforces that the motion of the interface follows advection by the flow field. The interface location can be obtained by interpolating the c function. Figure 4.3(b) displays the concept of the LS approach. The level set function is shown in the third dimension additional to the 2D computational domain by the gray shade.

In VOF and LS, surface tension is usually represented by a body force or stress term in the Navier-Stokes equation [24, 81], involving δ-functions supported on the interface. In the discretization, the interfacial δ-function needs to be approximated, typically by classical functions supported in a finite number of mesh cells near the interface. With finite element methods, the interfacial δ-function results in line or surface integrals on the interface. These integrals are again approximated discretely [132, 178].

The implicit representation in Eulerian methods makes it rather easy to handle large deformation and topological changes. Using a fixed mesh is also less costly than Lagrangian methods. There are, however, disadvantages. Challenges arise when imposing BCs and calculating interfacial forces. For instance, in VOF, due

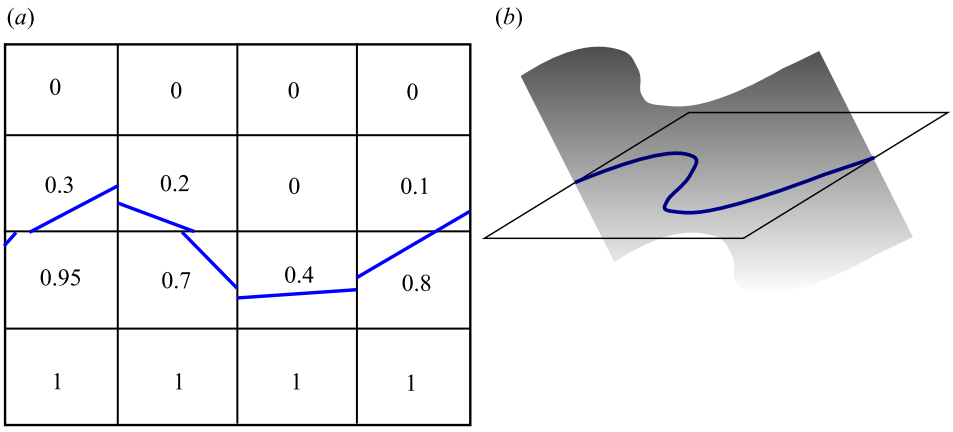

Figure 4.3: Sharp-interface Eulerian methods. (*a*) VOF. The values represent the volume fraction of one of the fluids in each mesh cell. The interface is reconstructed using the PLIC approach. (*b*) LS. The level set function value is visualized by the gray shade, and the moving interface in the 2D domain is the zero level set of this function.

to the uncertainty in interface location and geometry, calculating surface tension accurately and preserving force balance across the interface are non-trivial. Great care needs to be taken to avoid "spurious currents" in VOF methods [131, 142] (also existing in other methods). This is even more pronounced when incorporating complex fluids in the VOF or LS formalisms. The force balance across the interface is modified by complex rheology.

VOF and LS methods each have pros and cons of their own. Designed to track fluid volume, VOF techniques are naturally good at mass conservation. However, the discrete c field is subject to smearing by numerical error. One way to limit this effect is to advect the reconstructed interface directly based on local velocity and subsequently update the c field in the next time step [131]. This geometric scheme ensures that the discrete interface is not smeared to span more than one mesh cell. In contrast, in LS methods the interface stays sharp up to numerical error. On the other hand, the distortion to the level set function during interface evolution could cause large error in total mass. Reinitialization is required to restore mass conservation [164].

4.1.4 Diffuse-interface methods

The *Phase-Field* (PF) method assumes that the interface has a finite thickness across which the fluids mix and all variables change smoothly. This starts from the continuum description of the multiphase flow, and is therefore a diffuse-interface method. When applied to immiscible fluids, the thickness of the interfacial region used in the numerical model is usually much larger than physically realistic mixing areas. Thus it should be considered as a regularization to the sharp-interface picture more than a physically consistent model. The PF method also employs a fixed Eulerian mesh, combined with a phase variable ϕ to describe different fluids. Figure 4.4 shows the concept of the PF method in a two-phase flow. In this example, we assign $\phi = -1$ to one of the fluids and $\phi = 1$ to the other.

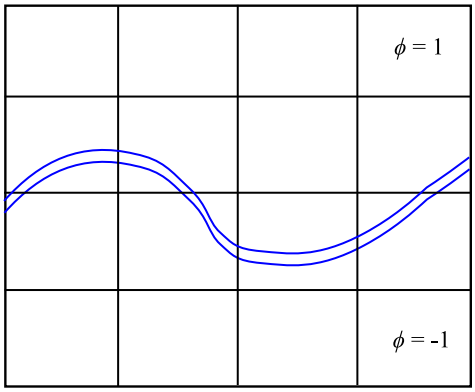

Figure 4.4: The phase-field method. The two fluids are separated by a thin (relative to flow length scales) interfacial region in which they mix and all variables change smoothly.

The PF method is based on energetic arguments concerning the mixing of the two fluids. Here we present a widely used variant (also used in this thesis) [181]. We introduce a mixing energy density for the two-fluid mixture,

$$f_m = \frac{\lambda}{2}|\nabla\phi|^2 + \frac{\lambda}{4\epsilon^2}\left(\phi^2 - 1\right)^2, \tag{4.2}$$

where λ is the mixing energy strength, and ϵ is a constant. The first term (gradient term) favours the mixing of the fluids, while the second is a double-well potential that favours phase separation. An equilibrium phase profile arises under the com-

petition between these two terms. In an infinite domain in 1D, minimizing the total mixing energy gives

$$\phi_e(x) = \tanh\left(\frac{x}{\sqrt{2}\epsilon}\right). \tag{4.3}$$

It shows that ϵ is a capillary width controlling the span of the interfacial region. The ϕ field is governed by an advection-diffusion equation, i.e., the Cahn-Hilliard (CH) equation, where the diffusive flux is the gradient of the chemical potential μ.

$$\frac{\partial \phi}{\partial t} + \boldsymbol{v} \cdot \nabla \phi = \gamma \nabla^2 \mu, \tag{4.4}$$

where γ is called the *mobility* (dimension of length^4/(force$\times$time)). The chemical potential μ is defined as

$$\mu = \frac{\delta \int_\Omega f_m \, dV}{\delta \phi} = \lambda \left(-\nabla^2 \phi + \frac{\phi(\phi^2 - 1)}{\epsilon^2}\right). \tag{4.5}$$

The CH equation describes the minimization of the total mixing energy, subject to flow advection. The mixing energy causes a stress in the fluid, which can be written as a stress term [181] or a body force term [185] in the Navier-Stokes equation. It is the diffuse-interface version of surface tension.

The non-advective CH equation was initially proposed to model phase separation in a spinodal decomposition [27]. However, as mentioned above, for immiscible fluids far from critical events, the realistic interfacial thickness is at a length scale much smaller than what the mesh can resolve. Then what is the relationship between the PF model with the sharp-interface picture in two-phase flows as constructed in Figure 4.1?

The efficacy of the PF method as a general technique for multiphase flows hinges on the following two factors.

(i) The *sharp-interface limit*. The sharp-interface picture emerges as the asymptotic limit of the PF model as the capillary width $\epsilon \to 0$. This has been discussed and established through a large body of literature [e.g., 9, 72, 95].

(ii) Recovery of macroscopic surface tension. The theoretical existence of the sharp-interface limit does not address the attainment of this limit in com-

putational practice, in particular the choice of numerical parameters in the CH equation to recover interfacial forces, such as surface tension. In order to bridge the macroscopic sharp-interface model to the PF model, Yue et al. [181] proposed a relationship based on the assumption of local thermodynamic equilibrium across the interface:

$$\sigma = \frac{2\sqrt{2}}{3}\frac{\lambda}{\epsilon}, \tag{4.6}$$

where σ is the surface tension coefficient.

In light of the first condition above, one needs to use a small enough capillary width ϵ to be close to the sharp-interface limit, and resolve the thin transition layer with sufficient grid points. For the second requirement, besides a small ϵ value, one has also to be judicious in selecting a value for the mobility γ. The authors in [72, 181, 185] have realized this issue but not provided a clear theoretical interpretation. Here we point out that the attainment of the sharp-interface limit is made possible by the separation of time scales in the CH diffusion [128]. Asymptotically with a vanishing ϵ, on the time scale of $O(\epsilon^2/\gamma)$, the interface is stabilized into equilibrium with the hyperbolic tangent profile of ϕ_e in Equation 4.3. On $O(1/(\epsilon\gamma))$ time scale, CH diffusion drives a curvature-dependent flow in ϕ (Mullins-Sekerka flow [117]). Our choice of γ in combination of a small ϵ aims to exploit this separation and put the flow time scale intermediate between these two time scales. When this condition is satisfied, the stabilized diffuse interface allows Equation 4.6 to be used, while being free from dampening by long-term CH diffusion. In other words, the interface motion is governed by almost pure advection of the fluid flow under the correct forcing consistent with macroscopic surface tension, i.e., near the sharp-interface limit. Best practices regarding approaching the sharp-interface limit have been proposed and demonstrated in a series of numerical experiments [181, 185, 186, 190]. See also Section 4.3 for how we choose to incorporate liquid crystal elastic energies under this principle.

As a Eulerian method, the PF technique enjoys the same benefits of implicit tracking of the interface, including the ease of handling topological changes. As an energetic approach, it has further advantages over sharp-interface Eulerian methods. First, critical events are easily accounted for in the framework. For exam-

ple, the incorporation of moving contact lines is natural as the stress singularity is removed [187]. In methods such as VOF or LS, ad-hoc treatments are usually required to accommodate dynamic contact lines. Second, the PF method is particularly suitable to model complex fluids, as long as the rheology can be described by a free energy. Through variational principles, the complex stress tensor including interfacial forcing can be readily derived. This power has been shown in [181, 182, 188, 189]. There are two disadvantages of the PF method, however. For one, the CH equation is of fourth order and expensive to solve numerically. In addition, the interfacial region needs a highly refined mesh, typically requiring a non-uniform grid in the computational domain. In cases with large motion of the interface, an efficient mechanism to adaptively refine and coarsen the mesh is needed. For the other, the CH diffusion brings about artificial dynamics, such as drop shrinkage and mass loss [186] and long-term Mullins-Sekerka flow which could dampen the advection of the velocity field. To mitigate these undesirable effects, a careful choice of parameters needs to be exercised to approach the sharp-interface limit.

In the two sections below, we apply the general knowledge reviewed here to our two specific problems. We present descriptions of multiphase flows of ferrofluid and liquid crystals, respectively.

4.2 The volume-of-fluid formulation of ferrofluid drop dynamics

The BCs across the moving interface between the two fluids are standard:

$$[\![\boldsymbol{v}]\!] = 0, \;\; \boldsymbol{n} \cdot [\![\boldsymbol{\tau}_\eta + \boldsymbol{\tau}_m]\!] \cdot \boldsymbol{t} = 0, \;\; [\![\varphi]\!] = 0, \;\; [\![\mu \boldsymbol{H}]\!] \cdot \boldsymbol{n} = 0. \tag{4.7}$$

where $[\![\cdot]\!]$ denotes the interfacial jump of a quantity. $\boldsymbol{n}$ and $\boldsymbol{t}$ are the unit normal and tangential vectors, respectively, and $\boldsymbol{\tau}_\eta = 2\eta \boldsymbol{D}$ is the viscous stress tensor. The normal component of the stress has a jump across the interface due to interfacial tension:

$$\boldsymbol{n} \cdot [\![\boldsymbol{\tau}_\eta + \boldsymbol{\tau}_m]\!] \cdot \boldsymbol{n} + [\![p]\!] = \sigma\kappa, \tag{4.8}$$

where σ is the constant interfacial tension and κ the curvature.

The VOF formulation modifies the governing equations in Section 2.2 in light of the above interfacial BCs. First, the interfacial tension is accounted for through a body force term that acts only on the interface [7, 131]:

$$\rho \left(\partial_t \boldsymbol{v} + \boldsymbol{v} \cdot \nabla \boldsymbol{v}\right) = -\nabla p + \nabla \cdot (2\eta \boldsymbol{D}) + \nabla \cdot \boldsymbol{\tau}_m + \sigma\kappa\delta_s \boldsymbol{n}, \tag{4.9}$$

where δ_s is the Dirac delta function supported on the interface. The volume fraction function $c(\boldsymbol{x}, t)$ is introduced such that c takes the value of 1 in the ferrofluid and 0 in the surrounding medium (see Section 4.1). c evolves according to Equation 4.1, which is repeated here for convenience:

$$\partial_t c + \boldsymbol{v} \cdot \nabla c = 0. \tag{4.10}$$

We choose the following reference scales: the initial radius of the circular drops r_0, the matched density of both fluids ρ, the viscosity of the surrounding medium η_s, and the magnitude of the uniform external magnetic field H_0. The reference time scale is chosen to be $t_0 = \sqrt{\rho r_0^2 / \mu_0 H_0^2}$. It follows that the reference velocity scale is $v_0 = r_0/t_0$, and the reference pressure scale is $p_0 = \mu_0 H_0^2$. Denoting all dimensionless variables using the same symbols, the dimensionless Navier-Stokes

equation becomes

$$(\partial_t \boldsymbol{v} + \boldsymbol{v} \cdot \nabla \boldsymbol{v}) = -\nabla p + \sqrt{\frac{1}{La_m}} \nabla \cdot (2\eta \boldsymbol{D}) + \nabla \cdot \boldsymbol{\tau}_m + \frac{1}{Bo_m} \kappa \delta_s \boldsymbol{n}. \quad (4.11)$$

The magnetic Laplace number La_m

$$La_m = \frac{\mu_0 H_0^2 \rho r_0^2}{\eta_s^2} \quad (4.12)$$

represents the ratio of the magnetic and inertial forces over the viscosity force, and can be interpreted as the square of a Reynolds number. The magnetic Bond number Bo_m represents the ratio of magnetic force to interfacial tension,

$$Bo_m = \frac{\mu_0 H_0^2 r_0}{\sigma}. \quad (4.13)$$

Other dimensionless numbers that govern the problem are as follows: the dimensionless frequency of the driving field,

$$f = \frac{1}{T} \sqrt{\frac{\rho r_0^2}{\mu_0 H_0^2}}, \quad (4.14)$$

with T being the period of rotation of the field; the viscosity ratio

$$\xi = \frac{\eta_d}{\eta_s}; \quad (4.15)$$

and the magnetic (volume) susceptibility of the ferrofluid

$$\chi = \frac{\mu_d}{\mu_0} - 1. \quad (4.16)$$

The magnetic field strength in the current study is sufficiently low that we can ignore the rotational viscosity of the ferrofluid [155] and assume linear magnetization. Hence ξ and χ are both constants. The latter implies that the magnetic force $\nabla \cdot \boldsymbol{\tau}_m = -(H^2/2)\nabla\mu$ amounts effectively to a surface force acting on the interface only. From this point on, unless stated otherwise, we use dimensionless variables normalized by the reference scales given above.

The VOF computation is carried out using the open-source software package Gerris [101, 130, 131], which uses a second-order accurate fractional-step projection method for time marching, and a finite volume spatial discretization with a structured quad/octree grid. Both the time step and mesh are adaptive. The quad/octree grid allows for efficient refinement and coarsening. The discretization of the interfacial tension term $\sigma\kappa\boldsymbol{n}\delta_s$ follows the Continuous-Surface-Force (CSF) approach [24], with the curvature computed by the height-function method. To interpolate the material properties in the interfacial cells, we use simple algebraic average for viscosity and a weighted harmonic mean for the magnetic permeability [7]:

$$\eta = \frac{c\eta_d + (1-c)\eta_s}{\eta_s} = 1 + c\,(\xi - 1)\,, \tag{4.17}$$

$$\frac{1}{\mu} = \left(\frac{c}{\mu_d} + \frac{1-c}{\mu_0}\right)\mu_0 = 1 + c\left(\frac{1}{1+\chi} - 1\right). \tag{4.18}$$

We adapt the EHD module in Gerris by setting the electric permittivity ϵ to the magnetic permeability μ, and the conductivity and free charge density both to zero. In such a VOF formalism, all the BCs across the interface (Equation 4.7-Equation 4.8) are naturally satisfied. For BCs on the outer bounding box, we prescribe the rotating magnetic field and impose no penetration of fluid but free slip on $\partial\Omega$:

$$\boldsymbol{v}\big|_{\partial\Omega}\cdot\boldsymbol{n} = 0,\;\; \boldsymbol{n}\cdot\boldsymbol{\tau}_\eta\big|_{\partial\Omega}\cdot\boldsymbol{t} = 0,\;\; \left.\frac{\partial\varphi}{\partial n}\right|_{\partial\Omega} = -H_n(t), \tag{4.19}$$

where $H_n(t)$ is the normal component of the time-dependent magnetic field strength, which will be substantiated in Chapter 5.

4.3 The phase-field formulation for elasto-capillary flows of liquid crystals

4.3.1 Introduction

In this section, we consider a pair of isotropic and nematic fluids and develop a phase-field (PF) formulation for this two-phase flow. Again as stated in Section 4.1, in our ideal model, the two fluids are immiscible with a sharp interface between them. The motion of the interface is purely governed by advection of the flow field. The PF model is meant to *approximate* such a description.

We follow the procedure outlined in Yue et al. [181] closely. I first construct a new diffuse-interface version of the free energy for LC anchoring, and then derive interfacial terms due to anchoring in the equation of $\boldsymbol{Q}$ and the stress tensor. These constitute the core contribution of our PF formulation. All the equations are thus generalized to apply globally to the two-fluid mixture.

4.3.2 Free energies

Our basic assumption is that the effect of complex rheology including interfacial rheology, in this case the nematic LC, is additive to the effect of conventional surface tension in the sense of free energies.

We introduce a phase variable ϕ to mark the different fluids. $\phi = -1$ denotes the nematic and $\phi = 1$ denotes the isotropic fluid. The mixing of these two fluids in the thin interfacial region is described by the standard Landau-Ginzburg energy density which has been introduced in Equation 4.2. We repeat it here for convenience

$$f_m = \frac{\lambda}{2}|\nabla\phi|^2 + \frac{\lambda}{4\epsilon^2}\left(\phi^2 - 1\right)^2, \tag{4.20}$$

It is convenient to impose the anchoring condition on the fluid-fluid interface weakly through an energy penalizing the LC molecules deviating from preferred directions. Here we propose a diffuse-interface version of the anchoring energy analogous to the classical Rapini-Papoular form. The latter has been used by a number of researchers [74, 108, 140, 173]. Compared to other forms of anchoring energy, e.g., in [17, 113], our formulation is more general and flexible. First

consider a sharp interface between a nematic phase and an isotropic fluid. The anchoring energy can be expressed phenomenologically by the Rapini-Papoular surface energy density [120, 139]

$$f_s = \frac{W_s}{2} \left\| \boldsymbol{Q} - q_e \left(\boldsymbol{e}\boldsymbol{e} - \frac{1}{3}\boldsymbol{I} \right) \right\|_F^2, \tag{4.21}$$

where W_s is the surface anchoring energy density, and $\|\cdot\|_F$ is the Frobenius norm. $\boldsymbol{e}$ is the easy direction preferred on the interface. Recall that q_e is the equilibrium scalar order parameter determined by the Landau-de-Gennes (LdG) free energy of the nematic phase (Equation 3.8).

In analogy, in the diffuse-interface picture, we hope to have an anchoring energy of the form

$$\hat{f}_a = \frac{\hat{W}}{2} \left\| \boldsymbol{Q} - q_e \left(\boldsymbol{e}\boldsymbol{e} - \frac{1}{3}\boldsymbol{I} \right) \right\|_F^2, \tag{4.22}$$

where $\hat{W}$ is a volume energy density. We settle on the following form

$$f_a = \frac{W}{2} |\nabla\phi|^4 \left\| \boldsymbol{Q} - q_e \left(\boldsymbol{e}\boldsymbol{e} - \frac{1}{3}\boldsymbol{I} \right) \right\|_F^2. \tag{4.23}$$

W is a constant with the dimension of energy$\times$length. We will derive W from W_s below. The factor $|\nabla\phi|^4$ avoids singularities in the expression of $\boldsymbol{e}\boldsymbol{e}$, which will become obvious once we substantiate the formula in two special cases below.

(i) *Homeotropic anchoring.* The easy direction is the unit normal vector $\hat{\boldsymbol{n}} = \nabla\phi/|\nabla\phi|$ of the interface (or its negative). Hence

$$f_a^{\perp} = \frac{W}{2} \left\| |\nabla\phi|^2 \boldsymbol{Q} - q_e \left(\nabla\phi\nabla\phi - \frac{1}{3}|\nabla\phi|^2 \boldsymbol{I} \right) \right\|_F^2. \tag{4.24}$$

(ii) *Planar anchoring in 2D.* In this thesis, we consider only a 2D geometry with symmetry in a third dimension (see Section 3.2.2). The planar anchoring condition requires that $\boldsymbol{e}$ is along the tangential direction to an interface. In the case of 2D axisymmetric geometry, this condition corresponds to the so-called monostable planar anchoring in the r-z plane in a cylindrical frame. In 2D planar geometry, the easy direction can be written as $(\hat{n}_2, -\hat{n}_1, 0)$ (or

its negative) where $\hat{n}_i$ is the i-th component of the vector $\hat{\boldsymbol{n}}$. It follows that

$$f_a^{\parallel} = \frac{W}{2} \left\| |\nabla\phi|^2 \boldsymbol{Q} + q_e \left(\nabla\phi\nabla\phi - \frac{1}{3}|\nabla\phi|^2 \boldsymbol{J} \right) \right\|_F^2, \tag{4.25}$$

where the tensor $\boldsymbol{J}$ can be written as

$$\boldsymbol{J} = \begin{bmatrix} 2 & 0 & 0 \\ 0 & 2 & 0 \\ 0 & 0 & -1 \end{bmatrix}, \tag{4.26}$$

which is rotationally symmetric in the 1-2 coordinate plane. In 2D axisymmetric geometry with cylindrical coordinates, one just needs to swap the second and third coordinates above.

Following these, the total free energy of the two-phase mixture is

$$F = \int_\Omega f(\phi, \boldsymbol{Q}, \nabla\phi, \nabla\boldsymbol{Q})\, dV = \int_\Omega f_m + \frac{1-\phi}{2} f_b + f_a\, dV. \tag{4.27}$$

Now I derive the anchoring strength parameter W. Consider a sharp interface S_W in some domain Ω_W, and its corresponding diffuse-interface picture. We might as well assume the special case where $\|\boldsymbol{Q} - q_e(\boldsymbol{ee} - \boldsymbol{I}/3)\|_F$ is a constant, provided that we make Ω_W sufficiently small. To have the same interfacial anchoring energy,

$$\int_{S_W} \frac{1}{2} W_s\, dS = \int_{\Omega_W} \frac{1}{2} W |\nabla\phi|^4\, dx. \tag{4.28}$$

We can further assume that ϕ is in the equilibrium profile Equation 4.3 across the interfacial thickness, because we are approximating the sharp-interface limit (see more details in Section 4.1). Then ϕ becomes a function in the coordinate x normal to the interface

$$W = \frac{W_s}{\int_{-\infty}^{\infty} (\phi')^4\, dx}. \tag{4.29}$$

Plugging ϕ_e into the above equation gives

$$W = \frac{35}{8\sqrt{2}} W_s \epsilon^3, \tag{4.30}$$

where W bears the dimension of energy$\times$length as expected. The above derivation is similar to that in [181] which bridges the macroscopic surface tension with microscopic parameters in the PF model. This is an advantage of the present model.

Next, all the equations in the BE theory need to be modified in order to be valid globally in the two-phase flow.

4.3.3 Modification of the LC evolution equation

Plugging the augmented free energy functional Equation 4.27 into the general expression for the molecular field $\boldsymbol{H}$ Equation 3.14, we need to introduce two changes in the expression of $\boldsymbol{H}$.

(i) Existing terms in Equation 3.16 and Equation 3.17 remain in the same form except that all material parameters involved need to be multiplied by the concentration $(1-\phi)/2$.

(ii) The anchoring energy f_a in F leads to new terms in $\boldsymbol{H}$. Introducing the dimensionless tensor $\boldsymbol{G}$,

$$\begin{aligned}\boldsymbol{H}_a^{\perp} &= -W\boldsymbol{G}^{\perp} \\ &\coloneqq -W|\nabla\phi|^2\left(|\nabla\phi|^2\boldsymbol{Q} - q_e\left(\nabla\phi\nabla\phi - \frac{1}{3}|\nabla\phi|^2\boldsymbol{I}\right)\right), \qquad (4.31)\\ \boldsymbol{H}_a^{\parallel} &= -W\boldsymbol{G}^{\parallel} \\ &\coloneqq -W|\nabla\phi|^2\left(|\nabla\phi|^2\boldsymbol{Q} + q_e\left(\nabla\phi\nabla\phi - \frac{1}{3}|\nabla\phi|^2\boldsymbol{J}\right)\right). \qquad (4.32)\end{aligned}$$

Following these, we update Equation 3.16 to be

$$\boldsymbol{H} = \frac{1-\phi}{2}\boldsymbol{M} - W\boldsymbol{G} + \nabla\cdot\left(\frac{1-\phi}{2}L_1\nabla\boldsymbol{Q}\right). \qquad (4.33)$$

For Equation 3.11 to apply globally, it has to stay consistent throughout the interfacial region and eventually vanish in the isotropic phase. The left hand side and the new $\boldsymbol{H}$ satisfy this requirement. However, in the isotropic phase, $\boldsymbol{S}(\nabla\boldsymbol{v}, 0) = (2/3)\xi\boldsymbol{D}$. Therefore, postulating the same phenomenology of interpolating ξ with

the nematic concentration, we update Equation 3.12 to be

$$\boldsymbol{S}(\nabla \boldsymbol{v}, \boldsymbol{Q}) = \left(\frac{(1-\phi)\xi}{2}\boldsymbol{D} + \boldsymbol{\Omega}\right) \cdot \left(\boldsymbol{Q} + \frac{1}{3}\boldsymbol{I}\right) \tag{4.34}$$

$$+ \left(\boldsymbol{Q} + \frac{1}{3}\boldsymbol{I}\right) \cdot \left(\frac{(1-\phi)\xi}{2}\boldsymbol{D} - \boldsymbol{\Omega}\right)$$

$$- (1-\phi)\xi \left(\boldsymbol{Q} : (\nabla \boldsymbol{v})^{\intercal}\right) \left(\boldsymbol{Q} + \frac{1}{3}\boldsymbol{I}\right). \tag{4.35}$$

One may have the concern that this is not necessarily consistent with the underlying energetics. But after all, provided that the interface is kept thin and the $\boldsymbol{Q}$ equation vanishes in the isotropic phase, the resulting physics is correct.

With the updated $\boldsymbol{H}$ and $\boldsymbol{S}$, Equation 3.11 remains to be valid. Remark that the symmetry of $\boldsymbol{H}_b$ and $\boldsymbol{S}_b$ is preserved in $\boldsymbol{H}$ and $\boldsymbol{S}$.

We consider four types of boundary conditions (BCs) for the $\boldsymbol{Q}$ equation. Conditions (i-iii) are routinely used in literature.

(i) On some boundaries Γ_{QN}, the gradient of $\boldsymbol{Q}$ vanishes, i.e., $\boldsymbol{Q}$ satisfies the homogeneous Neumann BC. These can be used to mimic infinity.

$$\hat{\boldsymbol{n}} \cdot \nabla \boldsymbol{Q}|_{\Gamma_{QN}} = 0. \tag{4.36}$$

(ii) On boundaries with infinite-strength anchoring Γ_{QD}, $\boldsymbol{Q}$ is specified as the desired function $\boldsymbol{Q}_D$ (Dirichlet BC). Alternative to (i) above, this can also be used on boundaries representing alignment at infinity.

$$\boldsymbol{Q}|_{\Gamma_{QD}} = \boldsymbol{Q}_D. \tag{4.37}$$

(iii) On boundaries with finite anchoring strength Γ_{QR}, we introduce a surface energy density, again in the Rapini-Popoular form

$$f_s = \frac{\tilde{W}}{2}(\boldsymbol{Q} - \tilde{\boldsymbol{Q}})^2, \tag{4.38}$$

where $\tilde{W}$ is the anchoring strength and $\tilde{\boldsymbol{Q}}$ is the preferred order parameter on the surfaces. We augment the total free energy Equation 4.27 with the

surface anchoring energy

$$F_R = \int_\Omega f \, dV + \int_{\Gamma_{QR}} \frac{1-\phi}{2} f_s \, dS. \tag{4.39}$$

For simplicity, we assume that the relaxation of $\boldsymbol{Q}$ on Γ_{QR} is much faster than in the bulk. This allows us to decouple $\boldsymbol{Q}$ on the boundary and construct a BC, otherwise a dynamic equation has to be associated with Γ_{QR} and solved together with the existing equations. With a standard variational procedure, we get the natural BC of Robin type

$$\left(\tilde{W}\left(\boldsymbol{Q}-\tilde{\boldsymbol{Q}}\right)+K\hat{\boldsymbol{n}}\cdot(\nabla\boldsymbol{Q})\right)\Big|_{\Gamma_{QR}}=0. \tag{4.40}$$

(iv) Symmetry boundaries are common devices to reduce computational cost and enforce symmetry. On symmetry boundaries Γ_S, it is not sufficient to impose homogeneous Neumann BC for individual components of $\boldsymbol{Q}$. Here I present a geometrical argument. The proposed conditions are not necessarily new, yet to the author's knowledge, they are not commonly seen in recent LC-modeling literature that uses tensorial order parameters. The eigenvectors of the tensor $\boldsymbol{Q}$ give three symmetry planes of $\boldsymbol{Q}$. It implies that one of the eigenvectors must be along the normal direction of a symmetry boundary. In this thesis, I only consider symmetry boundaries that are parallel to coordinate planes in orthogonal curvilinear systems. Hence, the condition can be stated as (i) diagonal terms of $\boldsymbol{Q}$ have zero gradients across Γ_S; (ii) off-diagonal terms of $\boldsymbol{Q}$ vanish on Γ_S. That is the following mixed BC

$$\hat{\boldsymbol{n}}\cdot\nabla\left(Q_{ii}\right)|_{\Gamma_S}=0, \;\; Q_{ij}|_{\Gamma_S}=0 \; (i\neq j). \tag{4.41}$$

Here ii and ij are simple subscripts which don't follow Einstein summation.

Note that in the presence of a moving contact line where the free surface intersects Γ_{QN}, Γ_{QD}, Γ_{QR} or Γ_S, the BCs can still be imposed on the whole boundary. Since the equation of $\boldsymbol{Q}$ reduces to be trivial in the isotropic fluid, corresponding degenerate equations are removed from the linear system after spatial discretization in the computation. The nonphysical BCs in those regions do not play a role.

4.3.4 Modification of the LC stress tensor

The key issue here is how the anchoring condition modifies the stress in the interfacial region. Following the same approach used by de Gennes and Prost [38] and Yue et al. [181], we decompose this effect into two parts, each governed by a different virtual operation.

(i) From a virtual rotation and deformation of the molecular distribution without motion of the fluid. This is already accounted for in the new $\boldsymbol{H}$ tensor (Equation 4.33).

(ii) From a virtual motion of the fluid with the $\boldsymbol{Q}$ configuration frozen in each fluid particle. This variational procedure will give rise to an additional stress tensor associated with $\nabla\phi$, caused by the newly proposed anchoring energy. Following a similar naming convention in the LE theory [38], we call this stress the anchoring Ericksen stress $\boldsymbol{\tau}_{ae}$. Next I derive this term, following the same procedure as in [181].

We consider how a general Ericksen stress is derived in the phase-field formulation, and later narrow down to the effect of the anchoring energy f_a. Introduce a virtual displacement $\delta\boldsymbol{u}$ of the flow field[1]. Note that the operator δ here is following material points, so it is not the ordinary variation.

$$\delta(\cdot) = \delta_o(\cdot) + \delta\boldsymbol{u} \cdot \nabla(\cdot), \tag{4.42}$$

where the operator δ_o is the ordinary variation of a field in the Eulerian frame. According to the *Virtual Work Principle* [43, 181], the resulting variation in the total free energy F is related to the virtual strain by

$$\delta F = \int_\Omega \boldsymbol{\tau}_e : (\nabla\delta\boldsymbol{u})^\intercal \, dV, \tag{4.43}$$

[1]Here $\boldsymbol{u}$ is different from that in Section 3.2 where it indicates the orientation of a single nematic molecule.

where $\boldsymbol{\tau}_e$ is the Ericksen stress. The variations of $\nabla \boldsymbol{Q}$ and $\nabla \phi$ satisfy

$$\delta(\nabla \phi) = -\nabla(\delta \boldsymbol{u}) \cdot \nabla \phi, \tag{4.44}$$

$$\delta(\nabla \boldsymbol{Q}) = -\nabla(\delta \boldsymbol{u}) \cdot \nabla \boldsymbol{Q}. \tag{4.45}$$

which will be derived at the end of this section. It follows that

$$\begin{aligned} \frac{\partial f}{\partial(\nabla \phi)} \cdot \delta(\nabla \phi) &= -\frac{\partial f}{\partial(\nabla \phi)} \cdot (\nabla(\delta \boldsymbol{u}) \cdot \nabla \phi) \\ &= -\frac{\partial f}{\partial(\partial_i \phi)} \partial_i(\delta u_j) \partial_j \phi \\ &= \left(-\frac{\partial f}{\partial(\partial_i \phi)} (\partial_j \phi) \right) \partial_i(\delta u_j). \end{aligned} \tag{4.46}$$

Similarly,

$$\begin{aligned} \frac{\partial f}{\partial(\partial_i Q_{kl})} \delta(\partial_i Q_{kl}) &= -\frac{\partial f}{\partial(\partial_i Q_{kl})} \partial_i(\delta u_j)(\partial_j Q_{kl}) \\ &= \left(-\frac{\partial f}{\partial(\partial_i Q_{kl})} (\partial_j Q_{kl}) \right) \partial_i(\delta u_j). \end{aligned} \tag{4.47}$$

The variation of F becomes

$$\begin{aligned} \delta F &= \int_\Omega \delta f \, dV \\ &= \int_\Omega \left(\frac{\partial f}{\partial \phi} \delta \phi + \frac{\partial f}{\partial Q_{kl}} \delta Q_{kl} + \frac{\partial f}{\partial(\partial_i \phi)} \delta(\partial_i \phi) + \frac{\partial f}{\partial(\partial_i Q_{kl})} \delta(\partial_i Q_{kl}) \right) \, dV. \end{aligned} \tag{4.48}$$

For the first two terms in the integrand, because the variation is following material points and we have assumed a frozen $\boldsymbol{Q}$ field, $\delta \phi = 0, \delta \boldsymbol{Q} = 0$. For the last two terms, observe Equation 4.46 and Equation 4.47. Thus

$$\delta F = \int_\Omega \left(-\frac{\partial f}{\partial(\partial_i \phi)} (\partial_j \phi) - \frac{\partial f}{\partial(\partial_i Q_{kl})} (\partial_j Q_{kl}) \right) (\partial_i \delta u_j) \, dV. \tag{4.49}$$

Compared with Equation 4.43, we obtain

$$(\tau_e)_{ij} = -\frac{\partial f}{\partial(\partial_i\phi)}(\partial_j\phi) - \frac{\partial f}{\partial(\partial_i Q_{kl})}(\partial_j Q_{kl}). \tag{4.50}$$

We can recognize that the second term already exists in $\boldsymbol{\tau}_p$ (Equation 3.18), as expected. The addition of f_m and f_a in the total f does not contribute to this term. Through the first term, f_m results in a tensor $-\lambda\nabla\phi\nabla\phi$, which is the usual stress form of surface tension in the phase-field formalism. Note that similar to Yue et al. [181], for simplicity we omit the incompressibility constraint in this variational procedure. This constraint will contribute an isotropic stress equal to $f_m\boldsymbol{I}$, which will be absorbed into pressure. Therefore, nothing is lost here. This stress for surface tension can also be written in other forms [185]. Our key point is that, f_a contributes to a stress through the first term in Equation 4.50, which is the $\boldsymbol{\tau}_{ae}$ we are after.

Plugging Equation 4.24 and Equation 4.25 into Equation 4.50, we get, respectively

$$\begin{aligned}
\left(\tau_{ae}^{\perp}\right)_{ij} &= -\frac{\partial f_a^{\perp}}{\partial(\partial_i\phi)}(\partial_j\phi) \\
&= -W\left[|\nabla\phi|^2 Q_{kl} - q_e\left((\partial_k\phi)(\partial_l\phi) - \frac{1}{3}|\nabla\phi|^2\delta_{kl}\right)\right] \\
&\cdot\left[2Q_{kl}(\partial_i\phi) - q_e\left(\delta_{ik}(\partial_l\phi) + (\partial_k\phi)\delta_{li} - \frac{2}{3}(\partial_i\phi)\delta_{kl}\right)\right](\partial_j\phi), \quad (4.51) \\
\left(\tau_{ae}^{\parallel}\right)_{ij} &= -\frac{\partial f_a^{\parallel}}{\partial(\partial_i\phi)}(\partial_j\phi) \\
&= -W\left[|\nabla\phi|^2 Q_{kl} + q_e\left((\partial_k\phi)(\partial_l\phi) - \frac{1}{3}|\nabla\phi|^2 J_{kl}\right)\right] \\
&\cdot\left[2Q_{kl}(\partial_i\phi) + q_e\left(J_{ik}(\partial_l\phi) + (\partial_k\phi)J_{li} - \frac{2}{3}(\partial_i\phi)J_{kl}\right)\right](\partial_j\phi). \quad (4.52)
\end{aligned}$$

As expected, $\boldsymbol{\tau}_{ae}$ is not symmetric. We now update the total LC stress tensor in

Equation 3.18 as

$$
\begin{aligned}
(\tau_p)_{ij} = &- \frac{1-\phi}{2}\left[\xi H_{ik}\left(Q_{kj}+\frac{1}{3}\delta_{kj}\right)+\xi\left(Q_{ik}+\frac{1}{3}\delta_{ik}\right)H_{kj}\right. \\
&\left. -2\xi\left(Q_{ij}+\frac{1}{3}\delta_{ij}\right)(Q_{kl}H_{kl})+L_1\left(\partial_i Q_{kl}\right)\left(\partial_j Q_{kl}\right)\right] \\
&+ H_{ik}Q_{kj}-Q_{ik}H_{kj}+(\tau_{ae})_{ij},
\end{aligned} \tag{4.53}
$$

with the updated $\boldsymbol{H}$ in Equation 4.33.

Mathematically, Equation 4.53 does not need a BC, although we know that on Γ_S boundaries, $\boldsymbol{\tau}_p$ satisfies the same conditions as $\boldsymbol{Q}$.

$$
\hat{\boldsymbol{n}}\cdot\nabla\left((\tau_p)_{ii}\right)\big|_{\Gamma_S}=0,\ \ (\tau_p)_{ij}\Big|_{\Gamma_S}=0\ (i\neq j). \tag{4.54}
$$

From numerical calculation results, we find that using our finite element formulation (Section 4.3.7), it is necessary to impose Equation 4.54 in order to obtain physically correct results at Γ_S boundaries In any event, by imposing Equation 4.54 we can reduce the total number of unknowns.

Finally, we derive the identities Equation 4.44 and Equation 4.45. The same formulae have been given in [181] without detailed derivation. Therefore I simply aim to provide a footnote here for completeness. Consider $\delta(\nabla\phi)$ first. After the virtual displacement, ϕ becomes a new function (scalar field). Call it $\tilde{\phi}$. We know that $\tilde{\phi}(\boldsymbol{x})=\phi(\boldsymbol{x}-\delta\boldsymbol{u})$. In accordance with our material variation

$$
\delta(\nabla\phi)=\frac{\partial\tilde{\phi}}{\partial x_i}(\boldsymbol{x}+\delta\boldsymbol{u})-\frac{\partial\phi}{\partial x_i}(\boldsymbol{x}). \tag{4.55}
$$

Introduce a transform of coordinates

$$
\boldsymbol{X}=\boldsymbol{x}-\delta\boldsymbol{u}. \tag{4.56}
$$

We have

$$
\tilde{\phi}(\boldsymbol{x})=\phi(\boldsymbol{X}). \tag{4.57}
$$

Therefore

$$\begin{aligned}
\delta(\nabla\phi) &= \frac{\partial\tilde{\phi}}{\partial x_i}(\boldsymbol{x}+\delta\boldsymbol{u}) - \frac{\partial\phi}{\partial x_i}(\boldsymbol{x}) \\
&= \left(\frac{\partial\tilde{\phi}}{\partial X_j}\frac{\partial X_j}{\partial x_i}\right)\Bigg|_{\boldsymbol{x}+\delta\boldsymbol{u}} - \left.\frac{\partial\phi}{\partial x_i}\right|_{\boldsymbol{x}} \\
&= \left[\frac{\partial\tilde{\phi}}{\partial X_j}\left(\delta_{ij} - \frac{\partial\delta u_j}{\partial x_i}\right)\right]\Bigg|_{\boldsymbol{x}+\delta\boldsymbol{u}} - \left.\frac{\partial\phi}{\partial x_i}\right|_{\boldsymbol{x}} \\
&= \left[\frac{\partial\phi}{\partial x_j}\left(\delta_{ij} - \frac{\partial\delta u_j}{\partial x_i}\right)\right]\Bigg|_{\boldsymbol{x}+\delta\boldsymbol{u}} - \left.\frac{\partial\phi}{\partial x_i}\right|_{\boldsymbol{x}} \\
&= \left.\frac{\partial\phi}{\partial x_i}\right|_{\boldsymbol{x}+\delta\boldsymbol{u}} - \left(\frac{\partial\phi}{\partial x_j}\frac{\partial\delta u_j}{\partial x_i}\right)\Bigg|_{\boldsymbol{x}+\delta\boldsymbol{u}} - \left.\frac{\partial\phi}{\partial x_i}\right|_{\boldsymbol{x}}.
\end{aligned} \tag{4.58}$$

Since $\delta\boldsymbol{u}$ is infinitesimal, take the limit $\delta\boldsymbol{u} \to 0$. Then we get Equation 4.44. As for $\delta(\nabla\boldsymbol{Q})$, once we write it as $\delta(\partial_i Q_{jk})$ in a Cartesian coordinate system, the same procedure as above leads to Equation 4.45.

4.3.5 The Navier-Stokes equation and the Cahn-Hilliard equation

The classical continuity equation and Navier-Stokes equation for an incompressible fluid govern the velocity and pressure fields:

$$\begin{aligned}
\nabla\cdot\boldsymbol{v} &= 0, \\
\rho\frac{\partial\boldsymbol{v}}{\partial t} + \rho\boldsymbol{v}\cdot\nabla\boldsymbol{v} &= \rho\boldsymbol{g} - \nabla p + \nabla\cdot(2\eta\boldsymbol{D}) + \nabla\cdot\boldsymbol{\tau}_p + \mu\nabla\phi.
\end{aligned} \tag{4.59}$$

Here as standard treatment, ρ and η are the interpolated density and dynamic viscosity of the two-fluid mixture

$$\rho = \frac{1-\phi}{2}\rho_n + \frac{1+\phi}{2}\rho_i,\ \eta = \frac{1-\phi}{2}\eta_n + \frac{1+\phi}{2}\eta_i, \tag{4.60}$$

where the subscripts n and i refer to the nematic and isotropic fluids, respectively. $\boldsymbol{g}$ is the vector of gravitational acceleration. The last term is a body-force form of surface tension from the phase-field formulation [185]. The chemical potential μ follows Equation 4.5.

On the boundaries, standard BCs for $\boldsymbol{v}$ and p apply, which are omitted here. I will specify these BCs for various applications considered in Chapter 6.

The Cahn-Hilliard (CH) equation is the same as Equation 4.4, repeated here.

$$\frac{\partial \phi}{\partial t} + \boldsymbol{v} \cdot \nabla \phi = \gamma \nabla^2 \mu, \tag{4.61}$$

Again the chemical potential μ is

$$\mu = \frac{\delta \int_\Omega f_m \, dV}{\delta \phi} = \lambda \left(-\nabla^2 \phi + \frac{\phi(\phi^2 - 1)}{\epsilon^2} \right). \tag{4.62}$$

As introduced in Section 4.1, we restrict the flow-related time scales to be intermediate such that the local interfacial ϕ profile has been stabilized, while undesirable long-term Mullins-Sekerka flow is mitigated.

Note that in the CH equation, i.e., the evolution of ϕ is only governed by the minimization of the total mixing energy $\int f_m \, dV$, rather than the total free energy $\int f \, dV$. This is essential to recover both accurate surface tension and LC anchoring. If including f_b and f_a in the chemical potential, the equilibrium interfacial profile of ϕ_e is unlikely to satisfy Equation 4.6, thereby leaving the value of surface tension and anchoring strength untractable. Even the notion of a sharp-interface limit and the asymptotic results regarding the CH equation may not hold any more. On the contrary, our goal is to recover correct motion of the interface under macroscopic surface tension and nematic anchoring. As pointed out in Yue et al. [181], we are using the phase-field formalism as a *numerical device*. Therefore, we *should* keep the gradient dynamics in the CH equation restricted to minimizing the mixing energy. See also Section 4.1 for more details on the PF method.

The fourth-order CH equation requires two BCs. The following conditions are well established. One often requires that there is no diffusive flux across all boundaries

$$\hat{\boldsymbol{n}} \cdot \nabla \mu|_{\partial \Omega} = 0. \tag{4.63}$$

The other BC is usually one of the following three types. Except for the first BC, the other two specify a contact angle at the three-phase contact line where the fluid-

fluid interface intercepts a solid boundary.

(i) Specifying the phases on the boundary Γ_{PD}

$$\phi|_{\Gamma_{PD}} = \phi_D. \tag{4.64}$$

(ii) Specifying a static contact angle θ_c on the solid boundary Γ_{PN}

$$\hat{\boldsymbol{n}} \cdot \nabla\phi|_{\Gamma_{PN}} = |\nabla\phi| \cos\theta_c. \tag{4.65}$$

Notice that the case of $\theta_c = \pi/2$ reduces to the Neumann BC for ϕ, which can also be used for symmetry boundaries Γ_S.

(iii) Specifying a dynamic contact angle. This requires introduction of a wall energy and a nominal contact angle. The dynamic contact angle is governed by the competition between the wall energy and bulk free energy and fluid motion. The net effect is similar to a dynamic contact line with a slip length in a sharp-interface formalism. We omit details because they are not used in this thesis. Interested readers can consult e.g., Yue et al. [187].

4.3.6 Summary of the governing equations

The governing equations are summarized below.

$$
\begin{aligned}
&\nabla \cdot \boldsymbol{v} = 0, \\
&\rho \frac{\partial \boldsymbol{v}}{\partial t} + \rho \boldsymbol{v} \cdot \nabla \boldsymbol{v} = \rho \boldsymbol{g} - \nabla p + \nabla \cdot (2\eta \boldsymbol{D}) + \nabla \cdot \boldsymbol{\tau}_p + \mu \nabla \phi. \\
&\frac{\partial \phi}{\partial t} + \boldsymbol{v} \cdot \nabla \phi = \gamma \nabla^2 \mu, \\
&\mu = \frac{\delta \int_\Omega f_m \, dV}{\delta \phi} = \lambda \left(-\nabla^2 \phi + \frac{\phi(\phi^2 - 1)}{\epsilon^2} \right). \\
&\frac{\partial \boldsymbol{Q}}{\partial t} + \boldsymbol{v} \cdot \nabla \boldsymbol{Q} = \boldsymbol{S}(\nabla \boldsymbol{v}, \boldsymbol{Q}) + \Gamma \boldsymbol{H}(\boldsymbol{Q}, \nabla \boldsymbol{Q}) \\
&(\tau_p)_{ij} = -\frac{1-\phi}{2} \left[\xi H_{ik} \left(Q_{kj} + \frac{1}{3}\delta_{kj} \right) + \xi \left(Q_{ik} + \frac{1}{3}\delta_{ik} \right) H_{kj} \right. \\
&\left. -2\xi \left(Q_{ij} + \frac{1}{3}\delta_{ij} \right) (Q_{kl} H_{kl}) + L_1 \left(\partial_i Q_{kl} \right) \left(\partial_j Q_{kl} \right) \right] \\
&+ H_{ik} Q_{kj} - Q_{ik} H_{kj} + (\tau_{ae})_{ij}.
\end{aligned}
\tag{4.66}
$$

4.3.7 Finite element approximation

We use a Galerkin finite element method to numerically approximate the solution to Equation 4.66. It has been used in existing calculations by [188, 189] with the regularized LE theory, but not in recent PF simulations of [112, 113]. The present method allows for an unstructured mesh with a high degree of refinement in the interfacial region. The construction of the weak form below is similar to that in [185], with additional terms and treatment associated with the BE theory for LC hydrodynamics.

Recall the Lebesgue space of square-integrable functions

$$
L^2(\Omega) \coloneqq \left\{ h \mid \|h\|_{L^2} < \infty \right\}. \tag{4.67}
$$

If $\boldsymbol{h}$ is a general tensor-valued function, then we say that $\boldsymbol{h} \in L^2$ when each component of $\boldsymbol{h}$ is in L^2. For an integer $k \geq 1$, H^k is the Sobolev space

$$
H^k(\Omega) \coloneqq \left\{ h \mid \nabla^j h \in L^2(\Omega), \, \forall j = 0 \cdots k \right\}. \tag{4.68}
$$

In the standard Galerkin formulation, the high-order derivatives of ϕ in the CH equation and of $\boldsymbol{Q}$ in the NS equation through the stress tensor $\boldsymbol{\tau}_p$ require high regularity of the variables. In this case, $\phi, \boldsymbol{Q} \in H^2(\Omega)$. Discretization needs quintic Argyris elements or Hermite elements of at least third order [11, 96]. To avoid the associated high computational cost, we follow the approach in [97, 185] and use a mixed finite element method. We introduce two auxiliary variables in the weak form. For the CH equation, same as in Yue et al. [185], we introduce μ, and split the CH equation into two second-order equations. For the NS equation, we keep $\boldsymbol{\tau}_p$ so that the terms involving $\boldsymbol{Q}$ in all equations are of second order at most. The latter treatment is new in the current context.

For convenience in notation, we write $\boldsymbol{\tau}_p$ in the following form

$$\boldsymbol{\tau}_p = -\boldsymbol{T}^{(1)}(\boldsymbol{Q}, \nabla\boldsymbol{Q}) - \nabla \cdot \boldsymbol{T}^{(2)}(\boldsymbol{Q}, \nabla\boldsymbol{Q}), \tag{4.69}$$

where $\boldsymbol{T}^{(1)}$ and $\boldsymbol{T}^{(2)}$ are tensors of second and third ranks, respectively. They only contain derivatives of $\boldsymbol{Q}$ up to first order. $\boldsymbol{T}^{(1)}$ and $\boldsymbol{T}^{(2)}$ are, respectively,

$$\begin{aligned} T_{ij}^{(1)} =&(\xi_p - 1)(M_a)_{ik} \cdot Q_{kj} + (\xi_p + 1)Q_{ik} \cdot (M_a)_{kj} + \frac{2}{3}\xi_p (M_a)_{ij} \\ &- 2\xi_p \left(Q_{ij} + \frac{1}{3}\delta_{ij} \right) (Q_{kl}(M_a)_{kl}) + L_p(\partial_i Q_{kl})(\partial_j Q_{kl}) \\ &- L_p(\partial_m Q_{ik})\partial_m(\xi_p Q_{kj}) - L_p\partial_m(\xi_p Q_{ik})(\partial_m Q_{kj}) \qquad (4.70) \\ &- \frac{2}{3}L_p(\partial_m \xi_p)(\partial_m Q_{ij}) \\ &- 2L_p\partial_m \left(\xi_p \left(Q_{ij} + \frac{1}{3}\delta_{ij} Q_{kl} \right) \right) (\partial_m Q_{kl}) \\ &- \tau_{ae}, \qquad (4.71) \end{aligned}$$

$$\begin{aligned} T_{mij}^{(2)} =&L_p(\xi_p - 1)(\partial_m Q_{ik})Q_{kj} + L_p(\xi_p + 1)Q_{ik}(\partial_m Q_{kj}) \\ &+ \frac{2}{3}\xi_p L_p(\partial_m Q_{ij}) - 2\xi_p L_p \left(Q_{ij} + \frac{1}{3}\delta_{ij} \right) Q_{kl}(\partial_m Q_{kl}), \qquad (4.72) \end{aligned}$$

where $\xi_p,\ L_p,\ \boldsymbol{M}_a$ are interpolated material properties and augmented $\boldsymbol{M}$

$$\xi_p = \frac{1-\phi}{2}\xi,\ L_p = \frac{1-\phi}{2}L_1,\ \boldsymbol{M}_a = \frac{1-\phi}{2}\boldsymbol{M}(\boldsymbol{Q}) - W\boldsymbol{G}(\boldsymbol{Q}, \nabla\phi). \quad (4.73)$$

Notice that on Γ_{QN} boundaries, because $\hat{\boldsymbol{n}} \cdot \nabla\boldsymbol{Q} = 0, \boldsymbol{T}^{(2)}$ vanishes

$$\hat{\boldsymbol{n}} \cdot \boldsymbol{T}^{(2)}\Big|_{\Gamma_{QN}} = 0. \quad (4.74)$$

Equation 4.66 is cast in the following weak form: Find $(\boldsymbol{v},\ p,\ \phi,\ \mu,\ \boldsymbol{Q},\ \boldsymbol{\tau}_p) \in H^1 \times L^2 \times H^1 \times H^1 \times H^1 \times H^1$ such that $\forall(\hat{\boldsymbol{v}},\ \hat{p},\ \hat{\phi},\ \hat{\mu},\ \hat{\boldsymbol{Q}},\ \hat{\boldsymbol{\tau}}) \in H^1 \times L^2 \times H^1 \times H^1 \times H^1 \times H^1$,

$$\begin{aligned}
&\int_\Omega \left(\rho\left(\frac{\partial \boldsymbol{v}}{\partial t} + \boldsymbol{v}\cdot\nabla\boldsymbol{v} - \boldsymbol{g}\right) - \mu\nabla\phi - \nabla\cdot\boldsymbol{\tau}_p\right)\cdot\hat{\boldsymbol{v}} + (-p\boldsymbol{I} + 2\eta\boldsymbol{D}) : (\nabla\hat{\boldsymbol{v}})^\intercal\, dV \\
&+ \int_\Omega (\nabla\cdot\boldsymbol{v})\hat{p}\, dV \\
&+ \int_\Omega \left(\frac{\partial\phi}{\partial t} + \boldsymbol{v}\cdot\nabla\phi\right)\hat{\phi} + \gamma\nabla\mu\cdot\nabla\hat{\phi}\, dV, \\
&+ \int_\Omega \left(\mu - \frac{\lambda}{\epsilon^2}\phi(\phi^2-1)\right)\hat{\mu} - \lambda\nabla\phi\cdot\nabla\hat{\mu}\, dV \\
&+ \int_{\Gamma_{PN}} \lambda|\nabla\phi|\hat{\mu}\cos\theta_c\, dS \\
&+ \int_\Omega \left(\frac{\partial\boldsymbol{Q}}{\partial t} + \boldsymbol{v}\cdot\nabla\boldsymbol{Q} - \boldsymbol{S} - \Gamma\boldsymbol{M}_a\right) : \hat{\boldsymbol{Q}}^\intercal + \Gamma K_p(\partial_k Q_{ij})(\partial_k\hat{Q}_{ij})\, dV \\
&+ \int_{\Gamma_{QR}} \frac{1-\phi}{2}\Gamma\tilde{W}\left(\boldsymbol{Q} - \tilde{\boldsymbol{Q}}\right) : \hat{\boldsymbol{Q}}^\intercal\, dS \\
&+ \int_\Omega \left(\boldsymbol{\tau}_p + \boldsymbol{T}^{(1)}\right) : \hat{\boldsymbol{\tau}}^\intercal - T^{(2)}_{kij}(\partial_k\hat{\tau}_{ij})\, dV \\
&+ \int_{\Gamma_{QD}\cup\Gamma_{QR}} \hat{\boldsymbol{n}}\cdot\boldsymbol{T}^{(2)} : \hat{\boldsymbol{\tau}}^\intercal\, dS = 0.
\end{aligned} \quad (4.75)$$

There is a practical consideration related to the PF method. When computing multiphase flows in a finite domain, due to relaxation of the total mixing energy, after the interfacial profile is stabilized ϕ will not be exactly 1 or -1 in the bulk of the two fluids. This phenomenon has been well documented [186]. In the current

multiphase flow involving a nematic phase, an outcome is that anti-diffusion of $\boldsymbol{Q}$ may arise in certain cases. This stems from the term $\nabla \cdot \left(\frac{1-\phi}{2} L_1 \nabla \boldsymbol{Q}\right)$ (see Equation 4.33) when ϕ shifts slightly above 1. Spurious oscillations in the $\boldsymbol{Q}$ field start growing as the simulation goes on. To mitigate this issue, we follow the idea in [185] and introduce a thresholding scheme. Let $h_s(x)$ denote a smoothed Heaviside function such that $h_s = 0$ when $x \leq -d$, $h_s = 1$ when $x \geq d$, and h_s transitions from 0 to 1 within $[-d, d]$. d is small to make the transition zone thin. The thresholding operation is

(i) The advection term $\boldsymbol{v} \cdot \nabla \boldsymbol{Q}$ in Equation 3.11 is multiplied by $h(-\phi + \phi_c)$.

(ii) The concentration factor $(1 - \phi)/2$ involved in the $\boldsymbol{Q}$ equation and $\boldsymbol{\tau}_p$ is multiplied by $h(-\phi + \phi_c)$. This includes Equation 4.27, Equation 4.33, Equation 4.34, Equation 4.53, Equation 4.73.

These steps are to enforce that the dynamics of $\boldsymbol{Q}$ and the LC stress $\boldsymbol{\tau}_p$ vanishes in regions where $\phi > \phi_c$. We choose the cutoff $\phi_c = 0.9$ and $d = 0.05$ to ensure that undesirable dynamics does not arise in the isotropic phase while maintaining LC dynamics in the majority of the mixing zone in the interfacial area. In fact, provided that we are close to the sharp-interface limit, what specific value the cutoff takes has little impact. We have tested even smaller ϕ_c values and the overall dynamics is hardly changed.

The model is implemented using the software package COMSOL Multiphysics® [1]. This is to utilize a selection of well-developed time-marching algorithms and numerical solvers. Equation 4.75 is discretized on an unstructured mesh of triangles, using piecewise quadratic Lagrange elements (P2) for $\boldsymbol{v}$, ϕ, μ, $\boldsymbol{Q}$, $\boldsymbol{\tau}_p$, and piecewise linear Lagrange elements (P1) for p. The unstructured mesh is essential. We need a high mesh density in the interfacial region to resolve the ϕ profile with a small ϵ, while in bulk regions where flow is slow, only a coarse mesh is needed. Using a uniform mesh density throughout is not only unnecessary, but also prohibitive given our computational resources. An Arbitrary-Lagrangian-Eulerian (ALE) scheme or an Adaptive Mesh Refinement (AMR) scheme can be coupled with our method to dynamically change mesh densities during the computation.

For time-stepping, we use a Backward-Difference-Formula (BDF) scheme with adaptive time step sizes and adaptive orders of accuracy between first and second

[25]. The adaptive time step size is crucial to resolve efficiently a range of time scales over which physical phenomena happen. All equations are coupled together and solved simultaneously. In each time step, the nonlinear system is solved by a Newton's method with possible damping. To solve each Newton iteration, we choose the MUltifrontal Massively Parallel sparse direct Solver (MUMPS) [3, 8]. MUMPS is an efficient direct linear solver with excellent scalability. In this thesis, since we only deal with 2D problems, a direct solver is advantageous in its robustness and accuracy, while the computational cost is reasonable.

Chapter 5

Problem I: The interaction of a pair of ferrofluid drops in a rotating magnetic field

In this chapter, we set up the ferrofluid drop interaction problem and apply the VOF formalism in Section 4.2 to solve this problem.

5.1 Problem setup

After extensive numerical experimentation, we have realized that a full 3D simulation of two ferrofluid drops in a rotating magnetic field is computationally prohibitive using our current tools. Thus, we will carry out a two-dimensional (2D) simulation using the geometry of Figure 5.1. Two drops of initially circular shape are placed symmetrically in a square domain Ω, which is large enough that the magnetic field and the velocity field on the boundary $\partial\Omega$ are hardly disturbed by the drops. A uniform external field rotates counter-clockwise with a constant speed and the dimensionless driving frequency of Equation 4.14. Its orientation is given by the phase angle $\theta_h = 2\pi f t$ with respect to the x axis. Thus, on the outer boundary we impose $-H_n(t) = -\boldsymbol{n} \cdot (\cos\theta_h,\ \sin\theta_h)$ (Equation 4.19). In most of our simulations, the pair of drops start from a horizontal initial orientation.

The parameter values are listed in Table 5.1 along with the experimental values

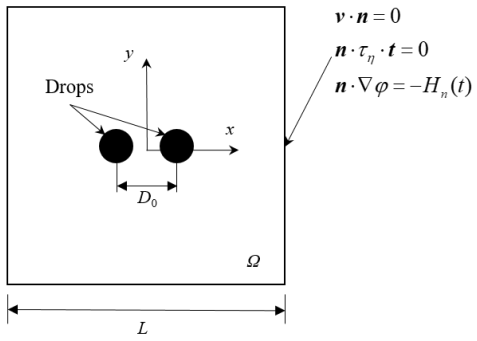

Figure 5.1: The 2D computational domain is a square with the ferrofluid drops initially placed symmetrically inside. On the outer boundary we specify a rotational magnetic field and no-penetration condition with free slip for the velocity.

in Chen et al. [32]. We use larger values for the magnetic Laplace number and the viscosity ratio, since the experimental values, corresponding to a low-viscosity ferrofluid and a high-viscosity surrounding liquid, tend to produce strong spurious currents across the interface, which only diminish slowly with mesh refinement. Despite these differences in parameters and the 2D geometry of the numerical simulations, we have been able to capture the key mechanisms governing the experiment.

The spurious currents associated with the experimental parameters have not been documented before. Normally, spurious currents are caused by imbalance between surface tension and pressure gradients, and decay with increasing viscosity by enhanced dissipation [131]. In our case, however, undulations in the velocity field decrease with decreasing viscosity (increasing La_m). We believe that the spurious currents at present are related to the numerical treatment of the magnetic force. A more detailed investigation is beyond the scope of this study. We use a larger viscosity ratio ξ to accelerate convergence of the calculation, thus reducing computational cost. Overall one can think of the surrounding medium in our computation as having lower viscosity than in the experiments.

We have used two validation tests to assess the performance of the code for simulating two-phase flows with magnetic effects. First, we compute the steady-state shape of a ferrofluid drop in a static uniform field. This test problem is set

Chen et al. [32]	Simulations
$\chi = 2.14$	$\chi = 2$
$f = 1/79$	$f = 1/120 - 1/40$
$Bo_m = 1.81$	$Bo_m = 0.2 - 2$
$La_m = 3.37$	$La_m = 50 - 75$
$\xi = 0.0249$	$\xi = 0.2 - 1$

Table 5.1: Comparison of parameters used in the experiment of Chen et al. [32] and in our simulations.

up in an axisymmetric domain, and we compute the equilibrium aspect ratio of the drop b/a as a function of Bo_m and χ. If the field is weak and the deformation is small, the drop shape can be assumed spheroidal and the problem admits an approximate analytical solution [7]. Figure 5.2 compares the numerical results with the analytical solution for two χ values. Excellent agreement is seen for relatively mild elongation of the drop. At higher Bo_m or χ values, the drop shape deviates from a perfect spheroid and the discrepancy between the numerical and theoretical results begins to increase.

Further we demonstrate convergence with respect to grid size and time step refinement and the domain size for the full numerical solution of our drop interaction problem as set up in Figure 5.1. The mesh generator requires specification of the coarsest and finest grid sizes, and we adaptively refine the mesh to deploy the finest grids at the interfaces [131]. For a simulation with a representative set of parameters ($f = 1/80$, $Bo_m = 2$, $\xi = 1$, $La_m = 75$ and initial separation $D_0 = 4$), Figure 5.3 illustrates mesh convergence using the horizontal velocity profile $u(x)$ at $t = 80$. The solution converges when the finest mesh size reaches 5×2^{-8} (Figure 5.3*a*) and the coarsest mesh size reaches 5×2^{-4} (Figure 5.3*b*). Such a grid is used for the rest of the paper except for Section 5.2.3, in which the finest mesh size is reduced to 5×2^{-9} to better resolve the fluid film between the drops. For time stepping, we have found the default adaptive scheme sufficient, with the maximum time step limited by the Courant-Friedrichs-Lewy condition associated with the advection of the fluid and the volume fraction field c [130, 131]. For the

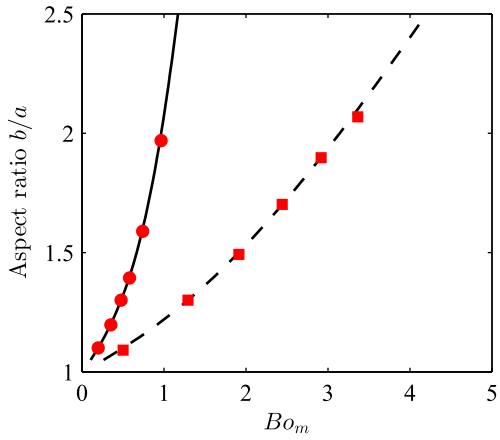

Figure 5.2: The steady-state drop aspect ratio b/a as a function of the magnetic Bond number Bo_m for two χ values. We compare the numerical results (symbols) with the small-deformation theory [7] for $\chi = 5$ (solid line) and $\chi = 2$ (dashed line). The axisymmetric domain is large enough that the magnetic field on the boundary is not disturbed by the drop. The finite-volume cells have sizes ranging from 5×2^{-9} to 5×2^{-6}, with finer cells concentrated on the drop interface.

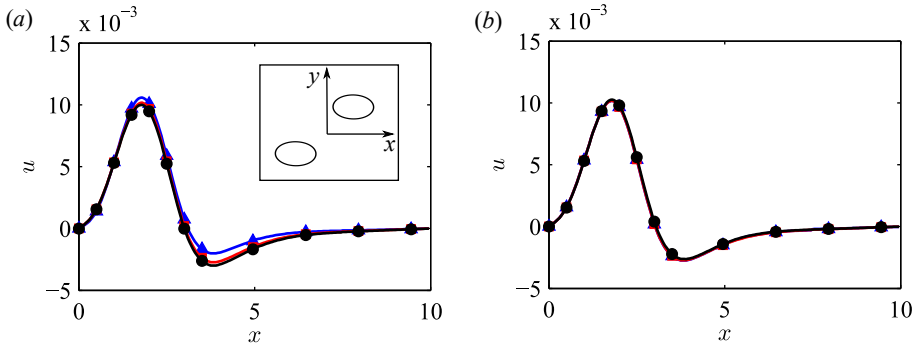

Figure 5.3: Convergence with mesh refinement ($f = 1/80$, $Bo_m = 2$, $\xi = 1$, $La_m = 75$, $D_0 = 4$). (*a*) $u(x)$ for different finest grid sizes: 5×2^{-7} (▲); 5×2^{-8} (■); 5×2^{-9} (●). The coarsest grid size is fixed at 5×2^{-4}. (*b*) $u(x)$ for different coarsest grid sizes: 5×2^{-3} (▲); 5×2^{-4} (■); 5×2^{-5} (●). The finest grid size is fixed at 5×2^{-8}. Temporal discretization is adaptive and the domain length is fixed at $L = 20$ to save computation time, and the profiles are taken at $t = 80$. The inset in (*a*) shows the shape and position of the drops at this moment.

domain size, $L = 40$ is large enough for the solution to be independent of L.

5.2 Results and discussion

5.2.1 Regimes of interaction

Four regimes of pairwise interaction between the drops have been identified, which can be observed by, for instance, varying the initial separation D_0 of the drops (Figure 5.4):

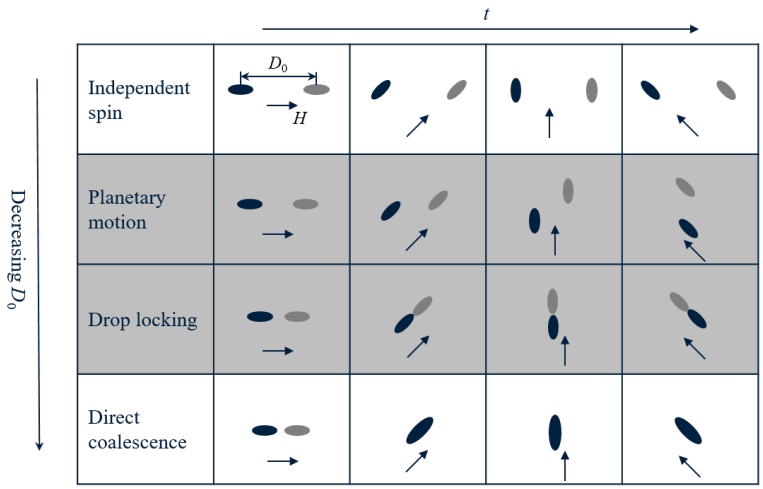

Figure 5.4: Regimes of interaction of the ferrofluid drop pair under a counter-clockwise rotating magnetic field.

- When D_0 is large, the drops spin individually in phase with the external magnetic field, with negligible interaction.
- At intermediate values of D_0, the drops perform planetary motion; they spin while revolving around each other. The angular velocity of the global revolution is lower than the rotating velocity of the field.
- At smaller values of D_0, the pair may attach to each other end-to-end without coalescing, and form a doublet that rotates with the driving frequency. In this "drop locking" regime, both the phase angle of individual drops and the

orientational angle of the pair are locked to the external field, while the drops maintain a small separation between them. This regime may be transient, sometimes preceded by an episode of planetary motion, and usually ending in coalescence.

- With an even smaller D_0, coalescence takes place right away without going through the locked rotation episode. Afterwards, the merged drop elongates and spins with the field.

These regimes agree qualitatively with recent experimental observations [104]. The rest of Section 5.2 focuses on the planetary motion and the drop-locking regimes, as well as transitions between different regimes.

5.2.2 Planetary motion

Figure 5.5 shows a typical simulation of the planetary motion. Each drop spins with the driving frequency of the rotating field f, with little phase lag. This is evident from Figure 5.5, where the long axes of the drops align to the field direction within 3°. In the mean time, the drops revolve around each other in the same sense as the rotating field, at a much lower rate. This is demonstrated in Figure 5.6(a) by the increase of the pair orientational angle $\theta_d(t)$ (see Figure 5.5 for definition). The revolution is not monotonic but suffers periodic small-scale reversals, a signature that agrees with experimental observations [32]. The drop separation $D(t)$, measured between the centroids of the drops (see Figure 5.5 for definition), shows a similar oscillation, around a mean value that appears to approach a limit in time. These features can be understood from the magnetic and hydrodynamic forces on the drops.

Magnetic interaction

The planetary motion resembles the behaviour of two solid magnetic microspheres in a rotating field, which has been accounted for by a dipole model [14, 67]. Thus, our first enquiry is which of the features observed above can be explained by the simple picture of magnetic dipole-dipole interactions in a viscous medium.

Assuming each drop is a magnetic point dipole, we can derive the following dimensionless 2D dipolar forces on each drop [71]:

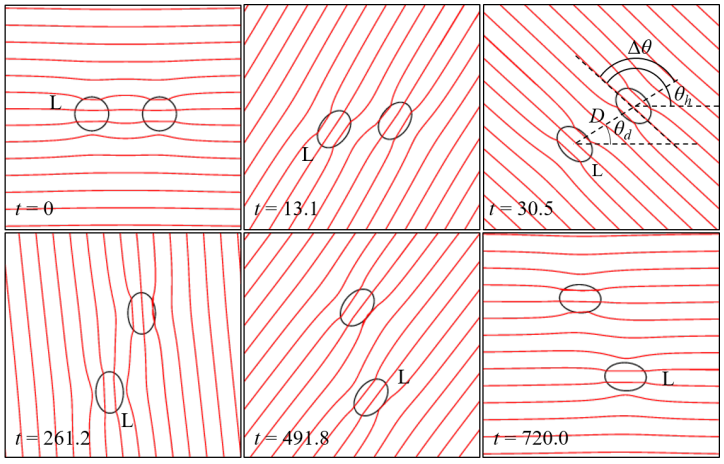

Figure 5.5: Snapshots of a typical simulation of planetary motion for parameters $f = 1/80$, $Bo_m = 2$, $\xi = 1$, $La_m = 75$ and $D_0 = 4$, showing the drops and the magnetic field lines. The letter L marks the drop initially on the left. We denote the distance between the centroids of the drops by D, and the orientational angle of the pair by θ_d.

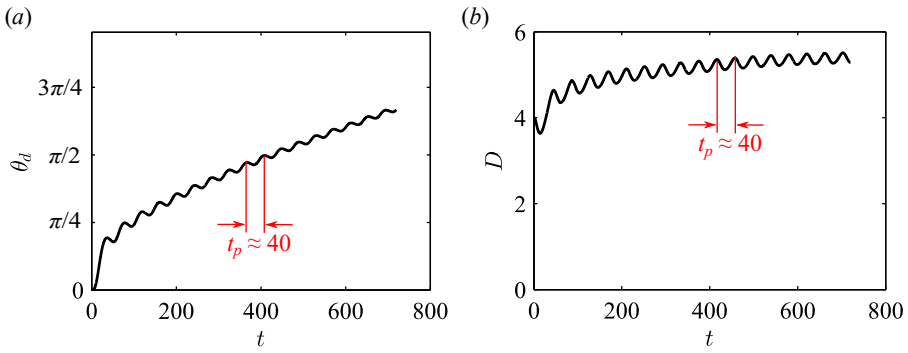

Figure 5.6: (a) The planetary revolution is manifested by the continual increase in the angle $\theta_d(t)$. (b) The distance $D(t)$ between the centroids of the drops. $f = 1/80$, $Bo_m = 2$, $\xi = 1$, $La_m = 75$, $D_0 = 4$. Note the oscillation in both curves with a period $t_p \approx 1/(2f) = 40$.

$$F_\theta = \left(\frac{\chi}{2+\chi}\right)^2 \frac{\sin(2\Delta\theta)}{D^3}, \quad F_r = -\left(\frac{\chi}{2+\chi}\right)^2 \frac{\cos(2\Delta\theta)}{D^3}, \qquad (5.1)$$

in the azimuthal and radial directions, respectively. The forces have been scaled by $4\pi\mu_0 H_0^2 r_0$. The former amounts to a magnetic torque that affects the rotation of the line of the centroids, i.e. the angle θ_d. A positive F_θ implies a counterclockwise rotation, in the same direction as the rotation of the magnetic field. The latter affects the separation D, and a negative F_r attracts the drops toward each other.

Because the speed of field rotation ($d\theta_h/dt$) is faster than the rate of planetary revolution ($d\theta_d/dt$) (Figure 5.6*a*), the phase lag $\Delta\theta = \theta_h - \theta_d$ increases in time. In each round of $\Delta\theta$, F_θ changes sign at $\Delta\theta = 0$, $\pi/2$, π and $3\pi/2$. Thus, there are four intervals in which the magnetic torque alternately rotates the pair forward (in the same direction as the rotating field) or backward (counter to the field). This explains the small-amplitude oscillations of θ_d in Figure 5.6(a). The oscillations in D is similarly due to the change in sign of F_r, although at different $\Delta\theta$ values. Because $d\theta_h/dt$ is much larger than $d\theta_d/dt$, $\Delta\theta$ increases at almost the same rate as θ_h. Hence, the appearance of $2\Delta\theta$ in Equation 5.1 means that θ_d and D oscillate with a frequency roughly twice the driving frequency f (see the period t_p in Figure 5.6).

Furthermore, in an interval of $\Delta\theta$ corresponding to a positive F_θ and forward rotation of θ_d, the line of centroids chases the driving field so as to slow down the increase of the phase lag $\Delta\theta$ and prolong the time period of forward rotation. Conversely, the time period of backward rotation is shortened. This difference in duration is manifested in Figure 5.6(a). Accumulated over repeated cycles, it produces a forward planetary revolution, in the same sense as the rotating field.

Similar arguments to the above have been made in Chen et al. [32]. In the next two sections, we examine the hydrodynamic interaction between the drops and interpret novel features in the planetary motion, which is original contribution from this thesis.

Hydrodynamic interaction

Our ferrofluid drops are not point dipoles, however. For one, they have a finite size and shape, and deform under the influence of the external field $\boldsymbol{H}$. Their motion

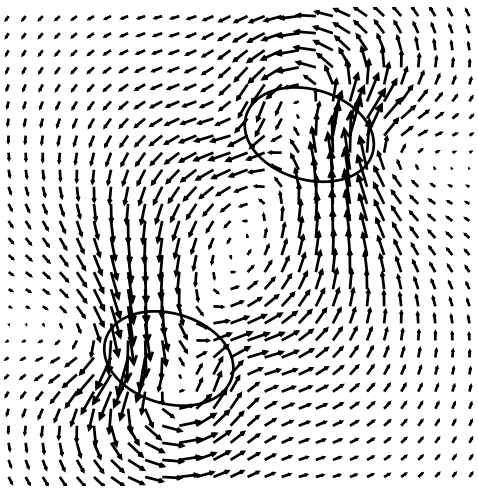

Figure 5.7: Instantaneous velocity field ($f = 1/80$, $Bo_m = 2$, $\xi = 1$, $La_m = 75$, $D_0 = 4$ at $t = 156.8$). Only the central region of the domain containing the drops is shown.

incurs viscous drag in the surrounding medium. As one elongated drop spins with the driving frequency f, it creates a flow field that sweeps the other drop forward and induces revolution around each other (Figure 5.7). This "viscous sweeping" effect provides another potential mechanism for the planetary motion, and is key to understanding several novel features of the planetary motion of ferrofluid drops that are absent for point dipoles or solid particles.

To evaluate the magnitude of the viscous sweeping effect, we vary the drop deformation by reducing the magnetic Bond number Bo_m from 2 to 0.2. This can be interpreted as increasing the interfacial tension by ten times. In Figure 5.8(*a*), the ovals represent the typical drop shape at each of the Bond numbers, at the driving frequency $f = 1/40$. The drop deformation is indeed greatly reduced, and so will be the viscous sweeping. This change in shape may potentially change the magnetization of the drops and the strength of magnetic interaction. However, Figure 5.8(*a*) shows little change in the mean value of D and its amplitude of the oscillations. Because the radial oscillation is driven by magnetic attraction or repulsion, it follows that there is little change in the magnitude of magnetic forces. Meanwhile, in Figure 5.8(*b*), the rate of global revolution has decreased

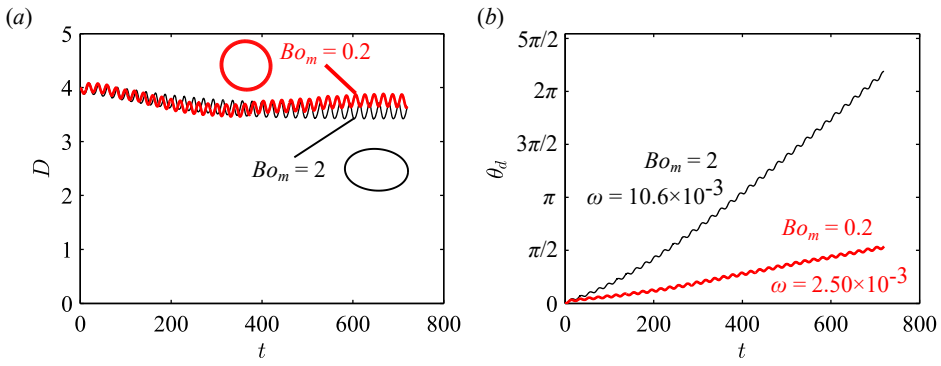

Figure 5.8: Effect of viscous sweeping probed by varying the magnetic Bond numbers Bo_m and drop shape: $Bo_m = 2$ (thin line) and $Bo_m = 0.2$ (thick line), with $f = 1/40$, $\xi = 1$, $La_m = 75$, $D_0 = 4$. (*a*) Evolution of the radial distance D. The ovals represent the typical drop shapes for the two Bond numbers. (*b*) Evolution of the pair angle θ_d. The angular velocity $\omega = d\theta_d/dt$ is calculated from the slope of straight lines fitted to the latter part of the $\theta_d(t)$ curves.

from $\omega = 10.6 \times 10^{-3}$ at $Bo_m = 2$ to $\omega = 2.50 \times 10^{-3}$ at $Bo_m = 0.2$. Hence, reducing viscous sweeping while keeping the magnetic effect roughly fixed has approximately quartered the rate of planetary revolution. Simulations at other f values have confirmed the same trend.

Taking the simplistic view that the dipolar magnetic interaction and viscous sweeping contribute additive parts to the planetary motion, we deduce from the above result that viscous sweeping is a more important mechanism than the magnetophoretic interaction. The same conclusion probably holds in the experiment of Chen et al. [32], whose external fluid has higher viscosity than in our numerical study, and thus is more efficient at viscous sweeping. As a side remark, the slower revolution for $Bo_m = 0.2$ means that $\Delta\theta = \theta_h - \theta_d$ increases slightly faster in time (Figure 5.8*b*). This explains the slightly shorter period of oscillation for the rounder drops that is evident in Figure 5.8(*a*). Its oscillation starts out in phase with that of the elongated drop, but has gained a lead of more than half a period by the end of the simulation.

Another novel feature, distinct from its counterpart in solid particles, is how the angular velocity ω of the planetary motion changes with the driving frequency

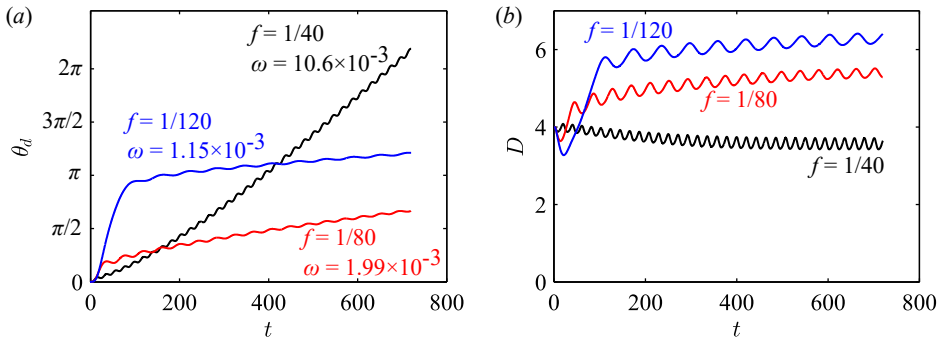

Figure 5.9: Effect of the driving frequency f on the planetary motion. (a) The evolution of θ_d at three frequencies $f = 1/120$, $1/80$ and $1/40$. The average angular velocity ω is calculated from the slope of straight lines fitted to the latter part of the curves. (b) The evolution of drop separation D under the same conditions. The other parameters are fixed: $Bo_m = 2$, $\xi = 1$, $La_m = 75$, $D_0 = 4$.

f.

With all other parameters fixed, increasing f causes the pair to revolve around each other at faster ω (Figure 5.9a). This contrasts the dipole-based solution for solid particles [14, 67], in which ω decreases with increasing f. The latter is because at a faster driving frequency f, the planetary revolution of the pair becomes less significant in determining the phase lag $\Delta\theta = \theta_h - \theta_d$. As a result, the difference in durations of forward and backward rotation due to θ_d also diminishes as the two become closer to cancelling each other. As a cumulative effect, the global revolution ω due to dipolar interaction decreases with increasing f. The distinction between ferrofluid drops and solid particles can be rationalized by viscous sweeping, which increases with the spinning velocity f of each drop so much that it compensates for any loss in the contribution due to magnetic dipolar interaction to the planetary motion. Note that the drop separation tends to different limits at different frequencies, being closer for higher frequencies (Figure 5.9b). The reduced separation may also have helped enhance the viscous sweeping.

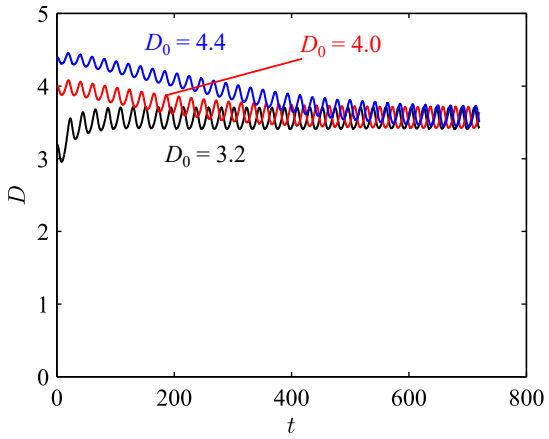

Figure 5.10: Evolution of the radial distance between the drops starting from different initial separations. $f = 1/40,\ Bo_m = 2,\ \xi = 1,\ La_m = 75$.

Limit separation

We turn to the last novel feature of the ferrodrop planetary motion: the drop separation D approaching a limiting mean value independent of the initial separation D_0. This has been noted in passing when discussing Figure 5.6 and Figure 5.9. Figure 5.10 depicts three trajectories that start from different D_0 toward the same long-time limit mean separation, denoted by D_s. Initially, the oscillation in the radial distance has smaller amplitudes for the drops starting farther away. This is due to weaker magnetic force at larger distance. As the drops approach the same D_s, the amplitudes for different cases converge to the same value.

The limit separation cannot be explained by dipole-dipole interactions. In previous studies of 3D spheres, the attractive radial magnetic force has greater magnitude and longer duration than the repulsive. Hence, the particles gradually attract and move into contact despite the periodical repulsions [67]. In 2D, the radial magnetic force $F_r \propto \cos(2\Delta\theta)$ (Equation 5.1) is symmetric between the attractive and repulsive phases. Thus, the two cancel over each cycle and do not produce a cumulative drift in D. Two solid particles would thus revolve in orbits that retain the initial mean separation D_0.

Here we examine three *hydrodynamic* mechanisms that have potentially contributed to the limit separation. The first is inertia. As the magnetic radial force

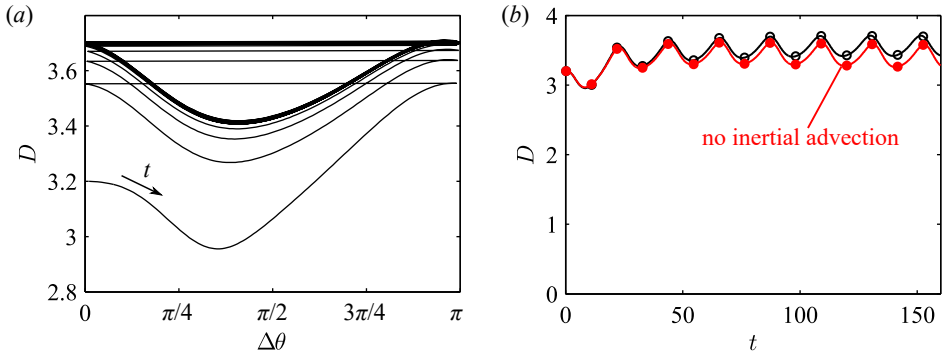

Figure 5.11: The inertial effect. $D_0 = 3.2$, $f = 1/40$, $Bo_m = 2$, $\xi = 1$, $La_m = 75$. (a) Trajectory of the pair of drops in the D-$\Delta\theta$ phase plane. The t-arrow indicates the progression of time. As $\Delta\theta$ reaches π, we fold the trajectory to the left end ($\Delta\theta = 0$) because of the $\cos(2\Delta\theta)$ periodicity of the radial dipolar force F_r. (b) Evolution of radial distance D between the drops with (open ○) or without (filled ●) the nonlinear convection term.

F_r drives the drops apart or toward each other, the drops will not stop instantaneously when F_r switches between positive and negative values. Rather, inertia carries them further, overshooting the zeros of F_r. Figure 5.11(a) illustrates the overshoot in the D-$\Delta\theta$ phase plane by a representative trajectory, the $D_0 = 3.2$ case in Figure 5.10. F_r changes from attraction to repulsion at $\Delta\theta = \pi/4$. But D continues to shrink and reaches its minimum some time after F_r has turned repulsive. At such a small D, F_r achieves a larger repulsive value than if the overshoot were absent, and drives the drops apart more forcefully. Similarly the maximum of D overshoots $\Delta\theta = 3\pi/4$, such that part of the attractive phase happens at larger separations. This results in a weaker attractive F_r that fails to bring the drops back to the separation at the start of the previous cycle. Over each cycle, therefore, the inertial overshoot favors the repulsive force over the attractive one, and amounts to a net effect of separating the drops. As a test of the inertial effect, we turn off the nonlinear convection term in the Navier-Stokes equation, and repeat the simulation of Figure 5.11(a). Figure 5.11(b) shows that without the convective part of inertia, the separation D does not increase as much from one cycle to the next and approaches a smaller D_s. This provides a partial confirmation of the inertial effect.

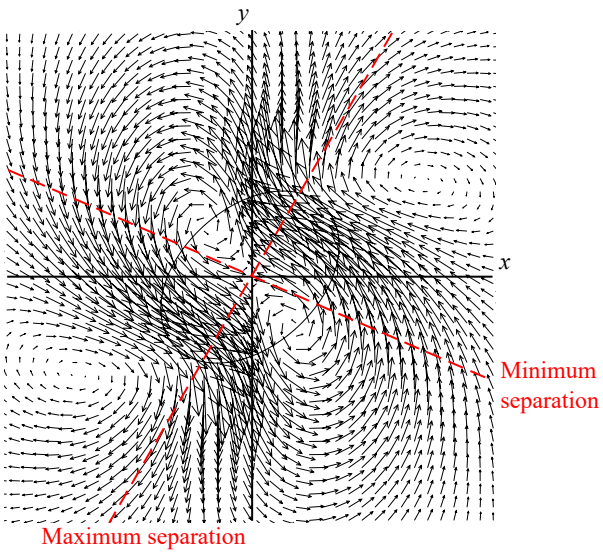

Figure 5.12: The velocity field around a single ferrofluid drop spinning steadily in a rotating field. $f = 1/80$, $Bo_m = 2$, $\xi = 1$ and $La_m = 75$. The dashed lines indicate locations where a second drop will be at maximum or minimum separation from the one shown during planetary motion.

The second is the viscous sweeping effect, which favors drop attraction. Figure 5.12 shows the velocity field around a single ferrofluid drop spinning in a rotating field. We examine how a second drop, placed in different positions relative to the first, would be pushed or pulled by the radial component of the flow field. We prefer this simpler flow to the two-drop velocity field of Figure 5.7, as the latter varies according to the location and orientation of the drops, and the added complexity obscures the underlying physics. Here the flow is steady as far as the rotating drop is concerned. For ease of discussion, we orient the x and y axes always at $\pi/4$ from the long axis of the drop. Thus, the flow field stays the same at different times, and the second drop will be placed at different angular locations at different times during its revolution.

We start by noting that the radial dipolar force vanishes if the second drop is placed on the x or y axes ($\Delta\theta = \pi/4$ or $3\pi/4$, see Equation 5.1). Next, to follow the increase of the phase lag $\Delta\theta$ during planetary motion, we imagine the second

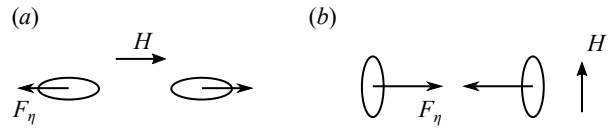

Figure 5.13: Illustration of anisotropic viscous drag. Magnetic attraction in (*a*) induces a smaller viscous drag F_η than the magnetic repulsion in (*b*).

drop moving clockwise around the first, starting from the first quadrant. As the second drop passes from above the x axis to below it, $\Delta\theta$ increases past $\pi/4$. F_r changes from attractive to repulsive, suggesting a minimum in separation D. Because of inertia, however, the minimum is attained further clockwise at an angle of about 0.13π below the x axis. Similarly the farthest separation is at about 0.17π past the y axis. The flow is mostly radially inward in the region around the minimum D but outward in the region around the maximum D. As a result, the second drop experiences stronger inward flow than outward flow during its revolution. Although the overall radial flux around a drop necessarily vanishes, viscous sweeping favors approach over separation on balance. Figure 5.9(*b*) provides direct evidence for this argument. Raising the driving frequency f increases the spinning velocity of the drops and the strength of viscous sweeping, which results in closer separation between the drops.

Finally, the third effect is anisotropic viscous drag, illustrated by the diagrams in Figure 5.13. The radial magnetic force is attractive when the phase lag $\Delta\theta$ has a small magnitude (below $\pi/4$). As the drops approach, therefore, they present relatively small cross-sections to each other and thus have smaller viscous drag F_η (Figure 5.13*a*). Conversely, the separation phase sees the drops oriented away from their line of centroids, and the large cross-sectional area induces more viscous drag (Figure 5.13*b*). Overall the anisotropic viscous drag favors drop attraction.

With the three effects in simultaneous action, we can rationalize the attainment of the limit separation D_s. When the drops are initially far apart, the inertial overshoot effect is weak, and the anisotropic drag and viscous sweeping effect bring the drops closer together. If the initial separation D_0 is small, the inertial overshoot is amplified as the asymmetry between approach and separation becomes relatively larger. This mechanism prevails over viscous sweeping and anisotropic drag to

push the two drops apart. The limit separation will be achieved when all effects are in balance.

Admittedly, the arguments above are mostly qualitative since it is difficult to quantify each factor and analyze their variation with parameters such as f. For instance, when we reduce the magnetic Bond number Bo_m in Figure 5.8, the rounded shape of the drop reduces viscous sweeping and anisotropic drag, and hence should increase the limit separation D_s. In the meantime, numerical results show that the inertial overshoot is also suppressed for the round drop, probably by the reduction in flow velocity. The outcome is that D_s only increases slightly. We can rationalize the outcome thus, but cannot make the quantitative calculation to predict it.

5.2.3 Drop locking

Figure 5.14 shows a typical simulation in the drop locking regime, first discovered by our calculation. Compared with the planetary motion of Figure 5.5, the viscosity ratio and the initial separation D_0 are both smaller. The drops initially approach each other as if coalescing, and form a thin liquid film between them. Then the two rotate as one at the same angular velocity as the external field. The locked rotation lasts for about $1/2$ of a cycle before coalescence.

Informed by our study, our collaborators went back to the laboratory to search for the drop locking regime experimentally [104]. Indeed, starting with the conditions that would produce the planetary motion and gradually reducing the initial drop separation, we were able to confirm the drop locking regime experimentally. Figure 5.15 shows snapshots of a pair of drops locked in close proximity and rotating with the driving frequency. In this case, the drops are locked for about 5/4 cycles of rotation before coalescing, a longer duration than in our numerical solution. This duration varies among experimental runs, apparently stochastically. In one extreme case, the drops remain locked for the entire duration of the experiment, for more than 12 cycles. In a sense, we can view drop locking as intermediate between planetary motion and direct coalescence. The transition among the regimes will be analyzed in the next subsection.

The reason that drop locking lasts much shorter time in the simulations than in the experiment is likely two-fold. First, we have used a lower viscosity for

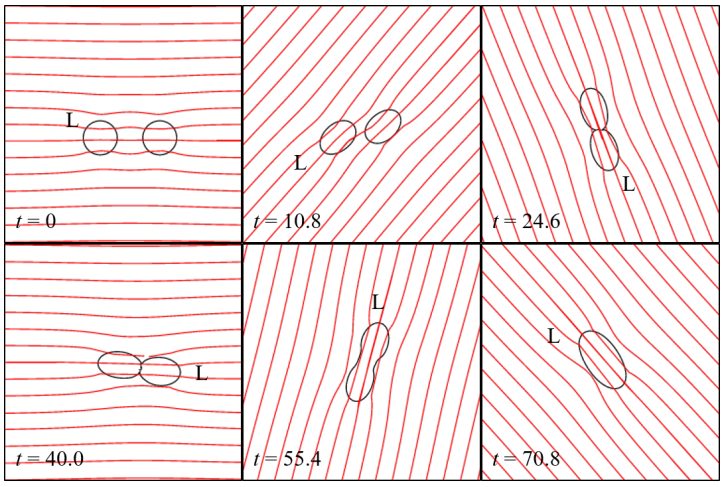

Figure 5.14: A typical simulation in the drop locking regime, with snapshots showing the drops and magnetic field lines. $f = 1/80$, $Bo_m = 2$, $\xi = 0.2$, $La_m = 75$ and $D_0 = 3.5$. The letter L marks the drop (or the end of the combined drop) initially on the left.

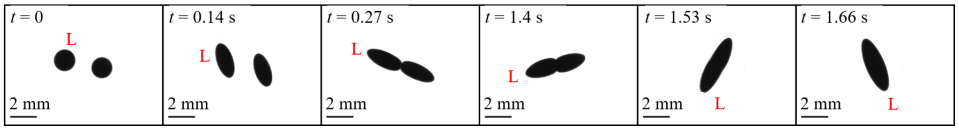

Figure 5.15: Snapshots of drop locking observed in an experiment. The letter L marks the drop (or the end of the combined drop) initially on the left.

the surrounding medium in the simulations (see Table 5.1), and this will produce faster film drainage. Second, insufficient numerical resolution of the thin liquid film between the drops may also lead to premature coalescence. As drop coalescence occurs upon rupturing of the thin liquid film separating them, its exact timing depends on molecular-scale forces and cannot be predicted by purely continuum models [182]. In simulations, therefore, rupture or coalescence is often precipitated by incidental factors such as numerical errors.

5.2.4 Transitions between regimes

The last section suggests that drop locking is an intermediate regime between planetary motion and direct coalescence. Naturally the question arises as to what con-

ditions determine the transition between regimes. In Section 5.2.1, we have found it convenient to describe the 4 regimes in terms of gradually reducing the initial separation D_0. This is not the only way to organize the regimes. Now we will consider the transitions as the outcome of the various forces in competition.

Generally, the interaction of a pair of ferrofluid drops in a rotating field is determined by the competition between the magnetic forces and viscous drag. The former causes attraction and even coalescence, while the latter, by way of modifying the relative position and orientation of the drops, introduces the potential for repulsion and sustained cyclic motion without coalescence. Much insight can be gained from considering the simpler case of solid microspheres (or effectively magnetic dipoles) that has been studied before [14, 67].

In this case, Helgesen et al. [67] derived a critical driving frequency based on dipole interactions in 3D and the Stokes drag. Using our unit system and scaling (see Section 2.2), this critical frequency can be written in dimensionless form as

$$f_c = \frac{2\sqrt{La_m}}{\pi}\left(\frac{\chi}{3+\chi}\right)^2 \frac{1}{D^5}. \tag{5.2}$$

At a driving frequency $f < f_c$, the magnetic force dominates the viscous drag. The pair rotates at the same speed as the driving field, with a phase lag $\Delta\theta$ never exceeding $\pi/4$. Thus the magnetic radial force remains attractive at all times and the spheres approach each other and then stay in contact. This behaviour is the counterpart of our drop locking regime. When $f > f_c$, the strong viscous drag causes the phase lag $\Delta\theta$ to exceed $\pi/4$. The two spheres periodically repel and separate, and revolve around each other at a lower rate, as in our planetary motion. Bacri et al. [14], Helgesen et al. [67] have also verified the predictions by experiments.

Extending this idea to the ferrofluid drops in our case, we can view the transitions outlined in Figure 5.4 in a more general light. Increasing the initial separation D_0 tends to decrease the magnetic forces relative to the viscous drag, resulting in the shift from direct coalescence to drop locking, and further to planetary motion and independent spin. The same outcome can also be achieved by one or a combination of the following means: gradually increasing the driving frequency f, reducing the magnetic susceptibility χ or reducing the magnetic Laplace number La_m. In fact, as La_m decreases from 75 to 50 in the simulation of Figure 5.14,

drop locking gives way to planetary motion. Furthermore, taking the experimental parameters of Chen et al. [32], Equation 5.2 predicts the dimensional critical driving frequency to be 0.5 Hz. This is consistent with observations of the planetary motion at a driving frequency of 1 Hz in the experiment.

To make direct comparison with our 2D numerical simulation, we assume Oseen flow with small inertia to avoid the singularity of Stokes flow. Balancing the dipole force in the azimuthal direction with the Oseen drag on a cylinder [82], we can derive a 2D counterpart of Equation 5.2:

$$\frac{f_c}{\ln\left(\frac{3.7}{\pi D\sqrt{La_m}f_c}\right)} = \frac{\sqrt{La_m}}{\pi}\left(\frac{\chi}{2+\chi}\right)^2\frac{1}{D^4}, \tag{5.3}$$

In our numerical simulations, planetary motion prevails at a frequency of $f = 0.025$ at $D_0 = 3.5$, $La_m = 75$, $\chi = 2$ and $\xi = 0.2$. Drop locking is realized at the lower frequency of $f = 0.0125$. Thus, the threshold frequency lies between these two values. Using the same parameters, Equation 5.3 predicts a critical frequency of $f_c = 0.0075$, smaller but on the same order of magnitude as the threshold frequency in the simulations.

Of course, our ferrofluid drops are not point dipoles, and their deformation and hydrodynamic interaction introduce new mechanisms into the picture. For one, we have observed that near the boundary between regimes, the initial positioning of the drops relative to the field can influence which behaviour prevails. In all the simulations presented so far, the drops are initially aligned along the field direction (horizontal in Figure 5.1). Thus, the two drops initially attract and approach each other. If the two drops are placed in a vertical line, perpendicular to the initial field direction, they repel each other at the start. For a relatively close $D_0 = 3.6$ (the other parameters being $f = 1/120$, $Bo_m = 2$, $\xi = 1$, $La_m = 75$), we have observed the two drops coalescing directly from the horizontal initial configuration, but separating and settling into a planetary motion from the vertical initial configuration. In addition, the viscosity ratio ξ of the ferrofluid to the surrounding medium affects the regimes. In the drop-locking example of Section 5.2.3, increasing ξ from 0.2 to 1 while keeping all other parameters the same will cause a transition from drop locking to planetary motion. Increasing the viscosity of the ferrofluid drop

makes it more rounded, and the reduced viscous sweeping tends to keep the drops farther apart. These are manifestations of the ferrofluid drop dynamics as distinct from that of magnetic dipoles.

A still more important factor is viscous sweeping, which can affect the drop interaction significantly. On the one hand, it directly promotes the revolution of the drops around each other through viscous forces. On the other, it tends to push the drops toward each other, magnifying the magnetic forces in the mean time. Thus, it is difficult to express its effects, say, as an algebraic generalization of Equation 5.3. Given the computational cost, especially associated with resolving thin films, we have not undertaken a comprehensive parameter sweep to determine more precisely the boundaries among the regimes as part of this study.

5.3 Summary for Problem I

Inspired by the experimental observations of Chen et al. [32], we have used direct numerical simulation for the first time to investigate the interaction between a pair of ferrofluid drops suspended in an immiscible fluid inside a rotating uniform magnetic field. The driving field is of sufficiently low frequency that the drops elongate and spin in phase with the field. We have observed four regimes of pair-wise interaction within the range of parameters explored: independent spin, planetary motion, drop locking, and direct coalescence. These are in qualitative agreement with experimental observations.

Furthermore, we have probed the mechanisms behind these outcomes by interrogating our numerical results. The transition between these regimes can be understood as the outcome of the competition of two types of forces: magnetophoretic forces that tend to attract the drops toward each other, and viscous drag that hinders the drop motion and causes the drops to fall periodically into a configuration of mutual repulsion. Thus, relatively strong magnetic forces favor coalescence, while relatively strong viscous drag favors less interactive regimes. The drop locking regime was discovered in the simulations first, and then confirmed by new laboratory experiments. It represents an intermediate state between direct coalescence and planetary motion.

We have analyzed the planetary motion in detail. A model of magnetic dipolar

interaction explains well the oscillations in the trajectory of the drops. Although the magnetic interaction can also produce revolution of the two drops around each other, we have found a type of hydrodynamic interaction—viscous sweeping—to play a more important role. When an elongated drop spins with the driving field, it produces a flow field that sweeps the second drop in the same direction. As a result, drop interaction presents novel features that cannot be explained by dipolar interaction. For example, the average angular velocity of the planetary revolution increases with the driving frequency, contrary to predictions of the dipole model. Besides, the drops in planetary motion approach a mean separation in time that is independent of initial separations. This limit separation is smaller if the external field rotates faster.

We should note that the simulations are limited by computational cost to two dimensions, so quantitative comparison with experiments is difficult. The main numerical challenge comes from resolving the thin film between two drops. Thanks to the efficient adaptive mesh refinement, we have been able to use mesh sizes as small as 5×2^{-9} times the initial drop radius near the interface. The solution for the magnetic field and the need for a large enough domain to avoid boundary interference also add to the magnitude of a full 3D simulation. The main contribution of this study, therefore, consists in elucidating qualitatively the mechanisms underlying the experimental observations of ferrofluid drops in a rotating magnetic field. In this regard, the 2D predictions match well with the experimental observations, including the transition between regimes (Section 5.2.1 and Section 5.2.4) and the emergence of drop locking (Section 5.2.3). This indicates that the 2D simulations have captured the essential physics. Beyond the pairwise interaction studied here, the experiments have also demonstrated self organization of a cluster of drops into regular patterns [32]. This, together with a full 3D numerical calculation using more realistic material parameters, presents challenges for future theoretical and computational studies.

Chapter 6

Problem II: Elasto-capillary flows of liquid crystals

In this chapter, we validate our PF method for computing interfacial flows of LCs with numerical examples, and apply the method to solve the problem of drop retraction involving a nematic phase.

6.1 Validations

In this section, I present various examples of single-phase LC flow. The purpose is two-fold.

(i) Validate our model by reproducing known results quantitatively.

(ii) Provide ground for our interpretation of more complicated behaviour in multiphase flows.

They are summarized below

(i) Formation of defects near a spherical particle. We consider two different defect structures: the Saturn ring and polar ring.

(ii) Flow-aligning LC in simple shear flow. We consider the cases both without and with anchoring on bounding walls.

(iii) Annihilation of defects of opposite winding numbers. We simulate this process with and without "back-flow", to be explained below.

Because all these pertain to single-phase LC bulk flow, we turn off the second phase as well as the interface treatment in our model and code. Note that the physics in the following examples is well-known, and modeling and computation have been carried out by other researchers.

6.1.1 Formation of defects near a spherical particle

Suppose a spherical solid particle is submerged in the bulk of a nematic, with strong homeotropic anchoring on the particle surface and uniform alignment in the far field. Consider the relaxation of the $\boldsymbol{Q}$ field and the nucleation of a defect near the particle. Experimentally we typically see one of two possible stationary configurations: Saturn ring (with quadrupolar symmetry) and a hyperbolic hedgehog (with dipolar symmetry). In general, as the particle radius increases, the energetically favoured defect configuration transitions from a Saturn ring to a hyperbolic hedgehog [52]. In a certain parameter range, though, meta-stable configurations co-exist due to the complicated energy landscape, which is both shown by experiments [63] and predicted by computations [140]. Note that different theories of nematic dynamics predict slightly different defects. True point hedgehogs are predicted with a kinetic theory [52, 54], while phenomenological theories using the LdG energy expansion with single-elastic-constant approximation (see Section 3.2) always indicates that the point defect will open up to be a small ring [58, 140]. So far, experiments have not validated one of these predictions against the other, as current techniques do not have the resolution to probe the fine structures in defect cores.

Here I calculate the formation of a Saturn ring and a polar ring, and demonstrate meta-stability with different defects by starting from different initial guesses. Results are compared with those in Ravnik and Žumer [140], where the total elastic energy is minimized by solving its Euler-Lagrange equation with a numerical annealing procedure. The solid particles are embedded using an immersed-boundary-like scheme. We solve our BE dynamics using our own numerical technique, and recover quantitatively the same steady state as the same elastic energy functional

(LdG energy) is minimized.

We set up the problem in 2D axisymmetric geometry, exploiting rotational symmetry. The computational domain is shown in Figure 6.1 in cylindrical coordinates. As we are only interested in the steady-state defect configurations, flow

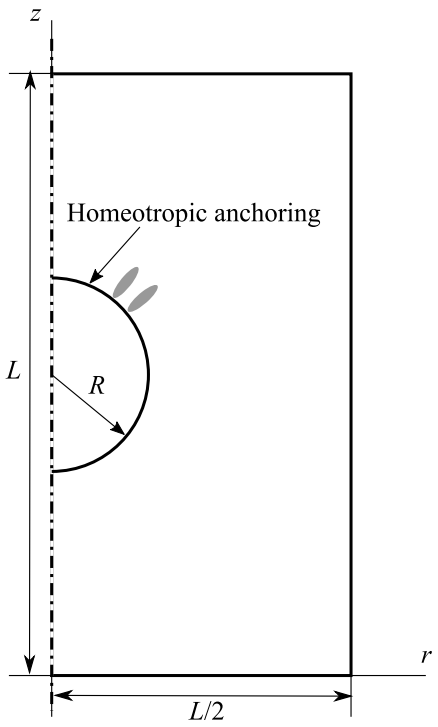

Figure 6.1: Computational domain and BCs for defect formation near a spherical particle with homeotropic anchoring.

is irrelevant here. Hence, we only solve the evolution equation of $\boldsymbol{Q}$ in the bulk of LC (Equation 3.11). Following [140], we impose homeotropic anchoring of finite strength on the particle surface (Equation 4.40), though the anchoring is rather strong (see specific parameters below). The outer bounding walls mimic infinity, so the BC in Equation 4.36 is used. On the symmetry axis $r = 0$, Equation 4.41 is used. For convenience of comparing with [140], we use a dimensional parameter system. The parameters are set as: $A = -0.172 \times 10^6$ Pa, $B = -2.12 \times 10^6$ Pa, $C = 1.73 \times 10^6$ Pa, $K = 4 \times 10^{-11}$ N, $W_s = 1 \times 10^{-2}$ N/m, $R = 0.5$ μm, $L = 2$ μm. These give the equilibrium scalar order parameter as $q_e = 0.799$ through

Equation 3.8. Since there is no flow, ξ is irrelevant. Γ controls the time scale of distortion relaxation and can thus be arbitrary, so we set it to be 1 $\text{Pa}^{-1}\text{s}^{-1}$. We have confirmed convergence of our results by refining the mesh, and also ensured steady state and domain-size independence.

Saturn ring

To recover the quadrupolar configuration, we prescribe an initial $\boldsymbol{Q}$ field with the directors aligned in the z-direction and $\boldsymbol{Q}$ being in equilibrium state (Equation 3.2 and Equation 3.8). To resolve the defect core with sufficient mesh density, we specify a fine mesh of approximately uniform sizes in a circular region near expected defect location, with progressively coarse mesh farther away from the defect. The mesh used in our study is shown in Figure 6.2. We have also indicated the scalar order parameter q at steady state through the grey scale. The brighter the colour is, the better LC molecules are aligned. A defect core is clearly shown in the onset which is sufficiently resolved by the mesh.

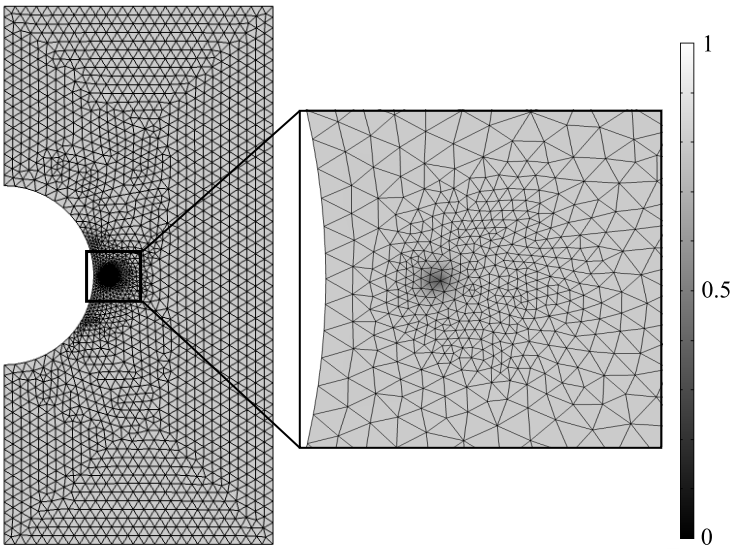

Figure 6.2: Mesh for computation of the Saturn ring near a spherical particle with homeotropic anchoring. The Saturn ring defect is also visualized through the scalar order parameter q indicated by the grey scale.

The calculated molecular configuration is visualized in Figure 6.3. Figure 6.3(a) displays an overview of the Saturn ring, with the iso-surface of $q = 0.5$ shown in the green contour, representing the defect core. Figure 6.3(b) shows the defect structure with a magnified view onto a dissected plane going through the particle centre and perpendicular to the ring. We visualize the molecular distribution by drawing ellipsoids representing the positive-definite tensor $\boldsymbol{Q} + \boldsymbol{I}/3$. Their colour shows the magnitude of the maximum eigenvalue. The more elongated the ellipsoid is, the better molecules are aligned along its major axis. In the defect core region, the ellipsoids become much more rounded due to reduced molecular order.

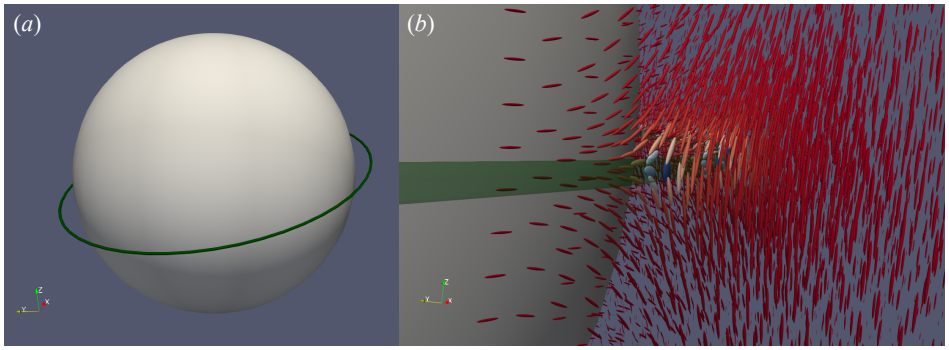

Figure 6.3: The Saturn ring defect. (a) Overview of the Saturn ring near the particle. The green contour shows the iso-surface for the scalar order parameter $q = 0.5$. (b) The molecular distribution near the defect core. The ellipsoids represent the tensor $\boldsymbol{Q} + \boldsymbol{I}/3$ and their colour signifies the maximum eigenvalue. The more elongated an ellipsoid is, the better local molecules align.

We compare our results with those from [140]. In Figure 6.4 we show the calculated $\boldsymbol{Q}$ components along the line $z = L/2$ in the r-z plane, near the defect core. They are compared with data extracted from Ravnik and Žumer [140] ("RZ"). The location of the defect core and change in $\boldsymbol{Q}$ profiles match very well, except that [140] has a more diffuse defect core. Considering the difference in computational method, grid structure and resolution, particularly the approximate surface representation in [140] we conclude that the agreement is satisfactory.

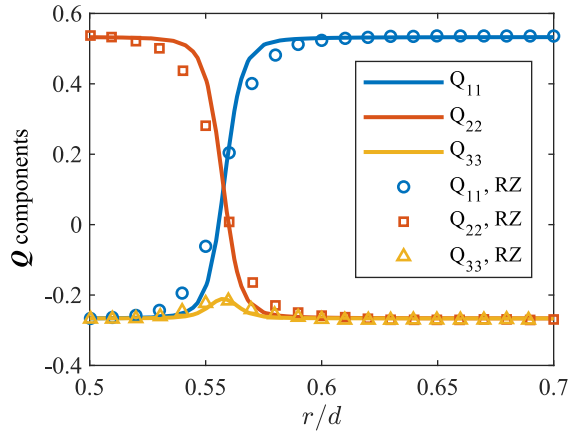

Figure 6.4: Calculated $\boldsymbol{Q}$ components of the Saturn ring defect compared to those from [140] ("RZ").

Polar ring

For the dipolar configuration, we use the *Ansatz* postulated by Lubensky et al. [105] as the initial condition. The *Ansatz* describes approximately the director field around a hyperbolic hedgehog defect generated by a solid spherical particle. Similar to the Saturn ring case, we use a non-uniform unstructured mesh which is shown in Figure 6.5 together with the polar ring indicated by the colour map.

As expected [58, 140], the point defect opens spontaneously to reduce the total energy. Figure 6.6 visualizes the steady-state polar ring from our calculation. In Figure 6.6(a), the defect core is represented by the iso-surface contour of $q = 0.5$. In Figure 6.6(b) we visualize $\boldsymbol{Q} + \boldsymbol{I}/3$ near the polar ring, this time on two dissecting planes through the particle centre and perpendicular to the ring.

We quantitatively examine the location and size of the polar ring to compare with [140]. In our simulation, the centre of the polar ring is 1.26 μm from the particle centre, which agrees well with the distance of 1.23 μm from [140]. We determine the radius of the polar ring, defined to be the distance between the polar ring centre and the geometric centre of the torus formed by the iso-surface $q = 0.5$, to be 0.057 μm. This is smaller than 0.067 μm found by [140]. Again considering the different numerical setup and ambiguity of grid resolution in [140], we believe satisfactory agreement has been reached.

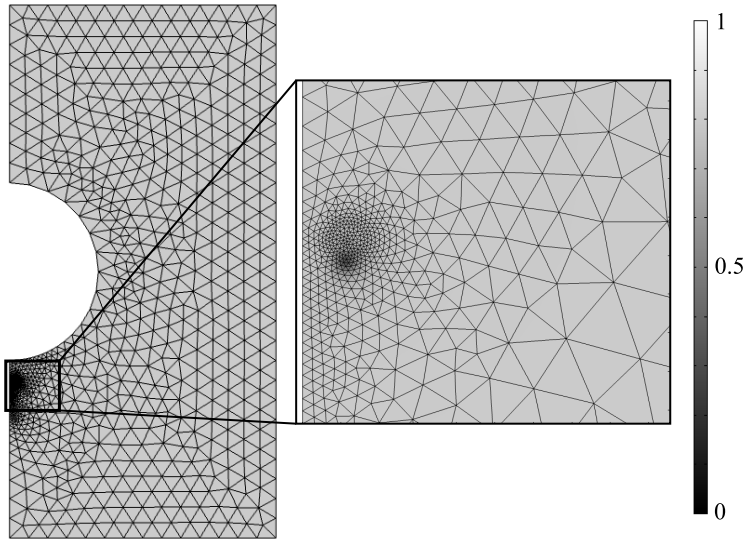

Figure 6.5: Mesh for computation of the polar ring defect, which is visualized through the inset. The grey scale indicates the scalar order parameter q.

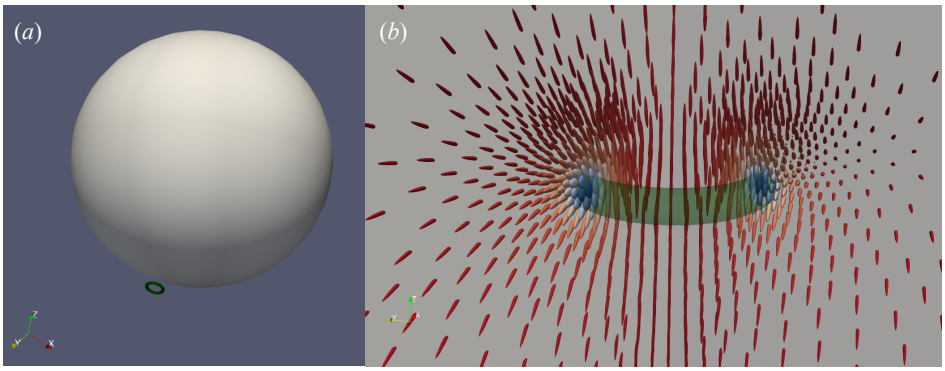

Figure 6.6: The polar ring defect. (a) Overview of the polar ring. The green contour shows the iso-surface for the scalar order parameter $q = 0.5$. (b) The molecular distribution ($\boldsymbol{Q} + \boldsymbol{I}/3$) near the defect core.

6.1.2 Flow-aligning LC in simple shear flow

In the two examples of this section, we validate the coupling of the LC order with flow. In both cases, we consider a square computational domain in 2D planar geometry (Figure 6.7). In the x-direction, periodic BC applies. In the y-direction, the

domain is bounded by two solid walls in relative motion, creating a shear (Couette) flow. Different BCs for $\boldsymbol{Q}$ on the bounding walls lead to the following two scenarios. (i) Without anchoring on the walls, the flow field and molecular configuration are homogeneous in the domain. (ii) With anchoring on the walls, distortion in the $\boldsymbol{Q}$ field arises as the flow alignment competes with wall anchoring. The flow field and $\boldsymbol{Q}$ configuration become inhomogeneous in the y-direction.

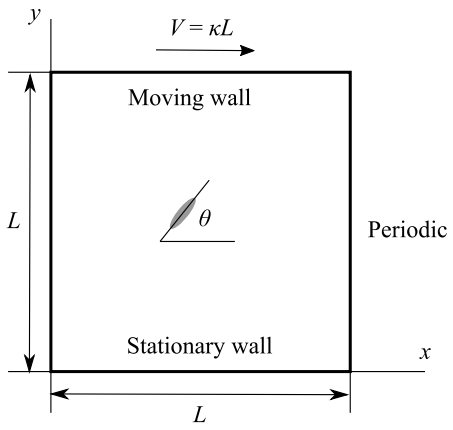

Figure 6.7: Computational domain for LC in a simple shear flow.

Homogeneous flow

In the first example, we consider a homogeneous LC configuration in essentially an infinite domain of simple shear flow. Thanks to vanished spatial gradients of $\boldsymbol{Q}$, the LC stress tensor is divergence-free, and thus does not alter the flow field. Therefore, in the calculation, we might as well decouple the flow from the $\boldsymbol{Q}$ evolution equation by removing the LC stress tensor. On the two walls, no-slip BC is imposed for the velocity field so that a simple shear flow with constant strain rate κ develops after starting the simulation, unaffected by the LC alignment. No flux BC (Equation 4.36) is used for the $\boldsymbol{Q}$ components to preserve spatial homogeneity. We choose our material parameters and operating conditions such that the nematic is in a uniaxial state under the *flow-aligning* regime [38]. In this case, the director is well defined, and it is stationary at an angle θ ($\theta \in [0, \pi)$) from the flow direction (Figure 6.7).

We use the parameters for a typical nematic LC such as 5CB, similar to those from Hung et al. [70]. To better map their parameters, introduce the nematic interaction strength U [40, 43, 54], and a molecular elasticity energy density $\tilde{A}$. Let

$$A = \tilde{A}\left(1 - \frac{U}{3}\right),\ B = -\tilde{A}U,\ C = \tilde{A}U. \tag{6.1}$$

It follows that dimensionless numbers govern the nematic order are: $U,\ \xi$ and the Deborah number

$$De = \frac{\kappa}{\Gamma\tilde{A}}, \tag{6.2}$$

which denotes the ratio between LC molecular relaxation time and characteristic flow time. In order to compare with theory, we choose $De = 0.001$ so that molecular equilibrium is maintained and LC alignment is uniaxial. From Equation 3.8 one sees that U determines the equilibrium scalar order parameter q_e. Figure 6.8(a) shows that the calculated q using Equation 3.5 from simulations under different U values (markers) are indeed in good agreement with the equilibrium values from Equation 3.8 (solid line). In this case, one could derive a relationship [40]

$$\xi\cos(2\theta) = \frac{3q}{q+2}. \tag{6.3}$$

Figure 6.8(b) shows that our numerical results (markers) match the analytical prediction (solid line) in a large range of q values.

Inhomogeneous flow with anchoring on the walls

In the second example, we take one step further and consider two-way coupling between the nematic order and the flow. We impose homeotropic anchoring with infinite strength on the bounding walls at equilibrium order q_e (see Equation 4.37). At steady state, long-range distortions in the $\boldsymbol{Q}$ field exists as the LC molecules transition from the flow-aligned direction near the centre of the domain to being approximately perpendicular to the flow direction at the walls. This spatial gradient exerts an LC stress on the fluid flow. The velocity profile across the channel in the y-direction is distorted and deviates from the linear profile in the last example. Thus the strain rate κ is just nominal, used merely as a parameter to represent the

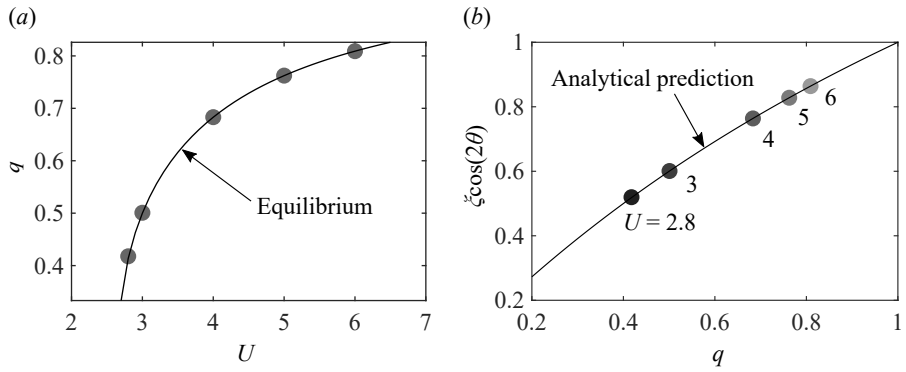

Figure 6.8: Flow aligning of nematic in a simple shear flow. $De = 0.001$ (a) Calculated q values from simulations using Equation 3.5 (symbols) match equilibrium scalar order parameter computed from Equation 3.8 (solid line). (b) Calculated director angles θ from simulations (markers) match analytical prediction in Equation 6.3 (solid line).

sliding velocity of the top wall (Figure 6.7).

We set $U = 6$, $\xi = 1$. Since we do not insist on local equilibrium and uniaxial alignment, we employ higher values of De between 10 and 160. The other dimensionless groups governing the LC dynamics are:

(i) An Ericksen number

$$Er = \frac{\eta \kappa L^2}{L_1}, \tag{6.4}$$

which represents the viscous force compared to elastic force in the flow. It is in the range of 10 and 160. Note that this definition is adapted to our BE-theory-based formulation, and is slightly different from the conventional Ericksen number in the context of LE theory [38].

(ii) A Péclet number

$$Pe = \frac{\kappa L^2}{\Gamma L_1}, \tag{6.5}$$

which is the ratio between the rate of advection of $\boldsymbol{Q}$ by the flow to the rate of diffusion of $\boldsymbol{Q}$ by distortional elastic relaxation. Pe is also taken to be between 10 and 160.

(iii) The Reynolds number

$$Re = \frac{\rho \kappa L^2}{\eta}, \tag{6.6}$$

which is kept small (< 0.4).

The values for these dimensionless numbers are chosen such that there are significant distortions between the centre and boundaries of the domain, which is suitable for testing our computation.

The numerical results for the case $De = 40,\ Er = 40,\ Pe = 40,\ Re = 0.1$ are shown in Figure 6.9. Note that in this plot, the horizontal axis is y. Figure 6.9(a) visualizes the normalized dominating eigenvector of computed $\boldsymbol{Q}$ across the channel along the y-direction. It shows the predominant alignment directions of the nematic. The flow is from top to bottom. As expected, the molecules tend to align along the flow in the centre of the domain, and gradually transition to be perpendicular to the flow near the walls. The markers in Figure 6.9(b,c) show the computed profiles for all independent $\boldsymbol{Q}$ components, the velocity component v_1 (the x-component), and the shear stress τ_{21} in the LC stress tensor.

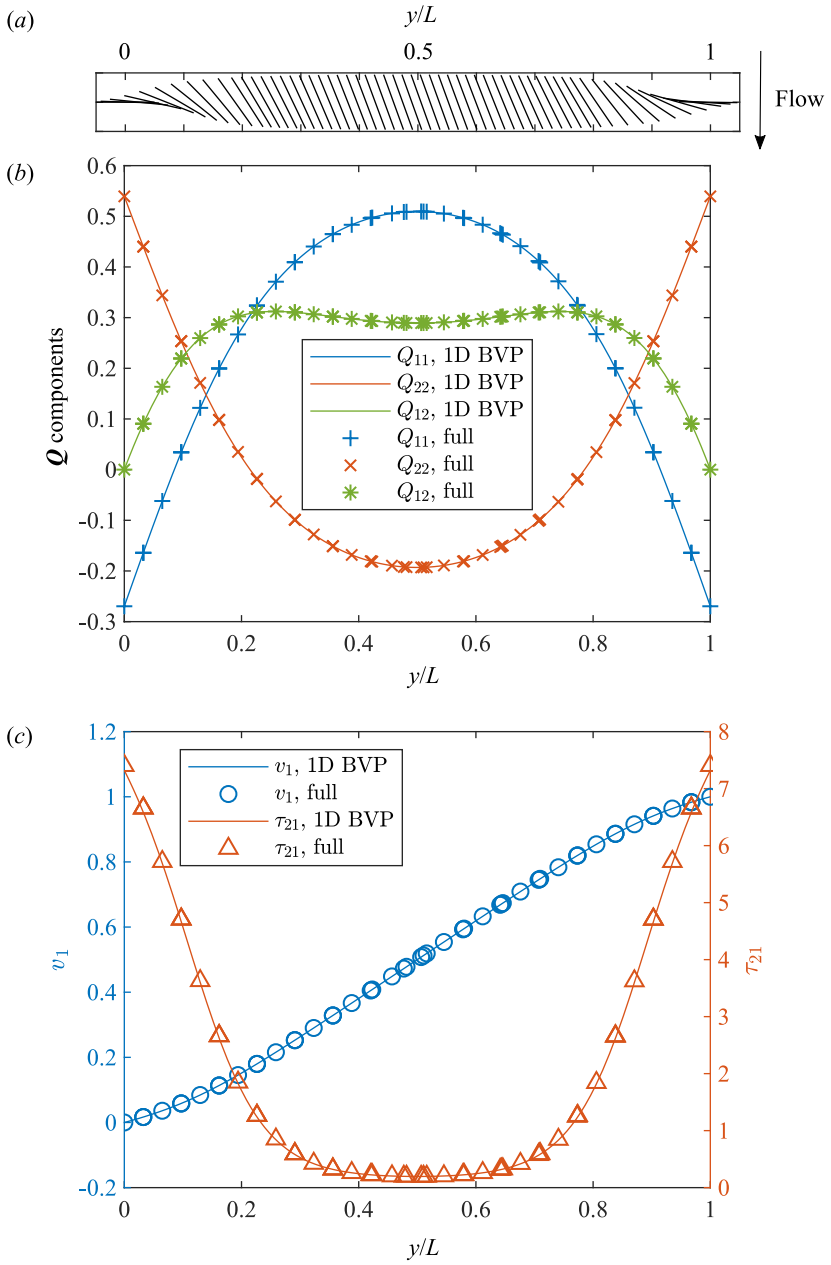

Figure 6.9: Flow aligning of nematic in a simple shear flow with anchoring on the walls. $De = 40$, $Er = 40$, $Pe = 40$, $Re = 0.1$. (a) Normalized dominating eigenvector of $\boldsymbol{Q}$ across the channel in the y-direction, showing predominant alignment directions. (b) Profiles of $\boldsymbol{Q}$ components across the channel from both the full calculation and the 1D BVP solution. (c) Profiles of the x-direction velocity component v_1 and the LC stress component τ_{21} across the channel, from both the full calculation and the 1D BVP solution.

The v_1 profile displays an "S" shape which agrees qualitatively with the results obtained using the LE theory under extreme material properties [188]. This is consistent with the increased value of the stress component τ_{21} near the walls. Constrained by shear stress balance, this increase is compensated by reduced Newtonian viscous shear stress, which is manifested in the reduced shear rate near the top and bottom boundaries.

For a quantitative validation, thanks to homogeneity along the x-direction, we reduce the problem of finding the steady state to a 1D Boundary Value Problem (BVP) in terms of the dependent variable

$$w = \left[\begin{array}{cccccccc} Q_{11} & Q_{22} & Q_{12} & Q'_{11} & Q'_{22} & Q'_{12} & v_1 & v'_1 \end{array} \right], \tag{6.7}$$

where the derivatives $Q'_{11},\ Q'_{22},\ Q'_{12},\ v'_1$ are taken in the y-direction. This 1D BVP is solved in the software package MATLAB [2] using a collocation method [76]. The results are shown also in Figure 6.9(*b*,*c*) with solid lines ("1D BVP"). Almost exact agreement between our full simulation and the reduced 1D BVP calculation is achieved.

6.1.3 Annihilation of defects

In this section, we validate our calculation of the dynamics of defects in bulk LC. Consider a pair of defects of winding numbers $1/2$ and $-1/2$, respectively. They can be regarded as points defects in 2D, or parallel disclination lines in 3D seen in a 2D domain perpendicular to the defect lines. It is well-known that topological defects of opposite winding numbers attract each other through elastic interactions to minimize the total elastic energy. Eventually they annihilate and the orientation field returns to a spatially uniform state consistent with the far-field alignment. The phenomenon has been studied in detail in [e.g., 166, 172].

A configuration of two defects of opposite half-integer winding numbers is initialized using the directors shown in Figure 6.10. The boundaries are for mimicking infinity. Therefore, they are non-penetrating walls with free slip for the flow field, and for the $\boldsymbol{Q}$ field vanishing gradients are imposed (Equation 4.36). We use the parameters from Tóth et al. [172] who solved the same BE model using a hybrid Lattice-Boltzmann and finite difference scheme. As a side remark, [172]

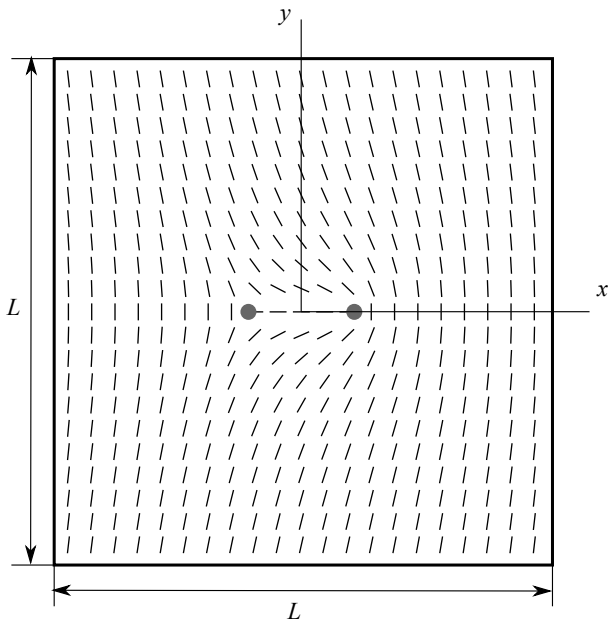

Figure 6.10: Computational domain for defects annihilation. The initial alignment is visualized in directors and the dark dots symbolize defect cores. The left defect has a winding number of -1/2 and the right one has a winding number of 1/2.

prescribed an unrealistically large time scale (i.e., almost infinite density for the fluid) presumably to facilitate numerical calculation. For comparison , we have used the same setting. In our computation, to resolve the defect cores sufficiently, we use a fine mesh in a rectangular region covering the trajectory of the defects. The mesh gradually coarsens towards the boundary.

Our simulation faithfully captures the physical features of interest in this process in the following two scenarios: (i) without flow, i.e., pure LC relaxation dynamics; (ii) with two-way coupling between flow, i.e., the LC stress induces a flow which in turn modifies defect motion. However, quantitative agreement in annihilation time with [172] is unfeasible because their exact initial distribution of $\boldsymbol{Q}$ is unknown to us. And based on our calculation, a slight perturbation in the initial configuration leads to drastic changes in the total time for annihilation. Therefore, we consider that a satisfactory agreement is achieved if annihilation times on the same order of magnitude as theirs are obtained.

LC relaxation dynamics

First, we consider a decoupled system in which the LC stress tensor is removed. In this case, without background flow, the $\boldsymbol{Q}$ field relaxes just by minimizing the total elastic energy. Provided that the distortional elasticity is isotropic, i.e., within the one-elastic-constant approximation (see Section 3.2), the trajectories of the two defects are symmetric with respect to the central line of the domain. In Figure 6.11(a), we show the time evolution of the loci of the two defect cores, together with that from Tóth et al. [172] ("TDY"). The defect with winding number 1/2 sets off from $x = 0.5$ μm, while the other sets off from $x = -0.5$ μm. Symmetry is captured well. From the slopes of the curves, one can also see the defects accelerate while they approach, as expected. Our annihilation time is about two thirds of that reported in [172].

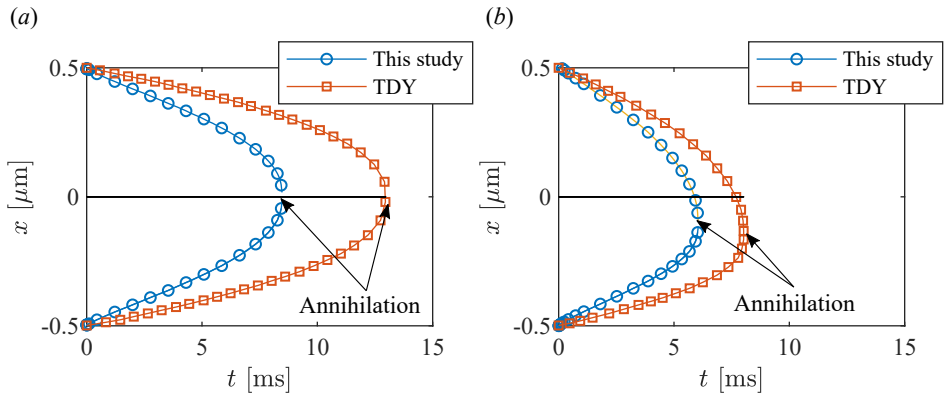

Figure 6.11: Evolution of the x-coordinates of the annihilating defect lines. The defect with winding number 1/2 sets off from $x = 0.5$ μm, while the other sets off from $x = -0.5$ μm. (a) Without back-flow. (b) With back-flow. Our results are compared with those taken from Figure 2 in [172] ("TDY").

Effect of back-flow

Next, we examine the situation when the $\boldsymbol{Q}$ relaxation is coupled with the flow. In general, the velocity field is stirred by the elastic stress generated by LC relaxation, and alters the $\boldsymbol{Q}$ evolution in turn. This phenomenon is termed "back-flow". For

our defects annihilation problem, it is well-known that there are two main effects from back-flow [172]:

(i) Reduced order around the defects leads to a high effective viscosity. It follows that each defect behaves like a solid inclusion, the translation of which creates a pair of vortices on both sides of its trajectory. These eddies advect the defects forward and accelerate their motion. Therefore, overall, the time to annihilation is shorter compared with the case without back-flow. This effect is captured in our simulation through the shorter annihilation time in Figure 6.11(*b*) compared to that in Figure 6.11(*a*).

(ii) The relaxation of nematic order creates additional vorticity in the flow field near the two defects. These vortices act in concord with the aforementioned effect to accelerate motion of the defect of winding number 1/2 (right defect), while for the defect of winding number -1/2 (left defect) they hinder the defect movement. Consequently, the symmetry in the trajectories of the two defects breaks down and the 1/2-strength defect moves faster than the other. Here we omit detailed explanation on the mechanism of this effect, but refer the reader to [172]. One sees that in Figure 6.11(*b*), the 1/2-strength defect has a steeper slope in its trajectory, resulting in annihilation to the left of the middle point $x = 0$. In addition, we show the velocity field in this simulation at $t \approx 3$ ms in Figure 6.12. The velocity magnitude is indicated by the colour map, as well as in logarithmic scale by the length of the velocity vectors. The defect cores are visualized by the region of $q \leq 0.3$ in green (Equilibrium scalar order parameter $q_e = 0.5$). The asymmetry in the speeds of the defects is evident.

With back-flow, our annihilation time also compares favorably with that in [172].

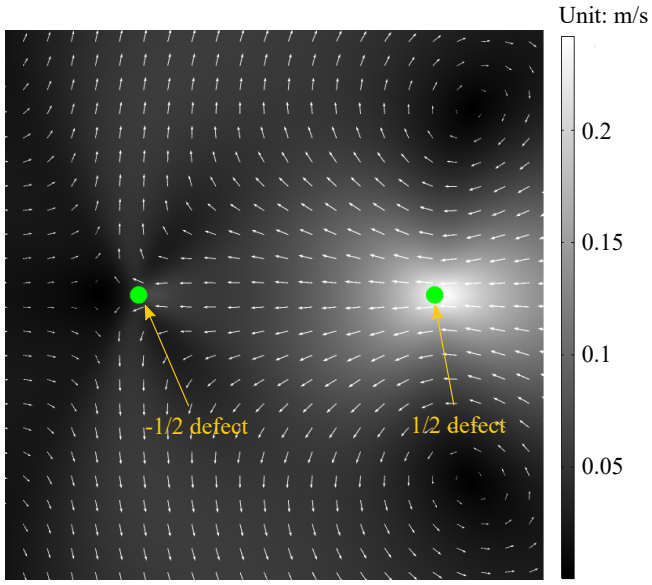

Figure 6.12: Velocity field near the annihilating defects with back-flow at $t \approx 3$ ms. The velocity magnitude is indicated by the colour map, as well as in logarithmic scale by the length of the velocity vectors. The green markers show the defect core regions ($q \leq 0.3$).

6.2 Drop retraction with a nematic phase

6.2.1 Introduction

In this section, we consider the problem of a micro-sized drop retracting in another medium, for either a nematic drop in an isotropic fluid or the inverse case. This problem serves two purposes. On one hand, it provides further validation to our computational framework by reproducing known results concerning multiphase flows of liquid crystals in the presence of topological defects. On the other hand, with the new model we uncover novel physical insight. It showcases the capability of our method.

In addition, there are three more reasons why we choose drop retraction as a model problem. First, drop retraction is driven by interfacial energy, which interacts with the elastic energies of a nematic, including the bulk and anchoring elastic energies. It provides a relatively simple ground for understanding the interplay among the energies, which underlies more complicated colloidal interaction under coupled elasto-capillary fields. Second, understanding drop retraction with a nematic phase is of potential use for measuring surface tension of LCs, which has been applied to Newtonian drops in isotropic fluids [115]. Third, understanding individual drop dynamics with a nematic-isotropic interface is crucial for studying more complex colloidal systems involving a nematic phase such as polymer-dispersed liquid crystals (PDLC) [42] and inverted nematic emulsion [119, 135].

A Newtonian drop retracting in another Newtonian medium has been thoroughly studied [e.g., 64, 107, 115]. With slight differences, several theories have predicted exponential decay of a drop deformation parameter in time. Rey pioneered a theoretical analysis of a nematic-isotropic interface using the LE theory [143–145]. He predicted that LC anchoring significantly alters interfacial behavior, including a Marangoni flow driven by anchoring energy gradient, and a bending stress. Experimental studies of LC drops retracting in a matrix were performed by a number of researchers [88, 179], who observed dependence of apparent surface tension on several factors such as drop size and interfacial LC alignment. Yue et al. [183] presented a brief computational study to probe a nematic drop retracting in an isotropic host in 2D. They showed the dynamic coupling between LC configu-

ration and surface tension. Consistent with earlier experimental observations, the results indicated that the apparent surface tension is no longer a material constant. The flow field and drop deformation also confirmed Rey's predictions. Liu et al. [98] used the same method and simulated an isotropic drop retracting in a nematic phase. The same final drop shape, elongated in the direction connecting the two surface boojums, was observed. These studies have provided a general theoretical understanding on the behaviour of a nematic-isotropic interface, and direct simulations for only a few scattered scenarios. However, much remains unexplored for more cases with different possible combinations of drop materials, anchoring condition and spatial dimensions. Further, the defect configurations observed in [98, 183] suffer from artificial constraints due to the regularized LC model used (see Section 3.2.2).

At the end of the retraction, the drop usually attains a non-spherical shape due to the elastic stress associated with the defect structure, which depends on other factors (see Section 6.2.4 and following sections). There has been much literature devoted to the final configuration of defect structures, such as reviewed in [85, 102, 151]. These investigations have elucidated how defects are affected by topological constraints, anchoring energy magnitude compared to bulk elastic energy magnitude, and curvature of the boundaries. However, most studies consider parameter ranges which result in negligible deformation, or in the other limit where surface tension is negligibly small. Therefore, there has been a lack of attention to interfacial deformation, especially quantitatively, and how it interplays with the bulk and anchoring elastic energies.

Here using our new model, we continue the effort in [183] and perform a systematic numerical study of the drop retraction problem with one of the two fluids being a nematic phase. We observe key features including the defect structures, the drop deformation and retraction rate modified by LC elasticity, consistent with earlier studies. We provide, however, a much more comprehensive map of drop configurations under various possible setups. Using numerical data, we uncover a proportionality relation between drop deformation at steady state and the elasto-capillary length, which signifies the competition between bulk distortional elastic force and surface tension. This linearity is explained by scaling arguments.

6.2.2 Problem setup

The problem setup is shown in Figure 6.13. In all cases considered here, the geometry and nematic alignment have quadrupolar symmetry, so we only need to simulate one quarter of the drop. On the symmetry boundaries, Equation 4.41 and Equation 4.54 apply. On outer boundaries, we use non-penetrating, free-slip walls. For all cases where the nematic phase is outside the drop, we specify the far-field LC molecules to be oriented in the vertical direction (y-direction in 2D planar geometry, and z-direction in 2D axisymmetric geometry) at equilibrium order. Hence, the BC of Equation 4.37 applies with $q = q_e$, and q_e is determined by Equation 3.8. On these outer walls, we do not need to keep the boundary terms for stress in the finite element formulation (Equation 4.74) because the box is large enough for Equation 4.36 to hold approximately. The drop is always placed with an initial elongation in the vertical direction. In most cases, we set the LC molecules to be initially aligned in the vertical direction at equilibrium order. Exceptions will be explained associated with the specific cases.

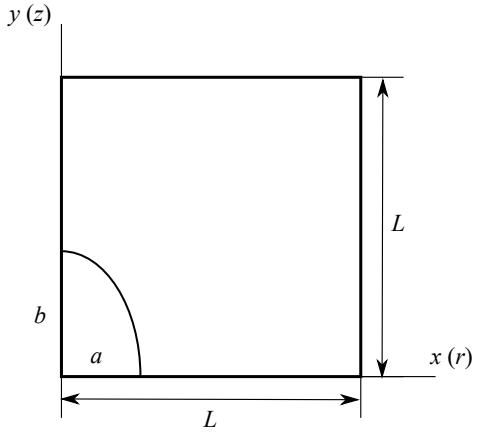

Figure 6.13: Computational domain of the drop retraction problem. In 2D planar geometry it is in the x-y plane, while in 2D axisymmetric geometry it is in the r-z plane.

For the purpose of this study, we prescribe a sub-domain with highly refined, near-uniform mesh size, covering the area through which the interface and defect move. Outside this sub-domain mesh sizes gradually coarsen. Figure 6.14 shows

the mesh structure in a typical simulation. From the time in Figure 6.14(a) to that in Figure 6.14(b), the interface sweeps through the interior of the refined region while the defect forms at the interface, detaches and moves towards the drop centre. Comparing these two plots, one can see that the interfacial region and the defect core are both well resolved from the start to steady state. Our setup is more efficient than the calculations in [98, 183] using a spectral method, and less costly than those in [188, 189] which adaptively refined their grids.

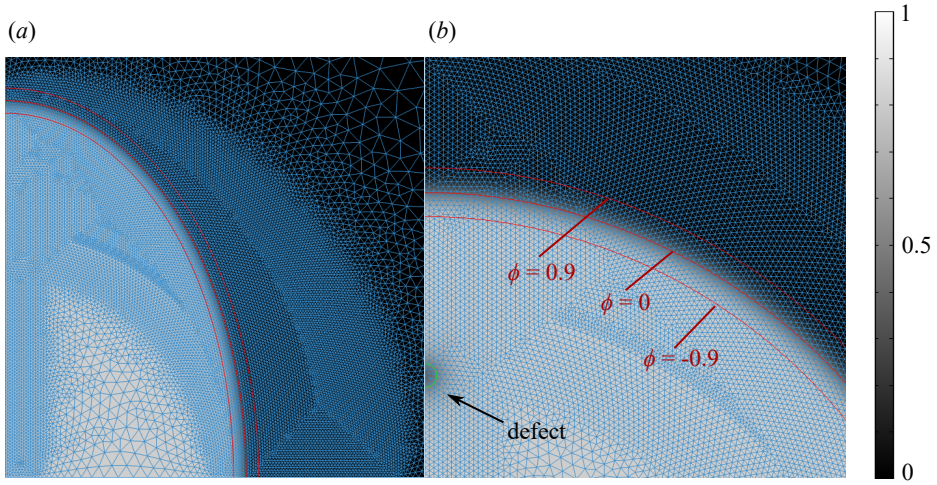

Figure 6.14: Mesh for drop retraction in a typical simulation where a nematic drop retracts in an isotropic medium in 2D planar geometry with planar anchoring at the interface. The contour lines show level sets of $\phi = 0$ (nominal interface), $\phi = 0.9$ and $\phi = -0.9$. The colour map indicates the concentration-weighted scalar order parameter $\frac{1-\phi}{2}q$. (a) Overview of the non-uniform triangular mesh at the initial time. (b) Details of the refined mesh at steady state. The dark spot is a defect with winding number 1/2, encircled by a green curve indicating the contour of $q = 0.5$.

Our material and geometry parameters are close to those for 5CB [70, 77, 138, 140]. For the LdG energy, again we use the $\tilde{A} - U$ system (Equation 6.1). With $U = 6$, the equilibrium scalar order parameter is $q_e = 0.8090$. Following Yue et al. [183], we employ a relatively large base value for the bulk elastic constant L_1 in order to make the nematic effect on the interfacial dynamics more pronounced. This factor will be taken into account in interpretation of the results. The numerical

Parameter	Symbol	Value
Material Parameters		
Bulk elastic constant	L_1	100 pN
LdG energy density	$\tilde{A}$	10^5 Pa
Nematic interaction strength	U	6
Nematic shape factor	ξ	0.6
Collective rotational diffusion coefficient	Γ	25 $\text{Pa}^{-1}\text{s}^{-1}$
Density of nematic	ρ_n	10^3 kg/m^3
Density of isotropic fluid	ρ_i	10^3 kg/m^3
Viscosity of nematic	η_n	0.01 Pa·s
Viscosity of isotropic	η_i	0.01 Pa·s
Surface anchoring strength	W_s	0.01 N/m
Surface tension coefficient	σ	0.01 N/m
Geometry Parameters		
Domain half edge length	L	5 μm
Nominal drop radius	R	1 μm
Initial drop size (2D planar)	b_0	1.25 μm
	a_0	0.8 μm
Initial drop size (2D axisymmetric)	b_0	1.25 μm
	a_0	0.8944 μm
Phase-Field Numerical Parameters		
Capillary width	ϵ	20 nm
Mobility (2D planar)	γ	4×10^{-14} m^2/(Pa·s)
Mobility (2D axisymmetric)	γ	4×10^{-15} m^2/(Pa·s)

Table 6.1: Typical parameters in the drop retraction problem.

parameters ϵ and γ are to ensure that we are close to the sharp-interface limit while not dampening interface motion with excessive CH diffusion (see Section 4.1 and Section 4.3). Table 6.1 summarizes all the dimensional parameters and their typical values used in this study.

6.2.3 Validation

We have ensured convergence by refining the mesh. We have also tested different box sizes, settings for the time-stepping algorithm, and numerical parameters, and the results have negligible differences. As further validation, we simulate the retraction of a Newtonian drop in isotropic fluid and match existing data.

We introduce the drop deformation parameter

$$D = \frac{b-a}{b+a}, \tag{6.8}$$

where $a,\ b$ are semi-axes lengths in the vertical and horizontal directions, respectively. Guido and Villone [64] gave a formula for the evolution of D under small deformations:

$$D = D_0 \exp\left(-\frac{40(\beta+1)}{(2\beta+3)(19\beta+16)}t^*\right), \tag{6.9}$$

where D_0 is the initial deformation parameter, β the viscosity ratio of the drop compared to the matrix. t^* is a dimensionless time, scaled by the capillary time $\eta_m R/\sigma$ where η_m is the viscosity of the matrix. This formula applies to a 3D spheroidal drop, thus we set our simulation in 2D axisymmetric geometry. We compute two retraction examples with $\beta = 1,\ 2$ and compare with Equation 6.9. To account for the assumption of small deformation, in agreement with [64, 190], we take the first time step after D falls below 0.09 in the simulation to be the start of the formula. For both β values, we have achieved satisfactory agreement between the numerical result (markers) and the analytical prediction (solid line, "GV"), as shown in Figure 6.15. Notice that deviation starts to appear at very small deformation, when the finite mesh size cannot resolve the interface motion any more [190].

6.2.4 Overview of different cases

We consider different scenarios including a nematic drop in an isotropic host and the inverse case, with planar or homeotropic anchoring on the fluid-fluid interface, in 2D planar (2D-planar) or axisymmetric (2D-axi) geometries. Figure 6.16 summarizes the final defect and drop configurations observed in different cases considered by our study. It serves as a map for our analysis below. We will first describe

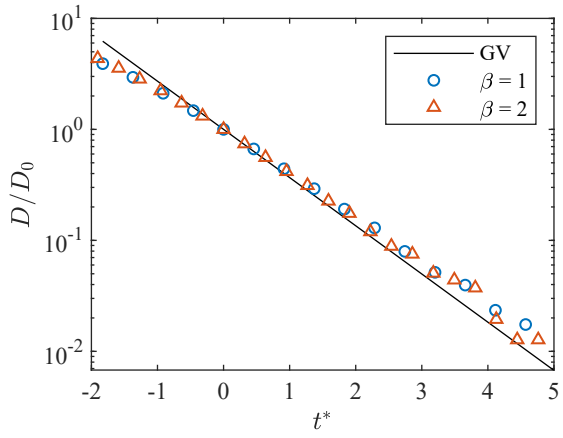

Figure 6.15: Computed Newtonian drop retraction in an isotropic medium for two different viscosity ratios, in comparison with the analytical prediction under small deformation by [64] ("GV").

general appearances of different cases. Then we address qualitative features, both common and contrasting among the cases. Finally we further examine the interplay between energies quantitatively. Comparison with literature is made whenever possible. In general, the configurations in Figure 6.16 have not been reported before except for Case 5, although many of them are not surprising. [98, 183] have studied Cases 1-3, but reported different results due to nonphysical defects (see Section 6.2.5).

Drop retraction in 2D-planar geometry

Case 1 in Figure 6.16 corresponds to a typical situation of a nematic drop retracting in isotropic fluid with planar anchoring in 2D-planar geometry. A series of snapshots in time are displayed in Figure 6.17. The dimensionless time t^* is scaled by the capillary time $\eta_i R/\sigma$, and the colour map indicates the scalar order parameter q. The interface is denoted by the red curve, while the defect core is visualized using the contour of $q = 0.5$ in green. Initially the LC molecules are aligned in the y-direction at equilibrium order (Figure 6.17a). The elongated drop starts retracting under surface tension to minimize interfacial energy $\int f_m \, dV$. Meanwhile, the LC molecules near the interface reorient such that anchoring energy $\int f_a \, dV$ is re-

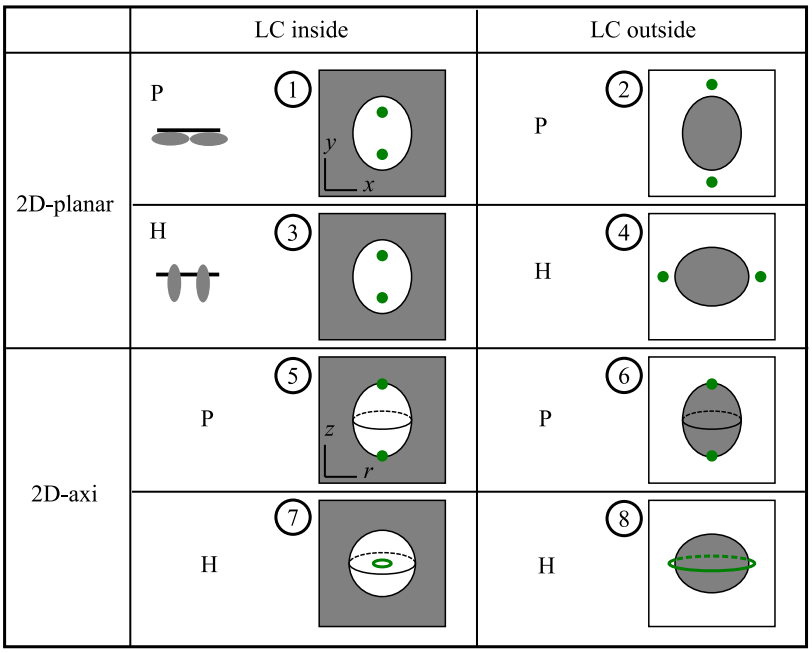

Figure 6.16: Overview of final defect and drop configurations after drop retraction with a nematic phase. Defects are marked by green points or lines. The drop deformation may be exaggerated for clarity. P = planar anchoring. H = homeotropic anchoring. These anchoring conditions are illustrated in the cells for Cases 1 and 3.

duced. These are at the expense of the bulk elastic energy $\int \frac{1-\phi}{2} f_b \, dV$. Therefore, as a pair of boojums nucleate at the top/bottom poles of the drop, a repelling elastic force arises between these defects (Figure 6.17*b*,*c*). While anchoring continues being established, the defects detach from the interface and move into the bulk of the drop, transitioning from surface boojums to a pair of defects of winding number 1/2. Eventually, the reduction in interfacial energy and anchoring energy balances the rise in bulk elastic energy, and the retraction comes to an end (Figure 6.17*d*). The drop maintains a slight elongation in the y-direction such that surface tension is in balance with the elastic stress due to distortion in the $\boldsymbol{Q}$ field.

Case 2 has the same setup with Case 1, except that the drop is isotropic while the matrix is nematic. Certainly the defects form outside the drop. At steady state, a pair of defects of -1/2 winding number are at the poles of the drop, also detached

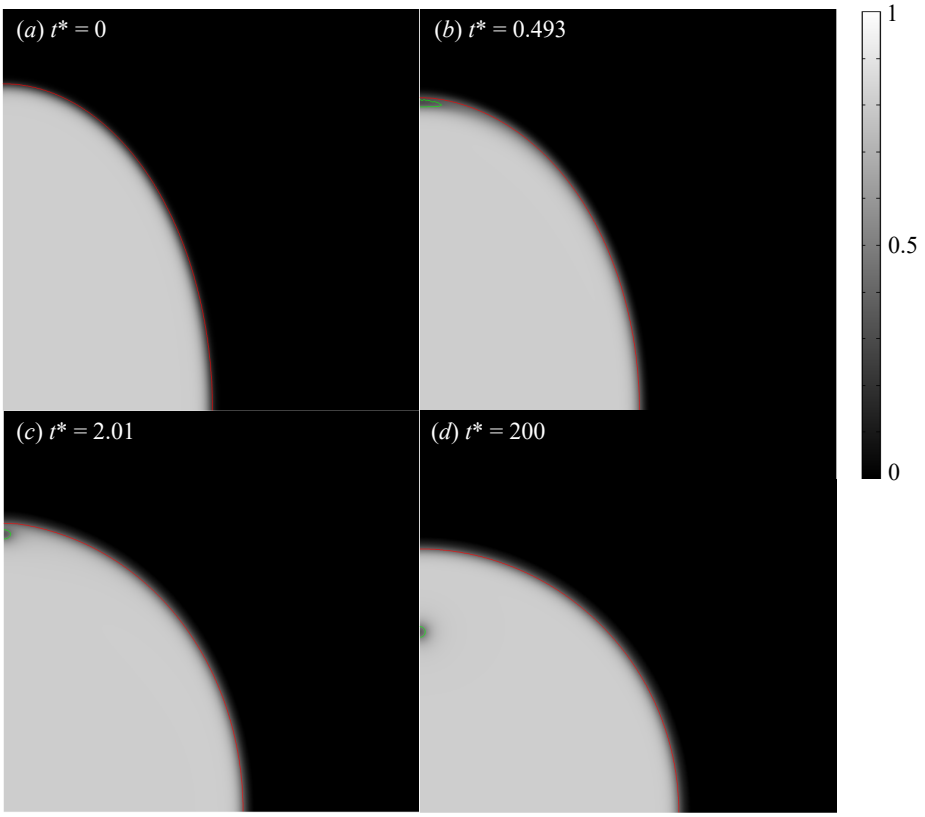

Figure 6.17: Snapshots of a typical simulation of Case 1 in Figure 6.16 (N in I, P, 2D-planar, only simulating a quarter of the domain). The gray scale shows the scalar order parameter q. The nominal interface $\phi = 0$ is marked in red, and the contour of $q = 0.5$ is marked in green representing the boundary of the defect core. (a) Well-aligned state at initial condition. (b) As the drop retracts, defects start to form at the poles of the drop. (c) The defect forms at the interface. (d) The defect detaches from the interface and moves inside the drop. Both the drop shape and defect location come to steady state.

from the interface.

Case 3 shows a nematic drop retracting in an isotropic medium, with homeotropic anchoring on the interface. The initial LC alignment is along the x-direction, still at equilibrium order. This leads to a retraction procedure rather similar to Case 1, resulting in a pair of $s = 1/2$ defects in the bulk of the drop near the poles.

Case 4 displays the steady state of an isotropic drop after retracting in a nematic phase, with homeotropic anchoring on the drop surface. A pair of defects of $s = -1/2$ nucleate at the waists of the drop, and detaches to move inside the nematic phase. This is the 2D analog to the Saturn ring defect shown in Section 6.1.1. After retracting in the y-direction, the drop further stretches in the x-direction.

Drop retraction in 2D-axi geometry

We also assume axisymmetry and simulate the drop retraction problem in the r-z plane. Cases 5 and 6 in Figure 6.16 both have planar anchoring on the drop surface, with nematic in isotropic, and isotropic in nematic configurations, respectively. Similar to Cases 1 and 2, two defects form at the poles of the drops. What is different from the 2D-planar cases is that, the defects are attached to the surface and are thus true boojums. This is a result of the different topology in 3D compared to 2D (see Section 6.2.5).

Case 7 deals with a nematic drop inside an isotropic host with homeotropic anchoring. The initial $\boldsymbol{Q}$ field is set up so that LC alignment is radial with respect to the drop centre. A small ring defect forms around the centre. This is reminiscent of the polar ring, which opens up spontaneously from a point defect near a spherical particle submerged in a nematic LC with parallel far-field alignment and homeotropic anchoring at its surface (see Section 6.1.1). The ring is oriented perpendicular to the z-direction, as determined by the initial alignment along the z-axis. Thanks to the small size of the ring, the drop retracts to an isotropic sphere almost completely.

Cases 8 reverses the materials in Case 7, still with homeotropic anchoring. The initial $\boldsymbol{Q}$ configuration is alignment in the z-direction. The retraction results in a Saturn ring and an oblate spheroid.

Note that the exact combinations of defect configuration and drop deformation in Cases 1-4 have not been reported before for true nematic phases in 2D-planar, nor has that for Case 8 in 3D. Case 1 has been investigated as a simplified 2D model in [112] for the so-called "tactoids", which are highly elongated nematic droplets usually experimentally seen in lyotropic LCs. Only interface-bound defects have been reported because of the low surface tension and high elongation. Cases 5 and

6 have been studied with prior investigations [102]. Case 7 has also appeared in earlier studies up to the difference of a point or ring defect in the centre. Having described briefly all the different cases, we will now examine in more details some qualitative features in the next two sections, as well as compare to existing literature.

6.2.5 Defect structures

The establishment of anchoring and thus topological constraints leading to defects are in line with the relationship of energy magnitudes in our study. We introduce the dimensionless *anchoring extrapolation length* scaled by the nominal drop radius, $l_e^* = L_1/(W_s R)$, which is a dimensionless group representing the magnitude of distortional elastic energy compared with anchoring energy. Using parameters from Table 6.1, $l_e^* = 0.01 \ll 1$. Hence, we are in a regime where anchoring is enforced with existence of defects [85], in agreement with what we see in the simulations.

As a necessary condition, all the defects we have obtained through the simulations are consistent with topological constraints, which are results of the Gauss-Bonnet theorem [75, 85, 151]. For nematic drops in 2D-planar (Cases 1 and 3), and drops in 3D with planar anchoring (Cases 5 and 6), the total winding numbers of the defects in our results satisfy the Poincaré theorem. In particular,, it dictates that on the planar-anchored spherical surface (Cases 5 and 6), there must be defects of total winding number $s = 2$. Therefore the two boojums in our simulations have to be bound to the interface. The homeotropically anchored nematic drop in 3D and its defect (Case 7) satisfy the Gauss-Stein theorem. All other cases with a nematic medium (Cases 2, 4, and 8) have defect structures which, combined with the drop surface itself, give total $s = 0$, consistent with uniform alignment in the far field.

These defect structures are also consistent with earlier studies in energetic stability. First, it has been well known that integer-strength defects described by the LdG energy with one-constant approximation are unstable in 2D-planar [57]. Indeed, for Cases 1-4, we have always predicted a pair of half-integer strength defects instead of an integer-strength defect. To further verify the stability of the defects pair, in Case 3 we test a different initial configuration, i.e., radial alignment of LC

molecules. The transient phenomenon is different from the original simulation. A defect of $s = 1$ nucleates at the drop centre. Nevertheless, as the drop retracts, this defect splits up into two half-strength defects, settling into the same configuration as in the original simulation with horizontal initial alignment. Second, for Case 7, a small ring spontaneously opens up from a point defect of $s = 1$, which is reminiscent of the polar ring near a sphere with homeotropic anchoring (see [58, 140] and also Section 6.1.1).

Cases 1 and 3 were probed previously by Yue et al. [183] who found different defect structures than us. In [183], the defects pair are constrained on the interface with planar anchoring, while a point defect of $s = 1$ forms at the centre with homeotropic anchoring. Both are artifacts caused by the regularized LE theory (see explanations in Section 3.2.2). The same difference occurs for [98] which briefly studied Case 2. Related to the discussions here, in experiments, free-standing smectic-C films are often used to model 2D-planar LCs [44]. However, due to the loss of head-tail symmetry of the LC molecules, it has different properties from a true nematic phase in 2D-planar. One example is that half-integer strength defects are not allowed, thus defects in a cylindrical inclusion are surface-bound with planar anchoring. The results in [183] are therefore more applicable to those systems.

6.2.6 Drop deformation and Marangoni flow

For the deformation of the drop during and after the retraction, in Section 6.2.4, we have provided an explanation for Case 1 from the perspective of competition between forces from different energy components. The same general argument works for all other cases except for Case 8, where the Saturn ring does not necessarily reduce distortional elastic energy by expanding. To account for that, we turn to the role of the nematic-isotropic interface which mediates the interaction between bulk elastic and surface energies. Rey has pointed out that a bending force on the interface results from a gradient of anchoring energy [144, 145], which has been numerically verified in [183]. In Case 8, despite that our defect is not attached to the interface as in [183], the proximity between the defect and the drop surface still leads to small deviations in the $\boldsymbol{Q}$ configuration from perfectly anchored at the interface

near the drop waist. Consequently, there is higher anchoring energy at the waist than the pole of the drop. This is clearly shown by the anchoring energy density non-dimensionalized by the distortional elastic energy scale $f_a^* = f_a/(L_1/R^2)$, towards the end of the retraction in Case 8 ($t^* = 149$), in Figure 6.18. According

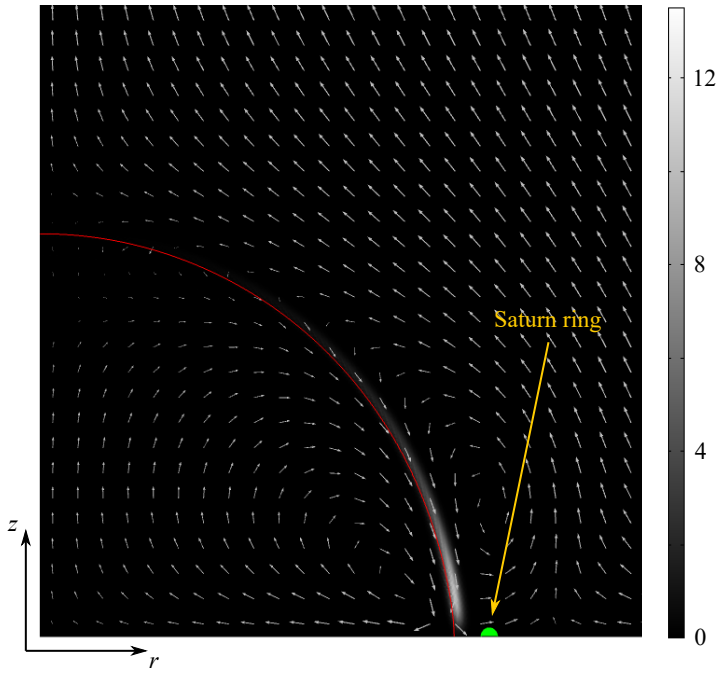

Figure 6.18: Anchoring energy density and velocity field for Case 8 near the end of the retraction ($t^* = 149$). The colour map shows the dimensionless anchoring energy density f_a^*. The interface is shown by the red curve, and the green area denotes the defect core ($q \leq 0.5$). The drop elongates slightly in the r-direction. The arrows show the velocity field in logarithmic scale, displaying the Marangoni flow caused by the anchoring energy gradient.

to Rey's theory, the higher anchoring energy at the waist of the drop will cause enhanced bending of the interface, leading to increased curvature. This explains the elongation of the drop in the r-direction observed in our simulation. Both these arguments (energetic and force-based) have been used also in [98, 183].

The gradient in anchoring energy drives a Marangoni flow along the interface from locations of low anchoring energy to those of high anchoring energy, pre-

dicted by [143]. It has been captured in our simulations, as again shown for Case 8 in Figure 6.18 by the velocity field. Similar flows have been identified for other cases as well. Note that in early time of retraction, this Marangoni flow is completely dominated by the global eddies created by the fast deformation of the drop. Only towards the end of the retraction when the main flow field has more or less died down can we observe the Marangoni flow clearly. By this time, though, the anchoring energy gradient has declined much and the Marangoni flow has also become much weaker. In [183] similar numerical results were observed.

6.2.7 Retraction rate

We analyze the retraction speed for Cases 1-4 in Figure 6.19, which shows the time evolution of the deformation factor D in log scale. Cases 1-4 are compared with a Newtonian drop retracting in an isotropic medium with the same fluid properties (designated as "Case i"). Similar to a Newtonian drop retracting in an isotropic host in 2D-axi (Section 6.2.3), the decay of D is exponential before it slows down to approach steady state. Cases 1-3 all retract slower than Case i, because the elastic repulsion between the defects in the y-direction hinders retraction. Case 4 retracts faster than Case i, because the drop stretches in the x-direction under the inhomogeneous bending force on the interface, accelerating retraction in the y-direction. In fact, since $b - a$ in Case 4 eventually becomes negative, its retraction curve tends to $-\infty$.

The evolutions of D for Cases 5-8 are shown in Figure 6.20 in comparison with Case ii, which is the counterpart of Case i in 2D-axi. Early-time exponential decay of D is again evident. Similar to the 2D-planar cases, Cases 5 and 6 retract slower than Case ii as the surface boojums in the z-direction resist drop retraction. Case 7 almost overlaps Case ii because the defect at the centre hardly affects the retraction rate nor the final drop shape. Finally, the drop in Case 8 retracts faster thanks to elongation in the r-direction.

The retraction speed obtained here agrees with the trend observed in [183], despite the different defect structures.

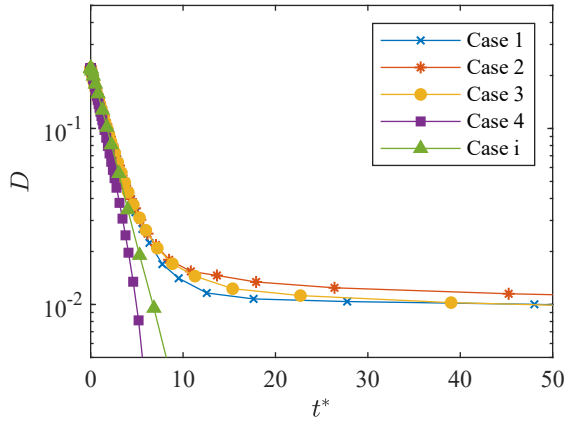

Figure 6.19: Time evolution of drop deformation factor D in time for Cases 1-4 compared with Case i.

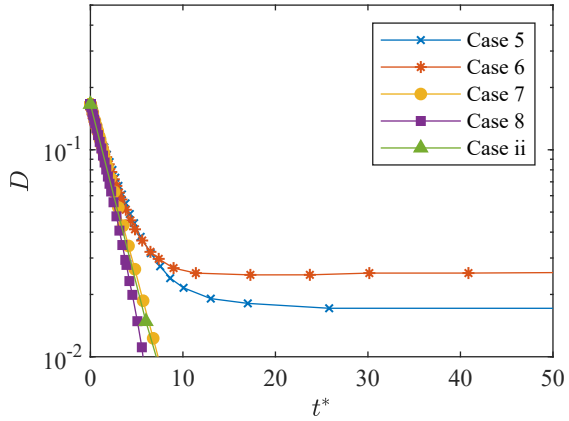

Figure 6.20: Time evolution of drop deformation factor D for Cases 5-8 compared with Case ii.

6.2.8 Drop shape in steady state

From the qualitative analysis in Section 6.2.6, we have established that the drop deformation is mainly a consequence of competition between the bulk distortional elastic energy and conventional interfacial energy (surface tension), mediated by anchoring energy. To further strengthen this point, we examine the non-spherical

drop shape in steady state quantitatively. We start by offering a simple analysis predicting that the drop deformation is proportional to an intrinsic characteristic length which comes out of the competition between the bulk distortion of $\boldsymbol{Q}$ and surface tension. Then we show numerical data to validate this relationship. The following analysis and data are original contribution of this thesis and have not been published before.

Let $b_s,\ a_s$ denote the steady-state semi-axes lengths of the drop, in the vertical (y or z) and the horizontal (x or r) directions, respectively. We consider how the length $b_s - a_s$ could depend on the parameters in this problem. Among the length scales admitted, the *elasto-capillary length* $l_{ec} = L_1/\sigma$ arises from the competition between distortional elastic energy with surface energy. Hence, we hypothesize that $|b_s - a_s|$ is proportional to l_{ec}.

We now make the proportionality argument more precise with a scaling analysis. Consider a drop in planar 2D geometry (Cases 1-4). Either the drop or the matrix is a nematic phase. Without loss of generality, let us assume that $b_s > a_s$. We first conceive a virtual "base state", in which a prescribed circular drop of radius R is held unchanged in shape, while the $\boldsymbol{Q}$ field has relaxed fully and the defects pair have formed. In the nematic phase, the distortional elastic energy density is approximately $f_e \approx L_1/\zeta^2$, where ζ is the characteristic length scale of $\boldsymbol{Q}$ distortions. One could pick the distance between the two half-strength defects as ζ. If the drop is nematic, then $\zeta < 2R$. If the host is nematic, then $\zeta > 2R$. Now we introduce a deformation of the drop such that it elongates by $\delta l > 0$ in one direction, i.e., $b_s = R + \delta l$. Assume that δl is small, then considering conservation of drop area, $a_s = R - \delta l$ to leading order. This will change the distortional elastic energy density approximately to $L_1/(\zeta + 2\delta l)^2$. We assume that the characteristic region with the average distortional elastic energy density f_e has an area of A_e, which approximately equals the drop area πR^2 if the drop is nematic, but is likely to be much larger if the surrounding medium is nematic instead. The change in total distortional elastic energy (per unit length in 2D) is approximately

$$\delta F_e \approx -\frac{4A_e L_1}{\zeta^3}\delta l. \tag{6.10}$$

As expected, the total distortional elastic energy decreases with enlarging distance

between the defects.

The change in the circumference of the drop is $3\pi\delta l^2/R$ to leading order. Therefore, the change in surface energy is approximately

$$\delta F_s \approx \frac{3\pi\sigma}{R}\delta l^2. \tag{6.11}$$

One can see that the reduction in distortional elastic energy scales with δl, while the increase in surface energy scales with δl^2. This gives an equilibrium δl corresponding to the lowest total of the two energies. Equating the magnitudes of the two energy changes we get

$$b_s - a_s = 2\delta l \approx \frac{8A_eR}{3\pi\zeta^3}\frac{L_1}{\sigma} = \frac{8A_eR}{3\pi\zeta^3}l_{ec}. \tag{6.12}$$

Indeed under small deformations, $b_s - a_s$ is proportional l_{ec}.

The scaling relationships $\delta F_e \propto L_1\delta l$ and $\delta F_s \propto \sigma\delta l^2$ can be established in 3D with axisymmetry, in the same way as above. The proportionality between δl and l_{ec} then follows.

Numerical data confirms this proportional relationship. Figure 6.21 shows dimensionless drop elongation scaled by the nominal drop radius $|b^* - a^*| = |b - a|/R$, as a function of the dimensionless elasto-capillary length $l^*_{ec} = l_{ec}/R$, for Cases 1-4 in 2D-planar. The parameters presented in Table 6.1 give $l^*_{ec} = 0.01$. $l^*_{ec} = 0$ corresponds to an infinitely large surface tension, with which the drop deformation should vanish. Other l^*_{ec} values are obtained by changing surface tension σ. In all cases, the deformation $|b^* - a^*|$ indeed is approximately proportional to l^*_{ec}. The same applies to 2D-axi cases (Cases 5-8), as shown in Figure 6.22. Case 6 is degenerate due to the vanished drop deformation.

As shown in the data, this scaling persists in situations where the deformation magnitude $|b - a|$ is even moderately large, reaching almost 20% of the drop nominal radius in 2D-planar cases, and more than 30% in 2D-axi cases. Furthermore, for some cases with a relative large l^*_{ec} (e.g., Cases 2 and 4 with $l^*_{ec} \geq 0.05$), the defects stay on the interface and never detach. It suggests that the low price of interfacial energy (surface tension) combined with reduced distortional elastic energy offsets the increased anchoring energy. Even then, the drop deformation

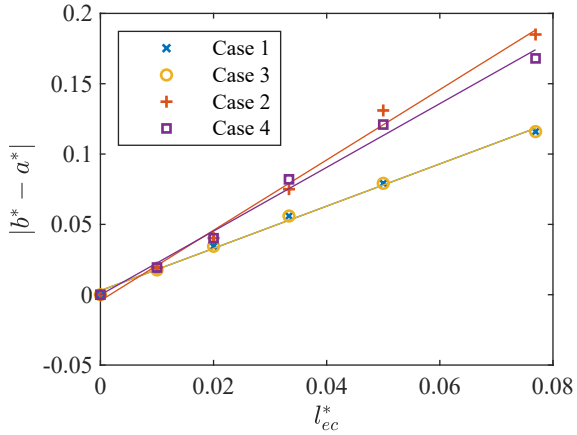

Figure 6.21: Final drop deformation $|b^* - a^*|$ as a function of the elasto-capillary length l^*_{ec} for 2D-planar cases.

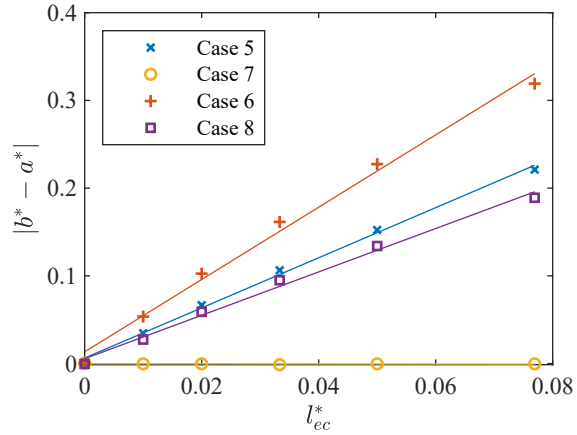

Figure 6.22: Final drop deformation $|b^* - a^*|$ as a function of the elasto-capillary length l^*_{ec} for 2D-axi cases.

$|b^* - a^*|$ remains approximately proportional to l^*_{ec}.

In 2D-planar, in Cases 1 and 3 (nematic drop in isotropic fluid), the drop deformations at different l^*_{ec} values are almost always the same. Examining the steady-state configurations in these two cases, we find the defect locations are also almost the same. It suggests effects from the strong confinement of the drop. The rates of

increase in $|b^* - a^*|$ with increasing l^*_{ec} (slopes of the fitting lines in Figure 6.21) in Cases 1 and 3 are lower than those in Cases 2 and 4. This is likely a consequence of a much larger A_e or a much smaller ζ in Cases 3 and 4 with a nematic host compared to LC being constrained inside the drop (see Equation 6.12).

The proportionality between $|b^* - a^*|$ and l^*_{ec} implies that mainly the interaction between the distortional elastic energy and the surface energy, mediated by the anchoring energy, determines the drop deformation, in the range of parameters we have considered.

6.3 Summary for Problem II

In this part of the thesis, we have considered the problem of elasto-capillary phenomena in liquid crystals. We have developed a computational framework that integrates a tensorial description of molecular order in nematic LC with a phase-field formalism that approximates the sharp-interface limit of two-phase flows. This method allows consistent description of topological defect structures in the LC, while capturing interfacial forces including surface tension and LC anchoring stress accurately. The method is validated using various tests of single-phase LC flows.

We further demonstrate the capability of our method by applying it to the problem of drop retraction involving a nematic phase. We have provided a comprehensive map of drop-defect configurations in a variety of cases, including nematic drop in an isotropic phase or vice versa, planar or homeotropic anchoring at the interface, in 2D-planar or 2D-axi geometries. Most of the exact configurations have not been reported or studied before. We have characterized the dynamic retraction process in each case, and interpreted the resulting LC alignment and drop shape in the language of competing energies and nematic-isotropic interfacial forces. These results agree with existing literature so as to validate our computation, and we further contribute new physical insights by quantitatively examining the drop deformation at steady state. For the first time, we report that the characteristic drop deformation $|b^* - a^*|$ is proportional to the elasto-capillary length l^*_{ec}. This relation exists in almost all configurations explored here, which indicates that the regimes under consideration are dominated by the competition between bulk distortional elasticity

and surface tension. These discoveries highlight the interplay between the elastic energy and surface energy mediated through anchoring energy at the interface.

Future directions for this problem can be grouped in two aspects: methodology and physics. From the methodology perspective, the drawback of our method, as common in PF models, is the high computational cost. It is partly because of the high order (fourth) of CH equation, and partly due to the demand of high mesh density in the interfacial region. This is particularly limiting when extending to 3D calculations. Various possibilities exist to improve the computational speed. Efficient adaptive meshing schemes such as in [130] can be considered. The recent scalar auxiliary variable method developed by Shen et al. [153] is a promising candidate to accelerate solution of the CH equation.

From the physics point of view, our PF method provides a flexible tool to study a large class of problems involving coupled LC elasticity and capillarity. Possible directions include the following.

(i) The drop retraction problem can be extended in two ways. First, our current study has only explored drop retraction with a strong anchoring at the interface (small l_e^*). If the anchoring energy is low and comparable with the distortional elastic energy, the drop retraction may display different dynamics. Second, we have restricted ourselves to be within the one-constant approximation for the distortional elastic energy of LC. It is straight-forward to include other bulk elastic constants to account for anisotropic distortional energy [e.g., 38, 140]. Adopting a more refined description of distortional elastic energy is likely to admit even richer configurations of the drop and its associated defects.

(ii) In the case of solid particles trapped at interfaces of LCs, moving contact lines can be readily incorporated into our computation. A moving mesh approach such as ALE (see Section 4.1) may be coupled with existing calculations to account for the particle motion. Then the elasto-capillary interaction between colloids introduced in Section 3.1 can be fully addressed. One could investigate a single particle or multiple interacting particles on the interface of an LC, in both stationary or dynamic situations. These studies can be carried out also for a globally curved interface.

(iii) By letting the LdG coefficients in Equation 3.7 be dependent on temperature or concentration, we can extend our model to describe phase transition for thermotropic LCs, or dynamics of lyotropic LCs. This allows for further studies on LC multiphase flows near the isotropic-nematic transition. Such phenomena have been studied thoroughly in the bulk of LC [e.g., 41], but little in the presence of a fluid-fluid interface.

Chapter 7

Conclusion

7.1 This thesis

In this thesis, we present two case studies in computational modeling of interfacial dynamics of complex fluids. The problems we have chosen are (i) the interaction between a pair of ferrofluid drops in a rotating magnetic field; (ii) elasto-capillary flows of liquid crystals (LCs). There are two parts in (ii): development of a phase-field (PF) method to compute the flow, and applying it to the drop retraction problem. We have justified the novelty of these two problems in the specific context of knowledge on ferrofluid and LCs, in Chapter 2 and Chapter 3, respectively.

We have made detailed summaries on the methodology that has been taken, results obtained, limitations and future directions for each problem in Section 5.3 and Section 6.3. Here, I recall the specific progress made by this thesis to the field of interfacial dynamics in complex fluids.

The ferrofluid drop interaction problem

(i) Using direct numerical solution with a volume-of-fluid (VOF) method, we have systematically classified interaction regimes of a pair of ferrofluid drops in a rotating magnetic field. We have presented arguments to explain the transition between these regimes.

(ii) We have demonstrated that the planetary motion of the drops is dominated by

a hydrodynamic interaction, termed viscous sweeping. With this argument, we are able to interpret features of the drop motion which are not explained by magnetic dipole interactions.

(iii) The simulation has discovered a regime that is not known previously, i.e., the drop locking regime. Informed by our choice of parameters, new experiments conducted at a collaborator's lab have observed this regime.

The LC elasto-capillary flows problem

(i) We have constructed a PF formulation for computing the elasto-capillary flows of nematic LCs. The advantage of this method over previous models is to achieve a consistent description of the nematic order, including topological defects, and accurate recovery of interfacial forces, including surface tension and nematic anchoring stress, simultaneously.

(ii) We have validated the model using a variety of numerical examples in the case of single-phase, bulk nematic flow.

(iii) The method has been applied to the drop retraction problem. It further validates our model by reproducing key features consistent with physical principles and existing literature.

(iv) Our study of the drop retraction problem has provided a comprehensive map of possible defect structures and drop shapes, as a result of different combinations of drop-matrix material pairs, anchoring conditions, and spatial dimensions. Many of these configurations have not been reported before.

(v) We have found that the drop retraction dynamics and steady-state shapes are mainly a result of competition between nematic distortional elastic energy with surface energy, mediated by anchoring energy at the interface.

(vi) In particular, in the range of parameters considered, we have uncovered a direct proportionality between the drop deformation at steady state and the elasto-capillary length.

7.2 Future directions in computational studies of interfacial phenomena of complex fluids

The work presented in this thesis spans several topics in soft matter physics and stages of developing and using computational tools. In the following, we put the contribution of this thesis in a broader context, together with general research directions for computational studies of interfacial dynamics of complex fluids. The discussion can be from two aspects: computational methodology and application to physics. These two aspects are closely related. The development of modern methods has enabled studies at new frontiers of physics, while the need to solve challenges by nature continues driving innovations in methodology.

Methodology

The development of computational models to compute flows with moving interfaces has been far from complete. The methods mentioned in Section 4.1 provide conceptual frameworks for modeling interfacial flows, while applying them to complex fluids and obtaining results that can explain experiments are non-trivial. It usually requires refinement of the model or development of new numerical schemes based on the specific fluids under consideration.

We take the elasto-capillary flow problem as an example. In this thesis, we have contributed a PF framework that takes into account of one nematic phase in a two-phase flow. We are able to accurately capture macroscopic interfacial forces and defect structures at the same time, which has not been satisfactorily addressed in previous literature. It is a significant step in tackling the elasto-capillary interaction problems (Section 3.1). Meanwhile, the limitation of the PF method, mainly the computational cost, needs to be lifted. Note that the cost issue is not limited to the LC material in our study, but also applies to the modeling of other complex fluids as well. One direction of research, as already mentioned in Section 6.3, is improved numerical schemes for solving the gradient dynamics including the CH equation and possibly the evolution of the microstructure of the complex fluid [e.g., 23, 153]. Another direction is to further develop sharp-interface methods to overcome the challenges such as imposing interfacial force balance [e.g., 5, 92]. Extension along these two lines is valuable future work for computing multiphase

flows of complex fluids, including LCs.

A trend worth noting in the computational studies of physics is the increasingly important roles played by software packages. The stacking complexities in the physics being considered and the sophistication of the numerical schemes employed call for specialization and collaboration among researchers. The work presented in this thesis is made possible by harnessing the power of well-developed softwares, both open-source and commercial.

Applications

As introduced in Chapter 1, in various interfacial phenomena involving complex fluids, the interplay between surface tension and complex rheology has been the central theme. This thesis continues effort in this theme, and demonstrates such novel interplay in two systems. For a pair of ferrofluid drops, individual drops are driven by magnetic forces. Their motion causes a hydrodynamic interaction (viscous sweeping) thanks to the magneto-capillary coupling. For a drop retracting in a medium with one of the two phases being nematic, defect structures, dynamic apparent surface tension, and drop deformation are all signatures of the interaction among bulk elastic, anchoring, and interfacial energies. We have outlined future plans along the same line of coupled physics in Section 5.3 and Section 6.3.

A further extension is on multi-scale problems. After understanding the dynamics of individual or a few drops or particles, it is natural to explore the behaviour of a large number of colloids under coupled surface tension and complex rheology. For the case of ferrofluid, computation is promising to bridge the dynamics of single droplets with the rheology of an emulsion of ferrofluid droplets [36]. For the case of LCs, as has been demonstrated experimentally [e.g., 158], colloidal particles absorbed on the interface of an LC self-assemble into a structured lattice with a high stability. The resulting soft material has properties that depend on the elasto-capillary interactions. Computational studies could be used in the design of such materials.

There is also a noticeable increase in applications of interfacial dynamics of complex fluids in biological problems. As mentioned in Chapter 2, ferrofluid drops have been proposed as a tool in biomedical applications [110, 152, 175]. In particu-

lar, Serwane et al. [152] compared the relaxation of an elongated ferrofluid droplet in a biological tissue to a reduced 1D model and successfully backed out the mechanical properties of the surrounding tissue. The 1D model was fitted from direct numerical calculations of a 3D drop in [148]. In addition, complex fluids have been used as model systems to understand behaviour of active matter. One such instance involves a mixture of microtubules and molecular motors at the water-oil interface [45]. Due to the cross-linking by the active molecular motors, the microtubules align in parallel spontaneously, which makes the mixture nematic. LC hydrodynamic models can be extended to model such systems, and direct numerical simulations have showed the so-called "active turbulence". The methods used and developed in this thesis can be readily applied to the subjects above. Furthermore, morphogenesis, in which tissues undergo transitions in morphology during the process of development, has also been studied from the perspective of interfacial phenomena of complex fluids. In [129], tissue spreading has been shown to be understood by a wetting transition of a fluid with an active stress. Proliferating examples show that new frontiers are being opened up in life sciences, offering a fruitful ground for interfacial flows approaches including computations.

Bibliography

[1] COMSOL Multiphysics® v. 5.4. www.comsol.com. COMSOL AB, Stockholm, Sweden. → page 57

[2] MATLAB r2018a. https://www.mathworks.com/. The MathWorks, Inc. → page 92

[3] MUMPS: A parallel sparse direct solver. http://mumps.enseeiht.fr/. → page 58

[4] D. G. Aarts, M. Schmidt, and H. N. Lekkerkerker. Direct visual observation of thermal capillary waves. *Science*, 304(5672):847–850, 2004. → page 1

[5] S. Adjerid, N. Chaabane, T. Lin, and P. Yue. An immersed discontinuous finite element method for the stokes problem with a moving interface. *Journal of Computational and Applied Mathematics*, 362:540 – 559, 2019. → page 120

[6] S. Afkhami, Y. Renardy, M. Renardy, J. S. Riffle, and T. St Pierre. Field-induced motion of ferrofluid droplets through immiscible viscous media. *Journal of Fluid Mechanics*, 610:363–380, 2008. → pages 7, 9

[7] S. Afkhami, A. J. Tyler, Y. Renardy, M. Renardy, T. G. S. Pierre, R. C. Woodward, and J. S. Riffle. Deformation of a hydrophobic ferrofluid droplet suspended in a viscous medium under uniform magnetic fields. *Journal of Fluid Mechanics*, 663:358–384, 2010. → pages xi, 6, 9, 10, 38, 40, 61, 62

[8] P. R. Amestoy, I. S. Duff, and J.-Y. L'excellent. Multifrontal parallel distributed symmetric and unsymmetric solvers. *Computer Methods in Applied Mechanics and Engineering*, 184(2-4):501–520, 2000. → page 58

[9] D. M. Anderson, G. B. McFadden, and A. A. Wheeler. Diffuse-interface methods in fluid mechanics. *Annual Review of Fluid Mechanics*, 30(1): 139–165, 1998. → page 35

[10] D. Andrienko, G. Germano, and M. P. Allen. Computer simulation of topological defects around a colloidal particle or droplet dispersed in a nematic host. *Physical Review E*, 63(4):041701, 2001. → page 21

[11] J. H. Argyris, I. Fried, and D. W. Scharpf. The TUBA family of plate elements for the matrix displacement method. *The Aeronautical Journal*, 72(692):701–709, 1968. → page 55

[12] J. C. Bacri and D. Salin. Instability of ferrofluid magnetic drops under magnetic field. 43:649–654, 1982. → page 6

[13] J. C. Bacri, A. O. Cēbers, and R. Perzynski. Behavior of a magnetic fluid microdrop in a rotating magnetic field. *Physical Review Letters*, 72(17): 2705–2708, 1994. → page 7

[14] J. C. Bacri, C. Drame, B. Kashevsky, S. Neveu, R. Perzynski, and C. Redon. Motion of a pair of rigid ferrofluid drops in a rotating magnetic field. In *Trends in Colloid and Interface Science IX. Progress in Colloid and Polymer Science, vol 98*, pages 124–127. Springer, 1995. → pages 8, 64, 69, 76

[15] R. L. Bailey. Lesser known applications of ferrofluids. *Journal of Magnetism and Magnetic Materials*, 39(1-2):178–182, 1983. → page 6

[16] N. Balmforth, S. Ghadge, and T. Myers. Surface tension driven fingering of a viscoplastic film. *Journal of Non-Newtonian Fluid Mechanics*, 142(1-3): 143–149, 2007. → page 2

[17] G. Barbero and G. Durand. Surface anchoring of nematic liquid crystals. In G. P. Crawford and S. Zumer, editors, *Liquid Crystals in Complex Geometries*, chapter 2, pages 21–52. Taylor & Francis, London, 1996. → page 41

[18] J. C. Baygents, N. J. Rivette, and H. A. Stone. Electrohydrodynamic deformation and interaction of drop pairs. *Journal of Fluid Mechanics*, 368:359–375, 1998. → page 7

[19] A. N. Beris and B. J. Edwards. *Thermodynamics of Flowing Systems with Internal Microstructure*. Oxford University Press, 1994. → pages 23, 24, 25, 26

[20] F. Bethuel, H. Brezis, F. Hélein, et al. *Ginzburg-Landau Vortices*. Springer, 1994. → page 22

[21] P. Biscari and E. G. Virga. Local stability of biaxial nematic phases between two cylinders. *International Journal of Non-Linear Mechanics*, 32 (2):337–351, 1997. → page 19

[22] C. Blanc, D. Coursault, and E. Lacaze. Ordering nano-and microparticles assemblies with liquid crystals. *Liquid Crystals Reviews*, 1(2):83–109, 2013. → page 15

[23] J. Bosch. *Fast iterative solvers for Cahn-Hilliard problems*. PhD thesis, Otto-von-Guericke Universität Magdeburg, 2016. → page 120

[24] J. U. Brackbill, D. B. Kothe, and C. Zemach. A continuum method for modeling surface tension. *Journal of Computational Physics*, 100: 335–354, 1992. → pages 32, 40

[25] K. E. Brenan, S. L. Campbell, and L. R. Petzold. *Numerical Solution of Initial-value Problems in Differential-algebraic Equations*. SIAM, 1996. → page 58

[26] W. F. Brinkman and P. E. Cladis. Defects in liquid crystals. *Physics Today*, 35(5):48–54, 1982. → page 13

[27] J. W. Cahn and J. E. Hilliard. Free energy of a nonuniform system. i. interfacial free energy. *The Journal of Chemical Physics*, 28(2):258–267, 1958. → page 35

[28] V. Cardoso and Ó. J. C. Dias. Rayleigh-Plateau and Gregory-Laflamme instabilities of black strings. *Physical Review Letters*, 96(18):181601, 2006. → page 1

[29] A. Cēbers. Dynamics of an elongated magnetic droplet in a rotating field. *Physical Review E*, 66(6):061402, 2002. → page 7

[30] A. Cēbers and S. Lācis. Magnetic fluid free surface instabilities in high-frequency rotating magnetic fields. *Brazilian Journal of Physics*, 25 (2):101–111, 1995. → page 7

[31] C.-Y. Chen and C.-S. Li. Ordered microdroplet formations of thin ferrofluid layer breakups. *Physics of Fluids*, 22(1):014105, 2010. → page 7

[32] C.-Y. Chen, H.-C. Hsueh, S.-Y. Wang, and Y.-H. Li. Self-assembly and novel planetary motion of ferrofluid drops in a rotational magnetic field. *Microfluidics and Nanofluidics*, 18(5-6):795–806, 2015. → pages ix, x, 7, 8, 60, 61, 64, 66, 68, 77, 78, 79

[33] X. Chen, D. Ma, V. Yang, and S. Popinet. High-fidelity simulations of impinging jet atomization. *Atomization and Sprays*, 23(12):1079–1101, 2013. → page 1

[34] D. T. Conroy and O. K. Matar. Thin viscous ferrofluid film in a magnetic field. *Physics of Fluids*, 27:092102, 2015. → page 6

[35] M. D. Cowley and R. E. Rosensweig. The interfacial stability of a ferromagnetic fluid. *Journal of Fluid Mechanics*, 30(4):671–688, 1967. → page 6

[36] L. H. P. Cunha, I. R. Siqueira, T. F. Oliveira, and H. D. Ceniceros. Field-induced control of ferrofluid emulsion rheology and droplet break-up in shear flows. *Physics of Fluids*, 30(12):122110, 2018. → page 121

[37] K. D. Danov, P. A. Kralchevsky, B. N. Naydenov, and G. Brenn. Interactions between particles with an undulated contact line at a fluid interface: capillary multipoles of arbitrary order. *Journal of Colloid and Interface Science*, 287(1):121–134, 2005. → page 15

[38] P. G. de Gennes and J. Prost. *The Physics of Liquid Crystals*. Clarendon Press, 2nd edition, 1993. → pages 13, 19, 22, 25, 47, 87, 89, 116

[39] C. Denniston, E. Orlandini, and J. Yeomans. Simulations of liquid crystal hydrodynamics in the isotropic and nematic phases. *Europhysics Letters*, 52(4):481–487, 2000. → page 24

[40] C. Denniston, E. Orlandini, and J. Yeomans. Lattice Boltzmann simulations of liquid crystal hydrodynamics. *Physical Review E*, 63(5): 056702, 2001. → pages 24, 25, 26, 88

[41] C. Denniston, E. Orlandini, and J. Yeomans. Phase ordering in nematic liquid crystals. *Physical Review E*, 64(2):021701, 2001. → pages 25, 117

[42] J. W. Doane, A. Golemme, J. L. West, J. B. Whitehead, and B.-G. Wu. Polymer dispersed liquid crystals for display application. *Molecular Crystals and Liquid Crystals Incorporating Nonlinear Optics*, 165(1): 511–532, 1988. → pages 2, 97

[43] M. Doi and S. F. Edwards. *The Theory of Polymer Dynamics*. Oxford University Press, 1988. → pages 19, 23, 47, 88

[44] P. V. Dolganov and V. K. Dolganov. Director configuration and self-organization of inclusions in two-dimensional smectic membranes. *Physical Review E*, 73:041706, 2006. → page 108

[45] A. Doostmohammadi, J. Ignés-Mullol, J. M. Yeomans, and F. Sagués. Active nematics. *Nature Communications*, 9:3246, 2018. → page 122

[46] B. J. Edwards, A. N. Beris, and M. Grmela. Generalized constitutive equation for polymeric liquid crystals Part 1. Model formulation using the Hamiltonian (poisson bracket) formulation. *Journal of Non-Newtonian Fluid Mechanics*, 35(1):51–72, 1990. → pages 24, 25, 26

[47] B. J. Edwards, A. N. Beris, M. Grmela, and R. G. Larson. Generalized constitutive equation for polymeric liquid crystals: Part 2. Non-homogeneous systems. *Journal of Non-Newtonian Fluid Mechanics*, 36:243–254, 1990. → page 24

[48] J. Erdmanis, G. Kitenbergs, R. Perzynski, and A. Cēbers. Magnetic micro-droplet in rotating field: numerical simulation and comparison with experiment. *Journal of Fluid Mechanics*, 821:266–295, 2017. → pages 7, 10

[49] J. Ericksen. Liquid crystals with variable degree of orientation. *Archive for Rational Mechanics and Analysis*, 113(2):97–120, 1991. → page 22

[50] G. Falcucci, G. Chiatti, S. Succi, A. A. Mohamad, and A. Kuzmin. Rupture of a ferrofluid droplet in external magnetic fields using a single-component Lattice Boltzmann model for nonideal fluids. *Physical Review E*, 79(5): 056706, 2009. → page 7

[51] J. J. Feng and C.-Y. Chen. Interfacial dynamics in complex fluids. *Journal of Fluid Science and Technology*, 11:JFST0021, 2016. → page 6

[52] J. J. Feng and C. Zhou. Orientational defects near colloidal particles in a nematic liquid crystal. *Journal of Colloid and Interface Science*, 269(1): 72–78, 2004. → pages 14, 21, 81

[53] J. J. Feng, C. Chaubal, and L. Leal. Closure approximations for the Doi theory: which to use in simulating complex flows of liquid-crystalline polymers? *Journal of Rheology*, 42(5):1095–1119, 1998. → page 23

[54] J. J. Feng, G. Sgalari, and L. G. Leal. A theory for flowing nematic polymers with orientational distortion. *Journal of Rheology*, 44(5): 1085–1101, 2000. → pages 23, 81, 88

[55] B. Fischer, B. Huke, M. Lücke, and R. Hempelmann. Brownian relaxation of magnetic colloids. *Journal of Magnetism and Magnetic Materials*, 289: 74–77, 2005. → page 10

[56] G. Foffano, J. Lintuvuori, A. Tiribocchi, and D. Marenduzzo. The dynamics of colloidal intrusions in liquid crystals: a simulation perspective. *Liquid Crystals Reviews*, 2(1):1–27, 2014. → page 15

[57] J. Fukuda and H. Yokoyama. Director configuration and dynamics of a nematic liquid crystal around a two-dimensional spherical particle: Numerical analysis using adaptive grids. *The European Physical Journal E*, 4(3):389–396, 2001. → pages 23, 107

[58] J.-i. Fukuda, M. Yoneya, and H. Yokoyama. Defect structure of a nematic liquid crystal around a spherical particle: adaptive mesh refinement approach. *Physical Review E*, 65(4):041709, 2002. → pages 23, 81, 85, 108

[59] Y. Gao, M. A. Hulsen, T. G. Kang, and J. M. J. den Toonder. Numerical and experimental study of a rotating magnetic particle chain in a viscous fluid. *Physical Review E*, 86(4):041503, 2012. → page 8

[60] C. G. Garton and Z. Krasucki. Bubbles in insulating liquids: stability in an electric field. *Proceedings of the Royal Society of London. Series A. Mathematical and Physical Sciences*, 280(1381):211–226, 1964. → page 7

[61] M. A. Gharbi, M. Nobili, M. In, G. Prévot, P. Galatola, J.-B. Fournier, and C. Blanc. Behavior of colloidal particles at a nematic liquid crystal interface. *Soft Matter*, 7(4):1467–1471, 2011. → page 16

[62] M. A. Gharbi, D. Seč, T. Lopez-Leon, M. Nobili, M. Ravnik, S. Žumer, and C. Blanc. Microparticles confined to a nematic liquid crystal shell. *Soft Matter*, 9(29):6911–6920, 2013. → page 16

[63] Y. Gu and N. L. Abbott. Observation of Saturn-ring defects around solid microspheres in nematic liquid crystals. *Physical Review Letters*, 85(22): 4719, 2000. → page 81

[64] S. Guido and M. Villone. Measurement of interfacial tension by drop retraction analysis. *Journal of Colloid and Interface Science*, 209(1): 247–250, 1999. → pages xvi, 97, 102, 103

[65] O. Guzmán, E. Kim, S. Grollau, N. Abbott, and J. de Pablo. Defect structure around two colloids in a liquid crystal. *Physical Review Letters*, 91(23):235507, 2003. → page 21

[66] J. Han, Y. Luo, W. Wang, P. Zhang, and Z. Zhang. From microscopic theory to macroscopic theory: a systematic study on modeling for liquid crystals. *Archive for Rational Mechanics and Analysis*, 215(3):741–809, 2015. → page 23

[67] G. Helgesen, P. Pieranski, and A. T. Skjeltorp. Dynamic behavior of simple magnetic hole systems. *Physical Review A*, 42(12):7271–7280, 1990. → pages 8, 64, 69, 70, 76

[68] C. Hirt and B. Nichols. Volume of fluid (VOF) method for the dynamics of free boundaries. *Journal of Computational Physics*, 39(1):201–225, 1981. → page 32

[69] H. H. Hu, N. Patankar, and M. Zhu. Direct numerical simulations of fluid-solid systems using the arbitrary Lagrangian-Eulerian technique. *Journal of Computational Physics*, 169(2):427–462, 2001. → page 31

[70] F. R. Hung, O. Guzmán, B. T. Gettelfinger, N. L. Abbott, and J. J. de Pablo. Anisotropic nanoparticles immersed in a nematic liquid crystal: defect structures and potentials of mean force. *Physical Review E*, 74(1):011711, 2006. → pages 21, 88, 100

[71] J. D. Jackson. *Classical electrodynamics*. Wiley, 3rd edition, 1998. → page 64

[72] D. Jacqmin. Calculation of two-phase Navier-Stokes flows using phase-field modeling. *Journal of Computational Physics*, 155(1):96–127, 1999. → pages 35, 36

[73] H. Jeridi, M. A. Gharbi, T. Othman, and C. Blanc. Capillary-induced giant elastic dipoles in thin nematic films. *Proceedings of the National Academy of Sciences*, 112(48):14771–14776, 2015. → page 16

[74] H. Jeridi, M. Tasinkevych, T. Othman, and C. Blanc. Colloidal particles in thin nematic wetting films. *Langmuir*, 32(35):9097–9107, 2016. → pages 16, 17, 18, 41

[75] R. D. Kamien. The geometry of soft materials: a primer. *Reviews of Modern Physics*, 74:953–971, 2002. → page 107

[76] J. Kierzenka and L. F. Shampine. A BVP solver based on residual control and the Maltab PSE. *ACM Transactions on Mathematical Software*, 27(3): 299–316, 2001. → page 92

[77] J.-W. Kim, H. Kim, M. Lee, and J. J. Magda. Interfacial tension of a nematic liquid crystal/water interface with homeotropic surface alignment. *Langmuir*, 20:8110–8113, 2004. → page 100

[78] M. S. Korlie, A. Mukherjee, B. G. Nita, J. G. Stevens, A. D. Trubatch, and P. Yecko. Modeling bubbles and droplets in magnetic fluids. *Journal of Physics: Condensed Matter*, 20(20):204143, 2008. → page 7

[79] P. A. Kralchevsky and K. Nagayama. Capillary interactions between particles bound to interfaces, liquid films and biomembranes. *Advances in Colloid and Interface Science*, 85(2):145–192, 2000. → page 16

[80] S. Lācis. Bending of ferrofluid droplet in rotating magnetic field. *Journal of Magnetism and Magnetic Materials*, 201(1):335–338, 1999. → page 7

[81] B. Lafaurie, C. Nardone, R. Scardovelli, S. Zaleski, and G. Zanetti. Modeling merging and fragmentation in multiphase flow with SURFER. *Journal of Computational Physics*, 113(1):134–147, 1994. → page 32

[82] H. Lamb. Xv. on the uniform motion of a sphere through a viscous fluid. *Philosophical Magazine*, 21(121):112–121, 1911. → page 77

[83] R. G. Larson. *The Structure and Rheology of Complex Fluids*. Oxford University Press New York, 1999. → pages 1, 19, 21

[84] O. M. Lavrenteva and A. Nir. Viscoplastic flows with free boundaries and interfaces. *Reviews in Chemical Engineering*, 26(5-6):149–170, 2010. → page 2

[85] O. D. Lavrentovich. Topological defects in dispersed words and worlds around liquid crystals, or liquid crystal drops. *Liquid Crystals*, 24(1): 117–126, 1998. → pages 14, 98, 107

[86] A. V. Lebedev and K. I. Morozov. Dynamics of a drop of magnetic liquid in a rotating magnetic field. 65(2):160–165, 1997. → page 7

[87] A. V. Lebedev, A. Engel, K. I. Morozov, and H. Bauke. Ferrofluid drops in rotating magnetic fields. *New Journal of Physics*, 5(1):57, 2003. → page 7

[88] H. S. Lee and M. M. Denn. The deformation and retraction of thermotropic LCP droplets in a flexible polymer matrix. *Journal of Non-Newtonian Fluid Mechanics*, 93(2-3):315–323, 2000. → page 97

[89] W. K. Lee, R. Scardovelli, A. D. Trubatch, and P. Yecko. Numerical, experimental, and theoretical investigation of bubble aggregation and deformation in magnetic fluids. *Physical Review E*, 82(1):016302, 2010. → page 7

[90] E. P. Lewandowski, M. Cavallaro Jr, L. Botto, J. C. Bernate, V. Garbin, and K. J. Stebe. Orientation and self-assembly of cylindrical particles by anisotropic capillary interactions. *Langmuir*, 26(19):15142–15154, 2010. → page 15

[91] J. Li and Y. Renardy. Numerical study of flows of two immiscible liquids at low Reynolds number. *SIAM Review*, 42(3):417–439, 2000. → page 32

[92] K. Li, N. M. Atallah, G. A. Main, and G. Scovazzi. The shifted interface method: A flexible approach to embedded interface computations. *International Journal for Numerical Methods in Engineering*, 121(3): 492–518, 2020. → page 120

[93] F.-H. Lin. Nonlinear theory of defects in nematic liquid crystals; phase transition and flow phenomena. *Communications on Pure and Applied Mathematics*, 42(6):789–814, 1989. → pages 18, 22

[94] F.-H. Lin and C. Liu. Nonparabolic dissipative systems modeling the flow of liquid crystals. *Communications on Pure and Applied Mathematics*, 48 (5):501–537, 1995. → page 22

[95] C. Liu and J. Shen. A phase field model for the mixture of two incompressible fluids and its approximation by a Fourier-spectral method. *Physica D: Nonlinear Phenomena*, 179(3-4):211–228, 2003. → page 35

[96] C. Liu and N. J. Walkington. Approximation of liquid crystal flows. *SIAM Journal on Numerical Analysis*, 37(3):725–741, 2000. → pages 22, 23, 55

[97] C. Liu and N. J. Walkington. Mixed methods for the approximation of liquid crystal flows. *ESAIM: Mathematical Modelling and Numerical Analysis*, 36(2):205–222, 2002. → page 55

[98] C. Liu, J. Shen, J. J. Feng, and P. Yue. Variational approach in two-phase flows of complex fluids: transport and induced elastic stress. *Mathematical*

Models and Methods in Phase Transitions, Nova Publications, 2005. → pages 98, 100, 103, 108, 109

[99] I. B. Liu, M. A. Gharbi, V. L. Ngo, R. D. Kamien, S. Yang, and K. J. Stebe. Elastocapillary interactions on nematic films. *Proceedings of the National Academy of Sciences*, 112(20):6336–6340, 2015. → page 16

[100] I. B. Liu, N. Sharifi-Mood, and K. J. Stebe. Capillary assembly of colloids: Interactions on planar and curved interfaces. *Annual Review of Condensed Matter Physics*, 9:283–305, 2018. → page 16

[101] J. M. López-Herrera, S. Popinet, and M. A. Herrada. A charge-conservative approach for simulating electrohydrodynamic two-phase flows using volume-of-fluid. *Journal of Computational Physics*, 230(5):1939–1955, 2011. → pages 9, 40

[102] T. Lopez-Leon and A. Fernandez-Nieves. Drops and shells of liquid crystal. *Colloid and Polymer Science*, 289(4):345–359, 2011. → pages 98, 107

[103] J.-C. Loudet, A. G. Yodh, and B. Pouligny. Wetting and contact lines of micrometer-sized ellipsoids. *Physical Review Letters*, 97(1):018304, 2006. → page 15

[104] C.-Y. Lu. Dynamics of ferrofluid drops in a rotational field. Master's thesis, National Chiao Tung University, Hsinchu, Taiwan, ROC, 2017. → pages 64, 74

[105] T. Lubensky, D. Pettey, N. Currier, and H. Stark. Topological defects and interactions in nematic emulsions. *Physical Review E*, 57(1):610, 1998. → page 85

[106] J. Lucassen. Capillary forces between solid particles in fluid interfaces. *Colloids and Surfaces*, 65(2-3):131–137, 1992. → page 15

[107] P. Maffettone and M. Minale. Equation of change for ellipsoidal drops in viscous flow. *Journal of Non-Newtonian Fluid Mechanics*, 78(2-3): 227–241, 1998. → page 97

[108] D. Marenduzzo, E. Orlandini, and J. Yeomans. Interplay between shear flow and elastic deformations in liquid crystals. *The Journal of Chemical Physics*, 121(1):582–591, 2004. → page 41

[109] G. Marrucci and F. Greco. A molecular approach to the polydomain structure of LCPs in weak shear flows. *Journal of Non-Newtonian fluid mechanics*, 44:1–13, 1992. → page 23

[110] O. T. Mefford, R. C. Woodward, J. D. Goff, T. P. Vadala, T. G. S. Pierre, J. P. Dailey, and J. S. Riffle. Field-induced motion of ferrofluids through immiscible viscous media: testbed for restorative treatment of retinal detachment. *Journal of Magnetism and Magnetic Materials*, 311(1): 347–353, 2007. → pages 6, 121

[111] N. D. Mermin. The topological theory of defects in ordered media. *Reviews of Modern Physics*, 51(3):591, 1979. → page 14

[112] L. Metselaar, I. Dozov, K. Antonova, E. Belamie, P. Davidson, J. M. Yeomans, and A. Doostmohammadi. Electric-field-induced shape transition of nematic tactoids. *Physical Review E*, 96:022706, 2017. → pages 18, 54, 106

[113] L. Metselaar, J. M. Yeomans, and A. Doostmohammadi. Topology and morphology of self-deforming active shells. *Physical Review Letters*, 123 (20):208001, 2019. → pages 18, 41, 54

[114] J. A. Miranda. Rotating Hele-Shaw cells with ferrofluids. *Physical Review E*, 62:2985–2988, 2000. → page 6

[115] H. Mo, C. Zhou, and W. Yu. A new method to determine interfacial tension from the retraction of ellipsoidal drops. *Journal of Non-Newtonian Fluid Mechanics*, 91(2-3):221–232, 2000. → page 97

[116] K. I. Morozov, A. Engel, and A. V. Lebedev. Shape transformations in rotating ferrofluid drops. *Europhysics Letters*, 58(2):229–235, 2002. → page 7

[117] W. W. Mullins and R. F. Sekerka. Morphological stability of a particle growing by diffusion or heat flow. *Journal of Applied Physics*, 34(2): 323–329, 1963. → page 36

[118] I. Muševič, M. Škarabot, U. Tkalec, M. Ravnik, and S. Žumer. Two-dimensional nematic colloidal crystals self-assembled by topological defects. *Science*, 313(5789):954–958, 2006. → pages 15, 16

[119] P. C. Mushenheim, J. S. Pendery, D. B. Weibel, S. E. Spagnolie, and N. L. Abbott. Straining soft colloids in aqueous nematic liquid crystals. *Proceedings of the National Academy of Sciences*, 113(20):5564–5569, 2016. → page 97

[120] M. Nobili and G. Durand. Disorientation-induced disordering at a nematic-liquid-crystal–solid interface. *Physical Review A*, 46(10):R6174, 1992. → page 42

[121] A. Nych, U. Ognysta, V. Pergamenshchik, B. Lev, V. Nazarenko, I. Muševič, M. Škarabot, and O. Lavrentovich. Coexistence of two colloidal crystals at the nematic-liquid-crystal-air interface. *Physical Review Letters*, 98(5):057801, 2007. → page 16

[122] M. Oettel and S. Dietrich. Colloidal interactions at fluid interfaces. *Langmuir*, 24(4):1425–1441, 2008. → page 16

[123] M. Oettel, A. Domınguez, M. Tasinkevych, and S. Dietrich. Effective interactions of colloids on nematic films. *The European Physical Journal E: Soft Matter and Biological Physics*, 28(2):99–111, 2009. → pages 16, 17

[124] P. D. Olmsted and P. Goldbart. Theory of the nonequilibrium phase transition for nematic liquid crystals under shear flow. *Physical Review A*, 41(8):4578, 1990. → page 23

[125] S. Osher and R. P. Fedkiw. *Level Set Methods and Dynamic Implicit Surfaces*. Springer New York, 2005. → page 32

[126] S. Osher and J. A. Sethian. Fronts propagating with curvature-dependent speed: algorithms based on Hamilton-Jacobi formulations. *Journal of Computational Physics*, 79(1):12–49, 1988. → page 32

[127] B. J. Park, T. Brugarolas, and D. Lee. Janus particles at an oil-water interface. *Soft Matter*, 7(14):6413–6417, 2011. → page 15

[128] R. L. Pego. Front migration in the nonlinear Cahn-Hilliard equation. *Proceedings of the Royal Society of London. A. Mathematical and Physical Sciences*, 422(1863):261–278, 1989. → page 36

[129] C. Pérez-González, R. Alert, C. Blanch-Mercader, M. Gómez-González, T. Kolodziej, E. Bazellieres, J. Casademunt, and X. Trepat. Active wetting of epithelial tissues. *Nature Physics*, 15(1):79–88, 2019. → page 122

[130] S. Popinet. Gerris: a tree-based adaptive solver for the incompressible Euler equations in complex geometries. *Journal of Computational Physics*, 190(2):572–600, 2003. → pages 40, 61, 116

[131] S. Popinet. An accurate adaptive solver for surface-tension-driven interfacial flows. *Journal of Computational Physics*, 228(16):5838–5866, 2009. → pages 9, 32, 33, 38, 40, 60, 61

[132] S. Popinet. Numerical models of surface tension. *Annual Review of Fluid Mechanics*, 50(1):49–75, 2018. → pages 29, 32

[133] S. Popinet and S. Zaleski. A front-tracking algorithm for the accurate representation of surface tension. *International Journal for Numerical Methods in Fluids*, 30(6):775–793, 1999. → page 31

[134] P. Poulin and D. Weitz. Inverted and multiple nematic emulsions. *Physical Review E*, 57(1):626, 1998. → page 15

[135] P. Poulin, H. Stark, T. Lubensky, and D. Weitz. Novel colloidal interactions in anisotropic fluids. *Science*, 275(5307):1770–1773, 1997. → pages 15, 97

[136] T. Qian and P. Sheng. Generalized hydrodynamic equations for nematic liquid crystals. *Physical Review E*, 58(6):7475, 1998. → page 23

[137] M. Qiu, S. Afkhami, C.-Y. Chen, and J. J. Feng. Interaction of a pair of ferrofluid drops in a rotating magnetic field. *Journal of Fluid Mechanics*, 846:121–142, 2018. → page v

[138] P. K. Rai, M. M. Denn, and C. Maldarelli. Interfacial tension of liquid crystalline droplets. *Langmuir*, 19(18):7370–7373, 2003. → page 100

[139] A. Rapini and M. Papoular. Distorsion d'une lamelle nématique sous champ magnétique conditions d'ancrage aux parois. *Le Journal de Physique Colloques*, 30(C4):C4–54, 1969. → page 42

[140] M. Ravnik and S. Žumer. Landau–de gennes modelling of nematic liquid crystal colloids. *Liquid Crystals*, 36(10-11):1201–1214, 2009. → pages xiv, 14, 15, 17, 18, 41, 81, 82, 84, 85, 100, 108, 116

[141] M. Ravnik, M. Škarabot, S. Žumer, U. Tkalec, I. Poberaj, D. Babič, N. Osterman, and I. Muševič. Entangled nematic colloidal dimers and wires. *Physical Review Letters*, 99(24):247801, 2007. → page 23

[142] Y. Renardy and M. Renardy. PROST: A parabolic reconstruction of surface tension for the volume-of-fluid method. *Journal of Computational Physics*, 183(2):400–421, 2002. → page 33

[143] A. D. Rey. Marangoni flow in liquid crystal interfaces. *The Journal of Chemical Physics*, 110(19):9769–9770, 1999. → pages 97, 110

[144] A. D. Rey. Viscoelastic theory for nematic interfaces. *Physical Review E*, 61(2):1540, 2000. → page 108

[145] A. D. Rey and M. M. Denn. Dynamical phenomena in liquid-crystalline materials. *Annual Review of Fluid Mechanics*, 34(1):233–266, 2002. → pages 97, 108

[146] B. Roman and J. Bico. Elasto-capillarity: deforming an elastic structure with a liquid droplet. *Journal of Physics: Condensed Matter*, 22(49): 493101, 2010. → page 11

[147] R. E. Rosensweig. Magnetic fluids. *Scientific American*, 247:136–145, 1982. → page 6

[148] P. Rowghanian, C. D. Meinhart, and O. Campàs. Dynamics of ferrofluid drop deformations under spatially uniform magnetic fields. *Journal of Fluid Mechanics*, 802:245–262, 2016. → pages 6, 7, 122

[149] R. Scardovelli and S. Zaleski. Direct numerical simulation of free-surface and interfacial flow. *Annual Review of Fluid Mechanics*, 31(1):567–603, 1999. → page 29

[150] C. E. Scott and C. W. Macosko. Morphology development during the initial stages of polymer-polymer blending. *Polymer*, 36(3):461 – 470, 1995. → page 2

[151] F. Serra. Curvature and defects in nematic liquid crystals. *Liquid Crystals*, 43(13-15):1920–1936, 2016. → pages 98, 107

[152] F. Serwane, A. Mongera, P. Rowghanian, D. A. Kealhofer, A. A. Lucio, Z. M. Hockenbery, and O. Campàs. In vivo quantification of spatially varying mechanical properties in developing tissues. *Nature Methods*, 14 (2):181–186, 2017. → pages 6, 121, 122

[153] J. Shen, J. Xu, and J. Yang. A new class of efficient and robust energy stable schemes for gradient flows. *SIAM Review*, 61(3):474–506, 2019. → pages 116, 120

[154] J. D. Sherwood. The deformation of a fluid drop in an electric field: a slender-body analysis. *Journal of Physics A Mathematical and Theoretical*, 24(17):4047–4053, 1991. → page 7

[155] M. I. Shliomis. Effective viscosity of magnetic suspensions. 34(6): 1291–1294, 1972. → page 39

[156] M. I. Shliomis and K. I. Morozov. Negative viscosity of ferrofluid under alternating magnetic field. *Physics of Fluids*, 6(8):2855–2861, 1994. → page 10

[157] I. I. Smalyukh. Liquid crystal colloids. *Annual Review of Condensed Matter Physics*, 9(1):207–226, 2018. → page 15

[158] I. I. Smalyukh, S. Chernyshuk, B. Lev, A. Nych, U. Ognysta, V. Nazarenko, and O. Lavrentovich. Ordered droplet structures at the liquid crystal surface and elastic-capillary colloidal interactions. *Physical Review Letters*, 93(11):117801, 2004. → pages 16, 121

[159] A. Sonnet, P. Maffettone, and E. Virga. Continuum theory for nematic liquid crystals with tensorial order. *Journal of Non-Newtonian Fluid Mechanics*, 119(1-3):51–59, 2004. → page 23

[160] D. Stamou, C. Duschl, and D. Johannsmann. Long-range attraction between colloidal spheres at the air-water interface: the consequence of an irregular meniscus. *Physical Review E*, 62(4):5263, 2000. → page 15

[161] H. Stark and T. Lubensky. Poisson-bracket approach to the dynamics of nematic liquid crystals. *Physical Review E*, 67(6):061709, 2003. → page 23

[162] A. Stomakhin, C. Schroeder, L. Chai, J. Teran, and A. Selle. A material point method for snow simulation. *ACM Transactions on Graphics*, 32(4): 1–10, 2013. → page 29

[163] H. A. Stone, J. R. Lister, and M. P. Brenner. Drops with conical ends in electric and magnetic fields. *Proceedings of the Royal Society of London. Series A. Mathematical and Physical Sciences*, 455(1981):329–347, 1999. → page 7

[164] M. Sussman and E. Fatemi. An efficient, interface-preserving level set redistancing algorithm and its application to interfacial incompressible fluid flow. *SIAM Journal on Scientific Computing*, 20(4):1165–1191, 1999. → page 33

[165] M. Sussman, P. Smereka, and S. Osher. A level set approach for computing solutions to incompressible two-phase flow. *Journal of Computational Physics*, 114(1):146–159, 1994. → page 32

[166] D. Svenšek and S. Žumer. Hydrodynamics of pair-annihilating disclination lines in nematic liquid crystals. *Physical Review E*, 66(2):021712, 2002. → pages 23, 92

[167] R. J. Tackett, J. Thakur, N. Mosher, E. Perkins-Harbin, R. E. Kumon, L. Wang, C. Rablau, and P. P. Vaishnava. A method for measuring the Néel relaxation time in a frozen ferrofluid. *Journal of Applied Physics*, 118(6): 064701, 2015. → page 10

[168] S.-H. Tan, N.-T. Nguyen, L. Yobas, and T. G. Kang. Formation and manipulation of ferrofluid droplets at a microfluidic T-junction. *Journal of Micromechanics and Microengineering*, 20(4):045004, 2010. → page 6

[169] J. V. I. Timonen, M. Latikka, L. Leibler, R. H. A. Ras, and O. Ikkala. Switchable static and dynamic self-assembly of magnetic droplets on superhydrophobic surfaces. *Science*, 341(6143):253–257, 2013. → page 7

[170] D. Torres and J. Brackbill. The point-set method: front-tracking without connectivity. *Journal of Computational Physics*, 165(2):620–644, 2000. → page 31

[171] I. Torres-Díaz and C. Rinaldi. Recent progress in ferrofluids research: novel applications of magnetically controllable and tunable fluids. *Soft Matter*, 10:8584–8602, 2014. → page 6

[172] G. Tóth, C. Denniston, and J. M. Yeomans. Hydrodynamics of topological defects in nematic liquid crystals. *Physical Review Letters*, 88(10):105504, 2002. → pages xv, 23, 92, 93, 94, 95

[173] G. Tóth, C. Denniston, and J. Yeomans. Hydrodynamics of domain growth in nematic liquid crystals. *Physical Review E*, 67(5):051705, 2003. → page 41

[174] D. Vella and L. Mahadevan. The "Cheerios effect". *American Journal of Physics*, 73(9):817–825, 2005. → page 1

[175] P. A. Voltairas, D. I. Fotiadis, and L. K. Michalis. Hydrodynamics of magnetic drug targeting. *Journal of Biomechanics*, 35(6):813–821, 2002. → pages 6, 121

[176] Q. Wang. A hydrodynamic theory for solutions of nonhomogeneous nematic liquid crystalline polymers of different configurations. *The Journal of Chemical Physics*, 116(20):9120–9136, 2002. → page 23

[177] E. J. Willman. *Three dimensional finite element modelling of liquid crystal electro-hydrodynamics*. PhD thesis, University College London (University of London), 2009. → page 23

[178] M. Wörner. Numerical modeling of multiphase flows in microfluidics and micro process engineering: a review of methods and applications. *Microfluidics and Nanofluidics*, 12(6):841–886, 2012. → pages 29, 32

[179] Y. Wu, W. Yu, and C. Zhou. A study on interfacial tension between flexible polymer and liquid crystal. *Journal of Colloid and Interface Science*, 298 (2):889–898, 2006. → page 97

[180] X. Xu, M. Dey, M. Qiu, and J. J. Feng. Modelling of van der Waals force with smoothed particle hydrodynamics: application to the rupture of thin liquid films. *Applied Mathematical Modelling*, 83:719–735, 2020. → page 29

[181] P. Yue, J. J. Feng, C. Liu, and J. Shen. A diffuse-interface method for simulating two-phase flows of complex fluids. *Journal of Fluid Mechanics*, 515:293–317, 2004. → pages 17, 18, 22, 34, 35, 36, 37, 41, 44, 47, 49, 50, 52

[182] P. Yue, J. J. Feng, C. Liu, and J. Shen. Diffuse-interface simulations of drop coalescence and retraction in viscoelastic fluids. *Journal of Non-Newtonian Fluid Mechanics*, 129:163–176, 2005. → pages 37, 75

[183] P. Yue, J. J. Feng, C. Liu, and J. Shen. Interfacial forces and marangoni flow on a nematic drop retracting in an isotropic fluid. *Journal of Colloid and Interface Science*, 290(1):281–288, 2005. → pages 17, 22, 97, 98, 100, 103, 108, 109, 110

[184] P. Yue, C. Zhou, and J. J. Feng. A computational study of the coalescence between a drop and an interface in Newtonian and viscoelastic fluids. *Physics of Fluids*, 18(10):102102, 2006. → page 2

[185] P. Yue, C. Zhou, J. J. Feng, C. F. Ollivier-Gooch, and H. H. Hu. Phase-field simulations of interfacial dynamics in viscoelastic fluids using finite elements with adaptive meshing. *Journal of Computational Physics*, 219 (1):47–67, 2006. → pages 18, 35, 36, 49, 51, 54, 55, 57

[186] P. Yue, C. Zhou, and J. J. Feng. Spontaneous shrinkage of drops and mass conservation in phase-field simulations. *Journal of Computational Physics*, 223(1):1–9, 2007. → pages 36, 37, 56

[187] P. Yue, C. Zhou, and J. J. Feng. Sharp-interface limit of the Cahn–Hilliard model for moving contact lines. *Journal of Fluid Mechanics*, 645:279–294, 2010. → pages 37, 53

[188] C. Zhou, P. Yue, and J. J. Feng. The rise of newtonian drops in a nematic liquid crystal. *Journal of Fluid Mechanics*, 593:385–404, 2007. → pages 17, 22, 37, 54, 92, 100

[189] C. Zhou, P. Yue, and J. J. Feng. Dynamic simulation of droplet interaction and self-assembly in a nematic liquid crystal. *Langmuir*, 24(7):3099–3110, 2008. → pages 17, 22, 23, 37, 54, 100

[190] C. Zhou, P. Yue, J. J. Feng, C. F. Ollivier-Gooch, and H. H. Hu. 3D phase-field simulations of interfacial dynamics in Newtonian and viscoelastic fluids. *Journal of Computational Physics*, 229(2):498–511, 2010. → pages 36, 102

[191] G.-P. Zhu, N.-T. Nguyen, R. V. Ramanujan, and X.-Y. Huang. Nonlinear deformation of a ferrofluid droplet in a uniform magnetic field. *Langmuir*, 27(24):14834–14841, 2011. → page 6